eman ta zabal zazu

Universidad del País Vasco
Euskal Herriko Unibertsitatea

Department of Theoretical Physics and History of Science

Mapping the Cosmological Expansion

Iker Leanizbarrutia

Ph.D. Thesis
Leioa 2019

Department of Theoretical Physics and History of Science
University of the Basque Country (UPV/EHU)
Postal Box 644, 48080 Bilbao, Spain

Departamento de Física Teórica e Historia de la Ciencia
Universidad del País Vasco (UPV/EHU)
Apartado 644, 48080 Bilbao, España

Fisika Teorikoa eta Zientziaren Historia Saila
Euskal Herriko Unibertsitatea (UPV/EHU)
Posta Kutxatila 644, 48080 Bilbo, Espainia

This document was generated with the 2016 LaTeX distribution.
The plots and figures of this thesis were generated with Wolfram Mathematica, Matplotlib and Inkscape.

This work was funded by the UPV/EHU Ph.D. Grant No. 750/2014.

eman ta zabal zazu

Universidad del País Vasco
Euskal Herriko Unibertsitatea

Department of Theoretical Physics and History of Science

Mapping the Cosmological Expansion

Supervisors:
Dr. Ruth Lazkoz Sáez
Dr. Vincenzo Salzano

Submitted by Iker Leanizbarrutia
for the degree of Doctor of Physics

A Irati y mi familia.

Contents

Acknowledgements / Agradecimientos

Lots of people have guide me during my life towards this point where I am about to finish an important chapter, the PhD thesis. I would like to start giving my sincere gratitude to my supervisors, Ruth Lazkoz and Vincenzo Salzano, for their guidance and patience through this endeavour that has been this thesis. Thanks Ruth for been there to direct this thesis despite all the adversities; and also Enzo, that even with great distance between us he still managed to help a lot. I know it has been tough for all three of us, but my limited writing skill may not reflect how grateful I am for the opportunity you gave me.

I am also thankful to the people of the Department of Theoretical Physics and History of Science, for everything they taught me and for the nice working and learning environment: Alex Feinstein, David Brizuela, Iñaki Garay, Jon Urrestilla, José Juan Blanco Pillado, José M. Senovilla, Juan M. Aguirregabiria, Ivan De Martino, Igor Bandos, Manuel Ángel Valle, Jesus Ibañez and Montserrat Barrio. I would like to thank specially Iñigo L. Egusquiza, whose help dealing with bureaucracy was invaluable; and also Raül Vera, for his useful tips about computers and his aid with the bureaucracy regarding my teaching duties. I also thank Mariam Bouhmadi for her encouragement and help during the last part of this thesis, and for her nice company in the office. Besides, the financial support from the UPV/EHU, as well as from various research projects led by Alex Feinstein, Ruth Lazkoz and José M. Senovilla, made this thesis possible. Apart from letting me attend several conferences and a summer school, these supports also eased the work with collaborators by allowing numerous visits.

These collaborators somehow helped to shape this thesis to the current form, in addition to teach me valuable lessons. For this I thank collaborators from other universities, including Francisco Lobo, Ismael Tereno and Alberto Rozas-Fernandez. I would like to thank Diego Saez-Gomez especially, who provided the initial spark not only for these collaborations, but also for this thesis, encouraging me towards the scientific world. The hospitality they all gave me both at the University of Lisbon and at the Institute of Astrophysics during my several visits was as wonderful as the city of Lisbon itself. I made excellent friends there, holding Ismael Ayuso a especial place in my memory.

Finally, I would like to thank three marvelous teachers I had at the school, Joseba Unzalu, Xabier Goikoetxea, and Xabier González de San Román. Each one on its special way, they influenced and guided me towards science in general, and physics in particular.

Quiero agradecer a todos los compañeros de penurias, especialmente a María Ortiz Baños como hermana académica, que con su presencia me ha hecho mirar atrás hacia el trayecto común que yo ya había recorrido anteriormente, y que con sus preguntas me ha ayudado a afianzar y repasar los conceptos a lo largo de dicho camino; y a João André Viegas Morais como compañero coetano que me ha ayudado mucho durante este largo viaje, sobretodo las reflexiones en voz alta que hacíamos juntos sobre temas que teníamos dudas, muchas de ellas con una resolución satisfactoria. No me olvido de las últimas incorporaciones al departamento como doctorandos, Francisco Fernandez y Mikel Alvarez Urquiola, cuya amabilidad ha alegrado el ambiente del departamento durante mi duro tramo final de la tesis. Gracias por todos eso momentos de humor, el apoyo brindado, y el sincero compañerismo que habéis conseguido insuflar en el departamento.

Respecto a la anterior generación de doctorandos que han pasado por el departamento, me gustaría agradecer especialmente a Borja Reina como excelente compañero de despacho. También quiero dar las gracias a Asier López Eiguren, Joanes Lizarraga y Pablo Jimeno por las más que esporádicas dudas que me han resuelto, y junto a Borja, agradecerles el buen ambiente que pudimos heredar los doctorandos del departamento.

Tampoco me olvido del resto de compañeros de la uni, aunque seguro que se me olvida alguien, por lo que doy las gracias a Aitziber, Carlos, Charlotte, Dani, Giuseppe, Iagoba, Iñigo, Iraultza, Jeremy, Julen, Kepa, Laura, Lluc, Mattin, Naiara, Nastassja, Olatz, Peio, Raul, Santi, Unai, Uri, Urtzi y a Xiao-Hang, por hacer agradable y amena mi paso por esta dura etapa en la universidad.

Por supuesto, también doy las gracias a toda mi familia por todo el apoyo brindado y toda la confianza puesta en mí. Por todas sus preguntas curiosas que me hacían reflexionar sobre los principios básicos para poder explicárselos mejor. Agradezco especialmente a mis familiares de Galdakao por acogerme en su casa cuando mi ajetreada vida nómada lo requería, y a mis padres por su apoyo incondicional aun con asuntos complicados y difíciles de explicar. Mencionar a mi querida amama Ines, que lamentablemente no va a poder ver el final de esta etapa de mi vida; y a Pitxin también, por toda la compañía que me ofreció durante todas las horas de lectura y estudio que me han traído hasta este punto de mi vida. Quiero agradecer en especial a mis hermanas, Garazi y Nikole, que ante las adversidades de los tramos finales su apoyo fue inestimable.

Por último, quiero agradecer a Irati, por todo. Porque al igual que no concibo haber llegado hasta este punto de mi vida sin ella, tampoco veo cómo habría podido terminar esta tesis sin su ayuda y apoyo. Por muy duro que sea una tesis, me ha ayudado a darme cuenta que se puede superar con esfuerzo, como todo en la vida. Gracias por el maravilloso camino recorrido juntos, y gracias por ayudarme a dar el siguiente paso de mi vida.

Resumen

La expansión acelerada del universo es uno de los pilares de la cosmología actual. Para estudiarlo, en esta tesis se usan observaciones geométricas del universo para poner a prueba la viabilidad de modelos cosmológicos que describen dicha expansión y restringir su espacio de parámetros. Estas observaciones no se centran en las estructuras que observamos hoy en día, sino en el universo a gran escala para trazar su geometría de fondo, o de manera equivalente de acuerdo con la Relatividad General, su contenido energético y/o material. La información que aportan se contrastan con nuevos modelos que se proponen como alternativa a ΛCDM, el modelo cosmológico estándar de consenso. Su nombre deriba de los dos principales componentes que tendría el universo: Λ como la constante cosmológica que impulsa la expansión acelerada del universo, y CDM para la materia oscura fría que permite explicar la formación de estructuras correctamente. Aunque este modelo describe con gran éxito el universo observado, deja abiertas algunas preguntas teóricas como por ejemplo una explicación completa para la existencia de la constante cosmológica, o qué compone exactamente la materia oscura. Ante las incógnitas abiertas, los nuevos modelos alternativos tratan de describir el universo de una forma distinta, usando más grados de libertad para intentar captar cualquier sutileza en la expansión cosmológica que podría derivar en una explicación teórica más completa, o por lo menos una mejor comprensión fenomenológica. Generalmente estos modelos alternativos se enfocan en la aceleración tardía del universo, y se suelen denominar como energía oscura. Pero en el caso de la materia oscura suele implicar variaciones de su proporción respecto a las demás componentes del universo. La teoría estadística con la que se ponen a prueba los diferentes modelos respecto a las observaciones cosmológicas es en el marco de la inferencia Bayesiana, donde todos los modelos cosmológicos considerados se comparan entre ellos utilizando observaciones del fondo cosmológicos recientes.

Estas observaciones cosmológicas han evolucionado desde las primeras que hizo Hubble a principios del siglo XX mostrando indicios de un universo en expansión, y desde entonces han ido incrementando su precisión a lo largo del siglo pasado. Tal ha sido el avance que hoy en día las observaciones del fondo cosmológico predicen con mucha precisión el contenido energético y material del universo. Además, las observaciones del fondo cosmológico concuerdan en gran medida con observaciones astrofísicas donde se refleja la existencia de la materia oscura, y también concuerdan con estudios detallados de las trazas de las perturbaciones cosmológicas que recientemente han permitido las nuevas

tecnologías.

En cosmología, la mayoría de las observaciones disponibles de naturaleza geométrica, por así decirlo, sirven como indicadores de distancia para objetos lejanos, lo que permitiría cuantificar el ritmo de expansión del universo en la época en que la señal luminosa correspondiente fue emitida. Ya sean objetos astronómicos de luminosidad conocida como es el caso de las supernovas tipo Ia (SNe Ia), o la escala de oscilaciones acústicas bariónicas (BAO) en la distribución de galaxias, todos los indicadores de distancia se clasifican en dos categorías: luminarias estándar o reglas estándar respectivamente.

Aunque estas observaciones hayan ido madurando y refinándose con el tiempo desde su concepción, la creciente precisión de las medidas y la extensión de los catálogos en las observaciones están llevando la cosmología a una era de alta precisión, siendo uno de los hitos la observación en 1998 de la expansión acelerada del universo usando SNe Ia. La reciente medición de las anisotropías del fondo cósmico de microondas (CMB) hecho por la colaboración *Planck* también ha sido extraordinaria, donde las mediciones alcanzaron una precisión sin precedentes. Esta cosmología de alta precisión también abre posibilidades de nuevos tipos de observaciones en el futuro cercano, como es el caso estudiado en el Capítulo 6.

En la Parte I, repasamos la base teórica utilizada a lo largo de esta tesis, explicando todo lo necesario para someter a examen diferentes modelos cosmológicos en el marco estadístico de la inferencia Bayesiana utilizando observaciones cosmológicas.

En el Capítulo 1, comenzamos introduciendo conceptos básicos de la Relatividad General aplicados a la cosmología. Exponemos el principio cosmológico, donde se supone que el universo es isótropo y homogéneo partiendo del principio Copernicano de que nuestra posición en el universo no es privilegiada, además de estar contrastado por numerosas observaciones cosmológicas. Gracias al principio cosmológico, la métrica que describe el universo a gran escala se puede simplificar significativamente, y la necesidad de describir la expansión cosmológica junto con los anteriores argumentos conducen a la métrica de Friedmann-Lemaître-Robertson-Walker.

Aplicando esta métrica a las ecuaciones de campo de Einstein, se consiguen las ecuaciones de Friedmann, que describen la evolución del universo, donde solo faltaría especificar su contenido energético y/o material. Analizando los diferentes constituyentes posibles, como la radiación, la materia, u otros fluidos, mostramos la posible evolución que el universo puede presentar para cada caso. Estas diferencias en la evolución del universo se ven reflejadas en la función de Hubble que se define en las ecuaciones de Friedmann. Terminamos el capítulo describiendo el modelo cosmológico estándar de concordancia, llamado ΛCDM, mostrando su función de Hubble donde persisten las grandes incógnitas de la cosmología, la materia oscura fría (CDM) y la constante cosmológica Λ.

En el Capítulo 2 describimos de forma general cómo se miden las distancias en un universo en base a las referencias físicas que estén disponibles para inferirlas. Definimos primero la distancia comóvil básicamente como una integral del inverso de la función de Hubble, que es a su vez la construcción básica de donde se generan las demás distancias usadas en las observaciones, como la distancia luminosa y angular. La distancia comóvil

luminosa está definida por la disminución del flujo energético percibida por un observador comparado a la emisión energética total de una fuente. Por otro lado, la distancia comóvil angular está dada por el aparente ángulo que muestra en el cielo un objeto de cierto tamaño. Para ambos casos hacen falta objetos con ciertas características: para el primer caso son objetos de luminosidad conocida llamados luminarias estándar, y para el segundo caso objetos de tamaño conocido llamados reglas estándar.

Las luminarias estándar son objetos astronómicos cuya luminosidad es afín a la construcción de modelos solventes. Todos los objetos astronómicos lejanos del mismo tipo que cumplen esta propiedad permiten deducir la distancia comóvil luminosa a la que se encuentran, como es el caso de las cefeidas o más recientemente, las supernovas tipo Ia, y son parte esencial de la conocida escalera cósmica para las distancias.

Las reglas estándar son objetos o formaciones cuyo tamaño es conocido, por lo que permite calcular la distancia comóvil angular a la que se encuentran midiendo el ángulo que presentan en el cielo. La única formación dentro de esta categoría lo suficientemente grande como para ser útil en cosmología es la escala a la que se congelaron las oscilaciones acústicas de bariones durante la recombinación. Estas oscilaciones presentes en el plasma primigenio donde bariones y fotones estaban acoplados se originaron a partir de las fluctuaciones cuánticas iniciales. Pero cuando la temperatura del universo disminuyó lo suficiente como para que se formasen los átomos de hidrógeno, los fotones y los bariones dejaron de interaccionar entre si fijando en ese momento la escala de las oscilaciones, y a partir de ahí cada componente evolucionó por su cuenta.

Es por ello que hoy en día tenemos dos formas de medir esa escala, dependiendo de si observamos los bariones o los fotones. En el primer caso, se puede extraer la escala de las oscilaciones acústicas de bariones (BAO) mirando las correlaciones en la distribución de las galaxias. Para el segundo, se miden las anisotropías en el fondo cósmico de microondas (CMB) para extraer la escala equivalente para los fotones.

En el Capítulo 3, la última parte de la introducción, explicamos la teoría estadística de la inferencia Bayesiana utilizada en esta tesis para poner a prueba diferentes modelos respecto a las observaciones cosmológicas. El objetivo es deducir los valores de los parámetros del modelo a probar, o al menos reducir su espacio de parámetros, teniendo en cuenta las observaciones proporcionadas.

La inferencia estadística plantea en términos generales menos dificultades cuando se puede repetir el experimento las veces necesarias hasta obtener suficientes observaciones. Eso permite la aproximación que se denomina como frecuentista, pero no es posible aplicarla a la cosmología dado que solo tenemos una realización del experimento, nuestro universo. Por lo tanto, tenemos que usar la aproximación Bayesiana, que consiste en tomar las limitadas observaciones como únicas y fijas, e intentar inferir de ellas la estadística de los parámetros de los modelos.

Esto se consigue definiendo la función de verosimilitud, que nos da una medida de cuán bien se adaptan los modelos a las observaciones. Esta función se construye teniendo en cuenta cada observación disponible, pero deja como variables libres de la función los parámetros de los modelos. Mediante una aproximación de Monte Carlo aplicada

a cadenas de Markov, se consigue una de las herramientas más comunes del análisis Bayesiano, la cadena de Markov Monte Carlo (MCMC). Una vez validada a través de un análisis de su convergencia y aplicándola a la función de verosimilitud, se puede conseguir la distribución de probabilidad de los parámetros implicados en el modelo deseado. Con toda la información estadística disponible, mostramos varias formas en las que diferentes modelos se pueden comparar entre sí para saber cual se adapta mejor a las observaciones, o para ver si algún modelo es más probable que otro.

Usando los recursos expuestos en la Parte I, en la Parte II de la tesis se utilizan conjuntos de datos de observaciones cosmológicas recientes para probar la viabilidad de ciertos modelos. En el Capítulo 4, mostramos un posible modelo que no solo podría explicar la expansión acelerada del universo como energía oscura, sino que también explicaría la componente de materia oscura observada. Este modelo se basa en un solo fluido exótico en el marco de la relatividad general, con las propiedades necesarias para comportarse de la misma forma que los mencionados componentes oscuros, y entra dentro de los llamados modelos de materia-energía oscura unificados (o UDM por sus siglas en inglés). Suelen tener un régimen parecido a la materia oscura en el pasado, y se comportan como el modelo ΛCDM en el presente, pero por algunos argumentos teóricos la transición entre un régimen y otro tiene que ser veloz. Éste es el caso del modelo UDM fenomenológico que presentamos en este capítulo, donde lo comparamos a otros posibles modelos después de un análisis Bayesiano usando datos cosmológicos geométricos. Los resultados muestran que las observaciones cosmológicas usadas en el análisis apoyan las limitaciones impuestas por la teoría a la velocidad de transición. El trabajo de donde está basado este capítulo fue publicado en la siguiente revista:

- **Cosmological constraints on fast transition unified dark energy and dark matter models**
  R. Lazkoz, I. Leanizbarrutia, V. Salzano, *Physical Review D93, (2016) no.4, 043537; arXiv:1602.01331*.

En el Capítulo 5, constreñimos otro modelo de materia-energía oscura unificada donde el fluido exótico puede estar representado por un campo escalar. Al igual que en el caso anterior, este modelo UDM está construido para tener una transición rápida entre los dos regímenes en consonancia con la teoría, y se limita su espacio de parámetros usando el mismo procedimiento y datos cosmológicos parecidos al Capítulo 4. Tras el análisis Bayesiano y compararlos a otros modelos, los resultados muestran que las observaciones cosmológicas siguen validando las limitaciones teóricas en cuanto a la velocidad de transición entre los diferentes regímenes. Este trabajo junto al resultado donde se muestra un límite inferior para dicha velocidad de transición fueron publicados en:

- **Cosmological constraints on a unified dark matter-energy scalar field model with fast transition**
  I. Leanizbarrutia, A. Rozas-Fernandez, I. Tereno, *Physical Review D96 (2017) no.2, 023503; arXiv:1706.01706*.

Hasta ahora en la Parte II, hemos usado datos observacionales reales para constreñir el espacio de parámetros de diferentes modelos cosmológicos que podrían explicar el sector oscuro del universo. Todos esos datos se basan en medir distancias cosmológicas de diferentes maneras, para así mapear la geometría del universo y estudiar su expansión. Pero estas cantidades implican integraciones de la función de Hubble, reduciendo la cantidad de detalles que se pueden extraer de las observaciones. De todas formas, no todas las mediciones del fondo cosmológico son así, dado que hay futuras observaciones donde se podría medir directamente la función de Hubble. En el Capítulo 6 de la Parte III, simulamos una de estas posibles observaciones que consiste en medir la deriva cósmica del redshift de objetos lejanos, también llamado el test de Sandage-Loeb, y analizamos sus capacidades de constreñir diferentes modelos.

La deriva cósmica del redshift se debe a que en una expansión acelerada del universo, el redshift de objetos lejanos irá aumentando poco a poco según la expansión vaya acelerándose. Paradójicamente, cuando fue propuesto por primera vez por Sandage e incluso al refinarlo más tarde por Loeb, esta observación se planteó para medir la desaceleración del universo, décadas antes del descubrimiento de la expansión acelerada del universo. Dado que el cambio en el redshift es muy leve, casi imperceptible, la observación de este fenómeno incluso hoy en día es prácticamente imposible. Pero futuros espectrómetros mucho más precisos posibilitarían, junto a un periodo de observación prolongado del orden de décadas, la detección de esta señal en un futuro cercano. Para estudiar la viabilidad de estas futuras observaciones, simulamos unos catálogos del test de Sandage-Loeb y las usamos para constreñir los parámetros de varios modelos de entre los más comunes en la literatura. Para contextualizar mejor el trabajo, comparamos los catálogos del test Sandage-Loeb con otras de futuras observaciones más clásicas de supernovas y BAO. Todos los catálogos están creados de la misma forma, basados en un modelo fenomenológico del universo, para así no favorecer ningún modelo cosmológico en particular. Este Capítulo 6, donde los resultados para las observaciones del test Sandage-Loeb son prometedores, está basado en el siguiente artículo publicado:

- **Forecast and analysis of the cosmological redshift drift**
  R. Lazkoz, I. Leanizbarrutia, V. Salzano, *European Physical Journal C78 (2018) no.1, 11; arXiv:1712.07555*.

Otros trabajos publicados durante la tesis:

- **Crossing SNe Ia and BAO observational constraints with local ones in hybrid metric-Palatini gravity**
  I. Leanizbarrutia, F. S.N. Lobo, D. Sáez-Gómez, *Physical Review D95 (2017) no.8, 084046 arXiv:1701.08980*.

- **Cosmological constrains on fast transition Unified Dark Matter models**
  R. Lazkoz, I. Leanizbarrutia, V. Salzano, *Journal of Physics: Conference Series 600 (2015) 012028* .

Prologue

This Ph.D. thesis is centered around cosmological background observations which, according to General Relativity (GR), lead to the measurement of both the energetic content of the universe and its geometry. New models are proposed as alternative to ΛCDM in order to explain the late time acceleration of the universe by dark energy (DE), but also the presence of dark matter (DM). All considered models are tested against each other in the Bayesian inference framework using recent available cosmological observations. The bulk of the thesis is based on works done with my supervisors Ruth Lazkoz and Vincenzo Salzano, having some ancillary projects done with my collaborators Ismael Tereno and Alberto Rozas-Fernadez.

Most of the background observations available in cosmology serve as a distance indicators for distant objects, which allows the measurement of the expansion history of the universe by integrating the inverse of the Hubble function from each observation. Whether astronomical objects of known luminosity as type Ia Supernovae (SNe Ia), or the scale of baryionic acoustic oscillations (BAO) inferred from the galaxy clustering distribution, all distance indicators are classified in two categories, standard candles or standard rulers.

Even though these observations are a mature and refined technique in cosmology, the increasing precision of measurements and extension of catalogs are nowadays moving cosmology into a high-precision era, being one of the milestone the recent cosmic microwave background (CMB) anisotropy measurement done by the *Planck* collaboration. This high-precision cosmology also opens the possibility of new type of observations in the near future.

In Part I, we show all the theoretical background used along this thesis, explaining everything necessary to test different cosmological models in the Bayesian inference framework using cosmological observations. We start introducing basic concepts of General Relativity applied to cosmology, as the different evolution that the universe can have depending on its dominant constituent. After describing the concordance model of ΛCDM, we describe how distances are measured in an universe with few physical references. Besides, we relate these distances with the cosmological observations from where they are inferred, and give full details of how measurements are used for that purpose. In the las part of the introduction, we explain the statistical Bayesian inference used in this thesis to test several different models with various cosmological observations,

giving details of the used mathematical tools as the Markov chain Monte Carlo (MCMC).

In Part II, recent available data sets of cosmological observations explained in Part I are used in order to test several cosmological models. In Chap. 4, we show a possible model to explain both dark matter (DM) and dark energy (DE) with a single exotic fluid within the context of General Relativity. Among the range of these models commonly called as unified dark matter-energy (UDM), the phenomenological fluid presented in this Chap. 4 has a fast transition from the dark matter-like regime to a dark energy-like scenario similar to the ΛCDM case. The requirement for this fast transition is theoretically motivated, and the results after constrained with cosmological background data are in line with those theoretical limitations. The work shown here is based on the published article:

- **Cosmological constraints on fast transition unified dark energy and dark matter models**
  R. Lazkoz, I. Leanizbarrutia, V. Salzano, *Physical Review D93, (2016) no.4, 043537* *arXiv:1602.01331*.

In Chap. 5, we constrain another unified dark matter-energy model that supports a scalar field representation for the exotic UDM fluid. Using a similar approach as in the previous Chap. 4, this UDM model is built to have a fast transition between different regimes according to the theory, which is then constrained using a similar set of cosmological background observables. The theoretical limitations imposed to the transition velocity of the UDM between different regimes are again backed up by background observations. This work, as well as the results showing a lower bound for the transition velocity, have been published in:

- **Cosmological constraints on a unified dark matter-energy scalar field model with fast transition**
  I. Leanizbarrutia, A. Rozas-Fernandez, I. Tereno, *Physical Review D96 (2017) no.2, 023503* *arXiv:1706.01706*.

Hitherto, real data was used to test cosmological models during Part II. In Chap. 6 of Part III, we create mock data sets to study in detail the constraining ability of future observations based on the cosmic redshift drift, also called Sandage-Loeb test. The basic concept for these observations is that, during a certain time period in an expanding universe, the cosmic redshift of distant objects could suffer a slight change if the expansion is accelerated. Though a very subtle effect almost impossible to appreciate, it could be measured with long period spectroscopic measurements of very distant objects, usually quasars. We create a mock data set simulating Sandage-Loeb observations in a fully model independent way, and constrain parameters of the most common models in the literature in order to see the constrain ability of these future observations. To give more insight, we compare the Sandage-Loeb data set with other background future observations for SNe Ia and BAO. This Chap. 6 is based on the published paper:

- **Forecast and analysis of the cosmological redshift drift**
  R. Lazkoz, I. Leanizbarrutia, V. Salzano, *European Physical Journal C78 (2018) no.1, 11* *arXiv:1712.07555*.

Other published works during the thesis:

- **Crossing SNe Ia and BAO observational constraints with local ones in hybrid metric-Palatini gravity**
  I. Leanizbarrutia, F. S.N. Lobo, D. Sáez-Gómez, *Physical Review D95 (2017) no.8, 084046* *arXiv:1701.08980*.

- **Cosmological constrains on fast transition Unified Dark Matter models**
  R. Lazkoz, I. Leanizbarrutia, V. Salzano, *Journal of Physics: Conference Series 600 (2015) 012028* .

PART I

Introduction

1 Historical and technical introduction to cosmology

It is difficult to precisely state when modern cosmology started, but it is clear that the beginning was around the early 20th century. If a decade has to be chosen, a possible candidate could be the 20s, thanks to Edwin Hubble's work. Indeed, his studies paved the road to the definitive acceptance of the real scale of our Universe and, eventually, to the realm of modern cosmology. Moreover, his discoveries led to set up on more solid observational grounds the theoretical knowledge about gravity which, at the time, was experiencing a novel approach from Albert Einstein.

Albert Einstein formulated the definitive form of his theory, the General Relativity, in 1915 [86]. In his approach, the gravitational interaction is explained through the deformation or curvature of a four-dimensional space-time, where test particles in free fall follow geodesics, which are the generalization of Euclidean straight lines to curved space. Einstein also tried to include the known Mach's principle, which was kind of a "milestone" or an inspirational idea for General Relativity. Nevertheless the theory is not actually a Machian one, as Willem de Sitter showed in 1917 with a test particle following geodesics in an empty Universe, thus defining an inertial frame without matter [77]. This problem kept the scientific community busy for several years, and trying to solve it Einstein proposed the cosmological principle, stating that the overall density of the Universe is homogeneous. As a consequence, and in order to have a static Universe, in 1917 Einstein introduced also the cosmological constant into his theory [87].

Few years later, in 1922, Alexander Friedmann found a solution of Einstein's field equations for the case of a closed Universe, namely, when the spatial part of the metric has a positive curvature and can be understood as a 3-dimensional sphere. This solution shows an initial expanding phase, but it eventually collapses to a singularity. Two years later, in 1924, Friedmann generalized his solution to include the case of an open Universe, that is, a solution whose spatial part of the metric is hyperbolic, and which has unbound expanding solutions [100]. In these works, his key contribution was that isotropic models must have constant curvature in every point.

Meanwhile, the observation of the night sky had improved a lot with the inclusion of reflective telescopes and photographic plates. The works in the period-luminosity relation

for Cepheids [144] and the calibration of the magnitude system in the north hemisphere by Henrietta Leavitt, as well as spectroscopic observations leading to the concept of redshift done by Vesto M. Slipher [213], established a firm foundation for the development of observational cosmology in the early 20th century. Therefore, with the new techniques and telescopes, astronomical observations were greatly improved.

The quality and capacity of these new observational tools steered the detailed study and need to catalog the so-called nebulae, faint blurred luminous objects which, from a spectroscopical point of view, seemed collections of stars, but whose resolution was barely enough to start distinguishing individual stars. Moreover, their distances were difficult to measure. The uncertainty whether these nebulae were inside or outside the Milky Way led to the great Shapley-Curtis debate in 1920.

Nevertheless, the mystery lasted until 1923, when Hubble observed the first Cepheid variable in M31 Andromeda nebula. Once its distance was calibrated, it revealed that the Andromeda nebula was far beyond our galaxy's rim and, thus, external to our Milky Way Galaxy. With later works in 1926 [127], Hubble generalized its conclusions, stating that the observed extragalactic nebulae were, in fact, other galaxies. Besides, he adopted Einstein's static Universe and got some roughly numbers regarding the number of galaxies and the radius of the closed geometry, which were the first attempts to constrain a cosmological model.

Friedmann's work remained mainly unnoticed until 1927, when Georges Lemaître independently found the same solutions just before noticing the previous works [146]. Both Lemaître and Howard P. Robertson realized that the expansive nature of the Friedmann's solution leads to a velocity-distance relation. Being aware of this connection, in 1929 Hubble assembled 24 distance measurements to different galaxies [125], whose velocity had been measured spectroscopically mainly by Slipher. Based on these observations, Hubble derived his famous relation between the distance d to a galaxy and its receding velocity v mediated by a constant, $v = H_0\, d$, where H_0 is the now famous Hubble constant. Those measurements gave a value around $H_0 \approx 500\, km\, s^{-1} Mpc^{-1}$, very far from the actual and more precise estimations we have nowadays, but understandable considering the precision of the measurements and the fact that all data to perform the regression fit were within 2 Mpc.

Few years later, Hubble realized that it was possible to test the hypotheses of isotropy and homogeneity of the Universe using the resources he had available at that moment. Counting the amount of faint galaxies detected for each brightness threshold increase, he realized that their number seemed to grow as expected for galaxies uniformly distributed in space [126]. However, the dynamics of these recently discovered galaxies were not fully understood. In order to explain it, the first "dark" ingredient for the Universe was introduced in 1933 by Fritz Zwicky after applying the virial theorem to the Coma cluster [255]: by measuring the velocity dispersion of galaxies within the cluster, it was possible to have an idea of its gravitational potential and, by using the virial theorem, of its total mass. Zwicky showed that the ratio of mass to optical luminosity was far bigger than expected [256]. This idea of *dark matter* (DM) was backed up by the first measurement

of the rotation curves of galaxies, which did not follow the expected Newtonian behaviour, done in 1939 by Horace W. Babcock [21].

During those years and driven by the recent evidence of an expanding Friedmann-like Universe found by Hubble, in 1937 the seed for the Big Bang idea was sown, though the name was given years later, as Lemaître's neutron "primaeval atom" concept [147]. This concept led to the theory of the nucleosynthesis as a brief non-equilibrium process by Ralph Alpher, Hans Bethe & George Gamow in 1948 [13]. According to this idea, starting with a hot and dense epoch, the elements were synthesized in a continuous build-up process, as primordial neutrons decayed into protons and aggregated themselves in heavier elements, until the expansion of the Universe froze this process. Alpher and Robert Herman improved the calculations [12], and discovered that at such high temperatures, the Universe was rather radiation than matter-dominated, and that the remnant of that epoch should have endured until today as a colder thermal background radiation of around 5 K.

As the knowledge in atomic and particle physics increased, the nucleosynthesis theory evolved from the initial decaying-neutron idea to a more complex and complete theory. The initial state was considered a thermodynamic equilibrium stage arisen from interactions between all constituents, mainly protons, neutrons, electrons and positrons, but considering also radiation. The work of Alpher, James Follin & Herman in 1953 gave a promising answer for primordial nucleosynthesis [14], taking into account detailed evolution of neutron capture and β-decay processes that allow a nucleus to increase its nucleon number and change its atomic number, respectively. Understanding the high temperatures involved at primordial nucleosynthesis, their work also included thermonuclear reactions for light nuclei. They showed that the reaction rates were high enough in order to keep the thermodynamic equilibrium during nucleosynthesis, and gave its detailed evolution explaining observations quite well. However, the idea was kept aside by the discovery of element synthesis in stars.

The discovery of the stellar nucleosynthesis was led by Fred Hoyle in 1953 [118], and improved later in 1957 by Margaret Burbidge, Geoffrey Burbidge, William Fowler & Hoyle [51]. The purpose of these works was to find an alternative explanation of primordial nucleosynthesis for the steady-state cosmological model invented few years before, in 1948, by Hermann Bondi & Thomas Gold [45], and Hoyle [117]. This theory, alternative to the Big Bang model, stated that the matter density of the expanding Universe was constant due to uniform matter creation. Despite the model was eventually proved wrong, and apart of the "Big Bang" derogatory term given by Hoyle to Friedmann models, the steady-state cosmology included also some features which had similarities with the future theory of inflation; in particular, the idea of a spatially flat geometry and of an exponential evolution of the scale factor driven by a "creation field".

Nevertheless, helium abundance was difficult to explain through stellar nucleosynthesis only, and even more after the observations performed between 1961 and 1964. This led Hoyle and Roger Tayler to revisit the primordial nucleosynthesis idea in 1964 and to conclude that the helium was synthesized in great abundance when the Universe was

extreme hot and dense [119], as in the Big Bang scenario, though no mention of the cooler remnant radiation was done.

Meanwhile, Arno Penzias and Robert Wilson were testing their new radiometer for radio astronomy and satellite communication experiments. During set up procedures, they unexpectedly discovered a smooth and always there cosmic microwave background (CMB), in 1964 [177]. Though at the beginning they did not know what it was exactly, at the same time also Robert Dicke's group was working on this possible signature from a theoretical perspective. Then, when both groups realized each other's discovery and work [79], by sharing the knowledge, they together measured the low temperature of the relic black body radiation from the past Big Bang event [192]. The discovery of the CMB radiation shed light onto the early Universe concept, and the Friedmann-Lemaître model of the Big Bang was strengthened.

Regarding the dark side of the Universe, during the 1960s–1970s Vera Rubin and Kent Ford performed more and better observations of the rotation curves of galaxies, providing further strong evidence for DM [195]. Some years later, however, the Universe gave another further surprise in 1998. During that decade, Type Ia Supernovae (SNe) had become common standard candles, namely stellar objects whose intrinsic luminosity is known and can thus be used to measure their distance from us. Using SNe as standard candles, the groups of Adam G. Riess and Saul Perlmutter discovered that, instead of the receding expansion that was thought to be occurring, the Universe was in fact going through an accelerated expansion phase [178, 186].

With time other observations confirmed this initial discovery, and the scientific community has been trying to explain this acceleration by different ways since then. The simplest candidate was and still is a constant, the so-called cosmological constant Λ which should be a measure of the energy density of the vacuum, its state of lowest energy [57, 199]. But in other models, and more in general, any "dark" cosmic ingredient or theory that leads to this accelerated expansion can be a possible candidate for it. They are generally referred as *dark energy* (DE).

This first chapter is dedicated to explaining the basic concepts of General Relativity (GR) and its application to cosmology, reaching at the end the description of the most accredited cosmological model nowadays. We begin by making an overview of the mathematical theory of differential geometry that explains gravity as a deformation of the space-time. This leads to Einstein's General Relativity and the description of an expanding Universe once we establish some basic cosmological principles. Detailing the energy content of the Universe we see how differently it evolves, and when several ingredients are considered, how the behavior of the expansion changes depending on the dominant content. Giving full details of the Universe's ingredients and trying to explain the cosmic observations, we show the simplest but most accepted model, the ΛCDM model.

1.1 The main pillar: General Relativity

There is no better way to introduce GR and its paramount change in the way of thinking about gravity than by citing John Archibald Wheeler, who perfectly summarized GR nature: *"Spacetime tells matter how to move; matter tells spacetime how to curve. In other words, a bit of matter (or mass, or energy) moves in accordance with the dictates of the curved spacetime where it is located (a ball falling to Earth is responding to the curved spacetime in its vicinity). At the same time, that bit of mass or energy is itself contributing to the curvature of the spacetime everywhere (the falling ball is affecting spacetime and therefore affecting the motion of other bodies elsewhere)."* [244].

From a mathematical point of view, this concept is formalized by the Einstein field equations:

$$G_{\mu\nu} \equiv R_{\mu\nu} - \frac{1}{2} g_{\mu\nu} R = \frac{8\pi G}{c^4} T_{\mu\nu} \ . \tag{1.1}$$

On the left hand side, we have the geometrical ingredients of GR. The crucial ingredient in GR vision is hidden in the so-called Einstein tensor $G_{\mu\nu}$, and it is the metric of the space-time, a four dimensional tensor generally identified by the symbol $g_{\mu\nu}$. In GR, such tensor contains all the geometrical information of the space-time and as such, in Einstein vision, most of the information about how gravity works; in particular, it helps to define and characterize the entire causal structure of the space-time. The Einstein tensor is defined in terms of geometrical quantities which are directly related to the metric $g^{\mu\nu}$ and its derivatives with respect to the space-time coordinates: the Ricci tensor $R_{\mu\nu}$ and the Ricci scalar or the scalar curvature, $R = g^{\mu\nu} R_{\mu\nu}$.

While still hidden and not explicitly shown in such equations, in GR the classical Newton's gravitational force is explained by the curvature of the space-time characterized by its metric. Massive objects curve the space-time around them, and in that manifold, test particles in the absence of any force follow geodesics, which are the generalized notion of straight lines in flat space-time applied to curved cases.

On the right hand side, we have the other missing ingredient of GR: the energy-matter content of the Universe, represented by the stress-energy tensor $T_{\mu\nu}$, which sources the modification of the space-time geometry mainly as curvature effects. In the case of a perfect fluid in thermodynamic equilibrium, this tensor can be expressed in a simplified version as

$$T^{\mu}{}_{\nu} = \left(\rho + \frac{p}{c^2}\right) u^{\mu} u_{\nu} + p\, g^{\mu}{}_{\nu} \ , \tag{1.2}$$

where ρ and p are the energy density and pressure of the fluid, respectively, and u_{ν} is its four-velocity.

1.1.1 Cosmological Principle

The problem is that Einstein field equations are a set of nonlinear differential equations for which it is very hard to find a solution in even the simplest cases. Thus, for logical

reasons, and also for simplicity and practicality of the mathematical formulation, some assumptions are taken in cosmology regarding the symmetry of the space-like or spatial hyper-surfaces.

For instance, one assumes that the manifold can be sliced in space-like hyper-surfaces where the world lines of all fluid particles (4-dimensional paths) are orthogonal to them. Then, observers following those particles would measure the same *cosmic time* t [243]. These basic assumptions for the manifold are known as *Weyl's postulates* [190], though the additional condition for the world lines to be time-like geodesics is sometimes included.

For what concerns us, the main assumptions underlying the present cosmological scenario are: isotropy, uniformity in all orientations; and homogeneity, uniformity in all positions. Together they define the so-called *Cosmological Principle*. These starting hypothesis are well grounded ideas based partly on the Copernican principle, but also on observations.

Both homogeneity and isotropy are independent cosmological assumptions. There can be within GR Universes which are homogeneous but anisotropic, or even inhomogeneous but isotropic (spherically symmetric from an origin). From our particular point of view, from the Earth, it is easy to check that they might not be reasonable assumptions, as the Universe is filled of many gravitationally clustered structures, interspaced by almost totally empty regions of space.

But we are concerned here with the large scale of the Universe, where observations like CMB back up the isotropic assumption [109]. Homogeneity seems more difficult to test, requiring observations at large scale (around ~ 200 Mpc or beyond) when the galaxy distribution seems spatially homogeneous. However, in order to accept homogeneity, a logical deduction can also be done based on the Copernican principle, which states that our spot in the Universe is not a preferred nor special one. This last reasonable assumption can be tested [52, 65, 229, 253], and if considered true, it would mean that the isotropy we measured must be valid in every other point of the Universe, and thus, the universe should be homogeneous [109].

1.1.2 The metric of an expanding space-time

As anticipated above, the metric tensor defines the causal structure of the space-time manifold. The infinitesimal line element ds^2, i.e. the norm of the four-vector distance between two events infinitesimally close in space-time, is invariant and independent of the chosen coordinate system, dx^ν and is strictly related to the metric of space-time $g_{\mu\nu}$. In general, the metric $g_{\mu\nu}$ is a symmetric tensor and, assuming the so-called Einstein convention that repeated indexes are summed, we use to write the line element as

$$ds^2 = g_{\mu\nu} dx^\mu dx^\nu \ , \tag{1.3}$$

where μ and ν range along all dimensions of the working space-time, starting with the time-like coordinate which is associated with the index zero. Thus, in a four dimensional

space-time, the μ and ν indices range from 0 to 3, and in principle the metric has four diagonal and six off-diagonal components.

Therefore, the metric can be understood as the mathematical tool that turns the distance observed from any coordinate system into an invariant quantity, or more generally, it turns coordinate distances into physical distances. The form and components of the metric can be simplified by the several cosmological assumptions which were mentioned above. Considering all the symmetries implied by isotropy and homogeneity, the simplest space-time that fulfills them has the Minkowski metric. Using Cartesian coordinates, the Minkowski metric has the following form,

$$ds^2 = -c^2dt^2 + dx^2 + dy^2 + dz^2 \ , \quad \eta_{\mu\nu} = \begin{bmatrix} -c^2 & 0 & 0 & 0 \\ 0 & 1 & 0 & 0 \\ 0 & 0 & 1 & 0 \\ 0 & 0 & 0 & 1 \end{bmatrix} , \tag{1.4}$$

where c is the speed of light. The signature of the diagonal terms, $(-,+,+,+)$, shows us that the metric is Lorentzian, that is, its eigenvalues are all positive except for the temporal dimension. Although the opposite sign convention exists, both describe properly and equivalently the physical space-time. Nevertheless, the most common coordinate system that is used in cosmology is based on spherical coordinates. With the sign convention shown above, the Minkowski metric becomes

$$ds^2 = -c^2dt^2 + dr^2 + r^2d\Omega^2 \ , \quad g_{\mu\nu} = \begin{bmatrix} -c^2 & 0 & 0 & 0 \\ 0 & 1 & 0 & 0 \\ 0 & 0 & r^2 & 0 \\ 0 & 0 & 0 & r^2\sin^2(\theta) \end{bmatrix} , \tag{1.5}$$

where the solid angle is $d\Omega^2 = d\theta^2 + \sin^2(\theta)d\phi^2$. Thus, the two expressions above, Eqs. (1.4) and Eq. (1.5), are different representations in different coordinates of the same Minkowski space-time.

If we want to consider the isotropic expansion of the Universe, we can introduce the scale factor $a(t)$ as a function of cosmic time t, though usually the time dependence is taken implicitly, $a(t) \equiv a$. This function, as its name states, tells us how a physical distance between any two points scales through time, or equivalently, gives us the ratio of the physical distance between two same points observed at different times. Thus, intuitively, we see that there is a comoving distance between those two points, which is independent of the scale factor.

To better understand the picture, we can imagine the space as a grid like in Fig. 1.1. Points on this grid have their coordinates assigned in a particular system which is independent of its scaling; distances between those points in the grid are *comoving*

distances: they keep constant in time during the expansion of the grid as they only depend on the coordinates, not on the scale factor. On the other hand, due to the scale factor, the physical distance between two points increases with time even if the corresponding comoving distance is fixed.

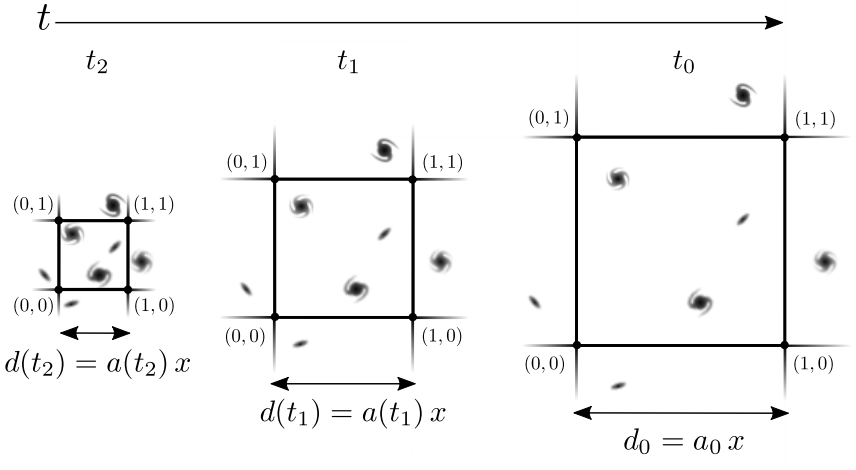

Figure 1.1: *During the evolution of time* $(t_2 < t_1 < t_0)$*, coordinates in the comoving grid remain constant* $(x = 1)$*. The physical distance, though, scales with the evolution of the scale factor* $(a(t_2) < a(t_1) < a_0)$ *expanding with time.*

As the Universe is expanding, we can normalize the value of the scale factor today, at time t_0, to one, i.e. $a(t_0) = a_0 = 1$, because it can be taken as a dimensionless quantity (the ratio of physical distance at different times). Therefore, in an expanding Universe any physical distance $d(t)$ in the past time t is $a(t)$ times smaller than today d_0, so $d(t) \equiv a(t)\, d_0 < a_0\, d_0 = d_0$ as we have $a(t) < a_0 = 1$ for any time in the past, $t < t_0$. Introducing this expansion in the above considered metric, we have, in Cartesian coordinates

$$ds^2 = -c^2dt^2 + a^2(dx^2 + dy^2 + dz^2)\ , \quad g_{\mu\nu} = \begin{bmatrix} -c^2 & 0 & 0 & 0 \\ 0 & a^2 & 0 & 0 \\ 0 & 0 & a^2 & 0 \\ 0 & 0 & 0 & a^2 \end{bmatrix}\ ; \qquad (1.6)$$

and in the case of spherical coordinates, the representation of this metric would be

$$ds^2 = -c^2dt^2 + a^2\left(dr^2 + r^2d\Omega^2\right)\ , \qquad (1.7)$$

where the matrix form would be similar to Eq. (1.5) but multiplying the spatial components

by the scale factor squared. Even if the original metric of Eqs. (1.4) - (1.5) represented a flat space-time, with null Riemann curvature tensor (4-curvature), the inclusion of this scale factor $a(t)$ makes its geometry quite different. Therefore, the final metric has a non-zero Riemann curvature tensor even though its spatial part remains flat. In fact, all the above metrics are spatially flat, though they can be easily generalized to a spatially curved case.

The Friedmann-Lemaître-Robertson-Walker metric

The metric shown in Eq. (1.7) is a particular case of a more general solution of the Einstein equations after assuming isotropy and homogeneity of the space-time, namely the Friedmann-Lemaître-Robertson-Walker (FLRW) metric. We note here that such FLRW metric can be derived by translating the general assumptions of isotropy and homogeneity into geometrical properties, in a quite independent way from the solution of the Einstein equations. What remains undetermined, however, is the intrinsic dynamics of the Universe expansion, encoded in the scale factor a, which can be derived only once we provide an energy-matter tensor and solve the field equations.

The most general FLRW metric, first introduced in 1935 by Robertson [191] and George Walker [235], is

$$ds^2 = -c^2dt^2 + a^2\left(\frac{dr^2}{1-kr^2} + r^2d\Omega^2\right) , \tag{1.8}$$

where k gives the signature of the spatial curvature. In the above case of Eq. (1.7), k was set equal to zero, and the metric had Euclidean space, so that the initial parallel trajectories of any free test particles kept going on parallel. In an closed Universe ($k = 1$; this choice implies a proper rescaling of r), the initial parallel trajectories of these particles converge. The most common example of closed space is Earth's surface, where all meridians meet at the poles though they are parallel at the equator. In the case of an open Universe ($k = -1$), the initially parallel path of these free test particles diverge instead and they never meet each other.

The spatial part of the metric can be interpreted as a spherical hyper-surface embedded in a four-dimensional Euclidean space; this hypersphere can be described by introducing a new angular coordinate χ. The expression of the FLRW metric in such hyperspherical coordinates is:

$$ds^2 = -c^2dt^2 + a^2\left(d\chi^2 + S_k^2(\chi)d\Omega^2\right) , \tag{1.9}$$

where the generalized sine S_k^2 is defined as

$$S_k(\chi) = \begin{cases} \sin(\chi) & \text{for } k = 1 \\ \chi & \text{for } k = 0 \\ \sinh(\chi) & \text{for } k = -1 \end{cases} \tag{1.10}$$

with the range of $0 \leq \chi \leq \pi$ for a closed Universe ($k = 1$) and $0 \leq \chi \leq \infty$ for an open

($k = -1$) or flat ($k = 0$) Universe.

Friedmann equations

Computing Einstein's fields equations using a perfect fluid in the comoving rest frame and assuming the FLRW metric from Eq. (1.8), we obtain the equations which make us possible describe how the Universe behaves on large scales.

The first equation can be derived by imposing the conservation of the total energy-momentum, $\nabla^{\mu} T_{\mu\nu} = 0$, which leads to the well known continuity equation. In the case of an expanding Universe using the FLRW metric of Eq. (1.8) or Eq. (1.9), the scale factor and its time derivative appear in the equation in the following way,

$$\dot{\rho} + 3\,\frac{\dot{a}}{a}\left(\rho + \frac{p}{c^2}\right) = 0\,. \tag{1.11}$$

From the time-time component of Einstein's equations in Eq. (1.1), we derive the first Friedmann equation, which is enough to understand the evolution of the scale factor on cosmological scales at the so-called background level, and which will be employed in the following sections to calculate the variously defined cosmological distances. It states that

$$\left(\frac{\dot{a}}{a}\right)^2 = \frac{8\pi G}{3}\rho - \frac{kc^2}{a^2}\,. \tag{1.12}$$

The trace of Einstein's equations, Eq. (1.1), provides us the second Friedmann equation (also known as Raychaudhuri equation)

$$\frac{\ddot{a}}{a} = -\frac{4\pi G}{3}\left(\rho + \frac{3p}{c^2}\right)\,. \tag{1.13}$$

Conservation of the energy-momentum is implicit in the Einstein field equations, as the continuity equation of Eq. (1.11) can be obtained by differentiating Eq. (1.12) and combining the result with Eq. (1.13). Thus, from these three equations only two are independent, and usually for cosmology the continuity equation, Eq. (1.11), and the first Friedmann's equation, Eq. (1.12), are employed.

1.2 Connecting theory to observations

The most common and used function to parametrize the expansion of the Universe is the Hubble function, $H \equiv \dot{a}/a$, but we have to specify also the energy content of that Universe and its evolution. If the entire energy budget of the Universe is constituted by different species that do not interact with each other, the continuity equation of Eq. (1.11) is fulfilled separately for each cosmic ingredient. Otherwise, coupled continuity equations

must be solved. Nevertheless, we can integrate them to obtain the time evolution of the energy density for each cosmic species.

All the cosmic constituents that we will include in this work will be considered as perfect fluids, whose characterization can be done solely by their density and pressure. If there is an equation of state (EoS) $p_i = w_i \rho_i c^2$ relating both quantities, given by the EoS parameter (function) w_i, that species is considered a barotropic fluid. This means that its density is a function of its pressure only, a good approximation for fluids whose density is almost constant in space (as it should be on very large cosmological scales) and/or varies very weakly with temperature. Thus, as homogeneous perfect fluids can be considered barotropic ones, the conservation equation for each cosmic ingredient, once introduced the EoS parameter, has the following form

$$\dot{\rho_i} + 3\,\frac{\dot{a}}{a}\rho_i\,(1 + w_i) = 0\ , \tag{1.14}$$

which can be easily solved in the case of a constant w, to obtain the evolution of the energy density as

$$\rho_i \propto a^{-3(1+w_i)}\ . \tag{1.15}$$

This function shows us that unless $w_i < -1$, the energy density of the fluid decreases as the Universe expands with time. In the special case for a fluid with $w_i = -1$, its energy density remains constant through time. We have to set a reference point in order to fix the integration constants of these density functions. That reference point is usually taken today (t_0), so the function that gives the evolution of the density has the following form

$$\rho_i = \rho_{i,0}\, a^{-3(1+w_i)}\ , \tag{1.16}$$

where $\rho_{i,0}$ is the energy density of the fluid today and the value of the scale factor toady is implicit ($a_0 = 1$).

The above case is obviously valid only for a fluid which has a constant EoS parameter. This is how the most well understood cosmic ingredients (matter, radiation) behave, but the elusive dark energy could have an evolving EoS, though a cosmological constant with $w = -1$ is nowadays considered as the most probable candidate to it (we will give a short sketch of present dark energy scenarios and theories in next sections). So, in the case of a fluid whose EoS evolves through time, the integration of the continuity equation of Eq. (1.14) yields

$$\rho_i \propto \exp\left(-3\int \frac{da'}{a'}\,[1 + w_i(a')]\right)\ . \tag{1.17}$$

As we have said, the energy content of the Universe shapes its geometry. Therefore, rewriting the first Friedmann equation, Eq. (1.12), and introducing the Hubble function

$$H^2 - \frac{8\pi G}{3}\rho = -\frac{kc^2}{a^2}\ , \tag{1.18}$$

we can see that there is a critical density which gives a spatially flat Universe for any value of the scale factor,

$$\rho_c \equiv \frac{3H^2}{8\pi G} \, . \tag{1.19}$$

A Universe with a total energy density content above this value is spatially closed, whereas one with a lower density is open. This critical density is a proper reference quantity to define dimensionless density parameters[1],

$$\Omega_i(a) \equiv \frac{\rho_i(a)}{\rho_c(a)} = \frac{8\pi G}{3H^2}\rho_i(a) \, , \tag{1.20}$$

where this relation is valid for every cosmic component. In total analogy, we also define a dimensionless curvature parameter, as

$$\Omega_k(a) = -\frac{kc^2}{a^2H^2}; \tag{1.21}$$

thus, the first Friedmann equation can be recast in an equivalent form as

$$\sum_i \Omega_i(a) + \Omega_k(a) = 1 \, . \tag{1.22}$$

Note that this relation holds at any time.

The first Friedmann equation can be also written in a more observational-friendly shape, which is completely equivalent to the previous one, but making the time behavior explicit for all and each component. From the definition Eq. (1.20), we can write

$$\Omega_i(a) \equiv \frac{\rho_i(a)}{\rho_c(a)} = \frac{H_0^2}{H^2}\frac{\rho_{i,0}}{\rho_{c,0}}\, a^{-3(1+w_i)} = \frac{H_0^2}{H^2}\, \Omega_i \, a^{-3(1+w_i)} \, , \tag{1.23}$$

where $\Omega_i = \rho_{i,0}/\rho_{c,0}$ is the density parameter evaluated today. Such parameters are actually measurable from observations (once a cosmological model is provided). Substituting this expression in the first Friedmann equation, either Eq. (1.12) or Eq. (1.22), we reach the most common expression for the Hubble function

$$H^2 = H_0^2 \left(\sum_i \frac{\Omega_i}{a^{3(1+w_i)}} + \frac{\Omega_k}{a^2} \right) \, , \tag{1.24}$$

where H_0 is the Hubble constant today (sometimes written as $H_0 = 100\, h$). If we evaluate this Hubble function today, $a = 1$, we get the following constrain,

$$1 = \sum_i \Omega_i + \Omega_k \, . \tag{1.25}$$

[1]We will use the following convention: time dependent densities will generically be expressed as $\Omega_i(a)$; densities evaluated now will be expressed as Ω_i, with no additional symbols and/or suffixes.

1.2.1 Cosmic Inventory

As illustrative examples, now we consider the main cosmic ingredients included in all the main and most widely used cosmological models, and we will check how they influence the expansion of our Universe.

Matter

Matter, both dark or baryonic, is modeled as a pressure-less fluid or dust. As such, its EoS parameter is $w = 0$ and its cosmological behavior is given by solving Eq. (1.16), i.e.

$$\rho_m(a) = \rho_{m,0}\, a^{-3}\,. \tag{1.26}$$

In this expression, we can see how the energy density of the fluid is diluted in the expansion of the Universe.

The case in which matter is the dominant constituent of the Universe is known as Einstein-de Sitter Universe: taking a flat Universe full of matter, thus having only $\Omega_m = 1$, the Hubble function of Eq. (1.24) simplifies to

$$\dot{a}^2 = \frac{8\pi G \rho_{m,0}}{3}\frac{1}{a}, \tag{1.27}$$

which can be integrated in order to solve the time evolution of the scale factor. Considering the initial conditon of $a(t_0) = 1$, we have

$$a(t) = \left(\frac{t}{t_0}\right)^{2/3}\,, \tag{1.28}$$

or, equivalently

$$\rho_m(t) = \rho_{m,0}\left(\frac{t_0}{t}\right)^2\,, \qquad\qquad H = \frac{2}{3t}\,. \tag{1.29}$$

Radiation

Radiation includes mainly photons, but relativistic particles as cosmic neutrinos are also in it. It has $w = 1/3$, which leads to the following density parameter

$$\rho_r(a) = \rho_{r,0}\, a^{-4}\,; \tag{1.30}$$

radiation does not only dilute its density as in the matter case due to the cosmic expansion, but also its associated wavelength is stretched. Therefore, the temperature of the radiation decreases with time as its wavelength expands with the Universe.

In a flat Universe full of radiation, so with only $\Omega_r = 1$, the Hubble function of Eq. (1.24) can be written simply as

$$\dot{a}^2 = \frac{8\pi G \rho_{r,0}}{3} \frac{1}{a^2}, \tag{1.31}$$

which can be integrated in order to solve the time evolution of the scale factor. Considering the initial conditon of $a(t_0) = 1$, we have

$$a(t) = \left(\frac{t}{t_0}\right)^{1/2} , \tag{1.32}$$

or, equivalently

$$\rho_r(t) = \rho_{r,0} \left(\frac{t_0}{t}\right)^2 , \qquad H = \frac{1}{2t} . \tag{1.33}$$

Cosmological constant

In the case of a cosmological constant Λ, its EoS parameter is $w = -1$ and according to the energy density evolution equations seen above (Eq. (1.14) or Eq. (1.15) for example), its energy density does not evolve with time. In the case of a flat Universe filled only with it, so with only $\Omega_\Lambda = 1$, the Hubble function of Eq. (1.24) simplifies to

$$H^2 \equiv \left(\frac{\dot{a}}{a}\right)^2 = H_0^2 . \tag{1.34}$$

Taking into account that $a(0) = 0$ cannot be set as initial condition, the integration leads to an exponential solution,

$$a(t) \propto \exp\left(H_0\, t\right) . \tag{1.35}$$

Thus, as the exerted negative pressure proportional to its density is kept constant through time, a Universe filled with only the cosmological constant has an exponential expansion.

Generic single fluid

In general, for a single cosmological fluid with a constant EoS parameter w, its energy density is

$$\rho_X(a) = \rho_{X,0}\, a^{-3(1+w_X)} , \tag{1.36}$$

and the Hubble function of Eq. (1.24) has the form of

$$\dot{a}^2 = \frac{8\pi G \rho_{X,0}}{3} \frac{1}{a^{-2+3(1+w_X)}}, \tag{1.37}$$

with $\Omega_X = 1$ being the only term considered in this flat Universe. Taking the same initial condition as before, $a(t_0) = 1$, the integration gives

$$a(t) = \left(\frac{t}{t_0}\right)^{\frac{2}{3(1+w)}} . \tag{1.38}$$

We can see how its value of the EoS parameter w modifies the evolution of the expansion of the Universe. This formula is valid for all the above cases except for the cosmological constant.

1.3 Dark energy and Dark matter: a short excursus

Given all these preliminary ingredients, we have now to work out a cosmological model which is consistent with observations. Nowadays, we do have a *consensus* model, the Λ-Cold Dark Matter (ΛCDM) model, which is so far the best *effective* model to explain the majority of the data we have collected both at cosmological and astrophysical scales. The latest confirmation of such privileged status has come from the last data release from the *Planck* satellite [6]. It has to be pointed out also that the main pillar of the ΛCDM model is the assumption that GR was the ultimate theory of gravity. This is by far a "huge" inference itself, if we consider that GR has been well-tested only in a really narrow scale range [245] (from Solar System to Nucleosynthesis) of four order of magnitudes; but what it is done daily is to supposedly assume that to apply GR on a range of scales of 60 orders of magnitude is the proper and only way to do cosmology.

Once GR is assumed, at least the 95% [6] of the matter and energy in the Universe is in some "dark" form: DE should account for $\sim 68\%$ of the energy budget in the Universe and lead its accelerated expansion, discovered in [178, 186]; DM should account for $\sim 27\%$ of the matter budget in the Universe and be responsible for the extra gravitational attraction we can detect in almost all the astrophysical gravitational structures we can observe nowadays in the cosmological large scale structure. The name of the consensus ΛCDM model refers exactly to what are the best candidates, up to now, for DE and DM: the cosmological constant Λ as DE; and the Cold Dark Matter.

In the ΛCDM model, the *easiest* way to explain DE is through the cosmological constant Λ, which should be a measure of the energy density of the vacuum, its state of lowest energy [56]. The conditional mode "should" is obligatory at this stage because if Λ was really the vacuum energy, then it is well known that its value calculated using tools from particle physics and quantum field theory does not agree with the observed one by 122 orders of magnitude (such discrepancy might be lower, ~ 54, but still present and quite problematic [164]). Despite this and other theoretical problems (for a more exhaustive list, see [50]), the cosmological constant is nowadays considered the best candidate for DE, for its intrinsic simplicity both from a theoretical point of view and from a statistical one when it comes to apply theoretical models to observational data.

By the way, such cast doubts have pushed cosmologists to find out other solutions. The most conservative alternatives still rely on GR, namely, they save its geometrical part, but modify the energy-matter contribution, generally adding phenomenologically one or more scalar fields with some given properties, and whose existence, however, has to be explained somehow [24, 69, 140, 150]. Generally they can be classified by their equation of state, which relates their pressure to their density by a parameter, the equation-of-state parameter w. For example, Λ has $w = -1$. Some possible candidates (in an absolutely non-exhaustive list) are [69, 176]: *quintessence*, with $w = const. \neq -1$, a scalar field minimally coupled to gravity and whose potential drives the accelerated expansion; *K-essence*, where the modified kinetic energy of the field is the source of the acceleration; *phantom* fields, with $w < -1$ and negative kinetic energy, which are really problematic from the theoretical point of view, leading to singularities and instabilities, but are apparently favored by the statistical analysis of low redshifts cosmological probes; *quintom* models, dynamical scalar fields which can move from quintessence to phantom; fields which couple DE with baryons and/or DM [17]; Chaplygin gas [130]. Finally, we cannot avoid to mention also the equally numerous phenomenological parameterizations of DE, based on the proposal of some dynamical w without any previously-given theoretical background, but just with the desired property of being able to provide a satisfactory fit of the cosmological data. The most famous parametrization in this case is for sure the Chevallier-Polarski-Linder (CPL) model [59, 154], the simplest possible dynamical w, being it a linear (in the scale factor) interpolation between the unknown values of w at the present and in the asymptotic past. More examples can be found in [17].

The less conservative side of the scientific community, instead, considers GR *"only"* as a special limit of a more general theory of gravity, so that now both geometry and matter are susceptible to modifications. Such theories are interchangeably called "modified", "alternative" or "extended" theories of gravity (ETG) [38, 66]. Possibly, in this case we have even more models to propose, because of the very large number of degree of freedoms and ways to extend GR while having one very important constraint: ETGs have to reduce to GR on scales where we know GR works perfectly, like in the Solar System, with probes ranging from the historical Einstein's calculations about Mercury perihelion shift and deflection of stars light by the Sun, to more recent measurements of the frame-dragging effect from the *Gravity Probe B* mission [245]. But we will not deepen this aspect in this work, sticking to GR solutions to the DE problem.

For DM the situation is equally muddled. Historically speaking, we have been knowing of a missing matter contribution since the 30's, when a discrepancy between the observed and the theoretically-derived dynamical mass of galaxy clusters was found by [256]. Later on, the pioneering works on rotation curves of spiral galaxies showed the same discrepancy [195, 196]. The conclusion of such studies was that the internal dynamics of such self-gravitating systems was not possible to be sustained only by the ordinary observable mass, but it needed the additional contribution of some new and not yet identified kind of matter which, apparently, was interacting with photons and ordinary baryonic matter only by gravitational interaction. Since then, we have been accumulating further and further evidence for the existence of DM both at cosmological and astrophysical scales and in

parallel a long list of candidates for DM has been compiled [39, 55, 85, 158, 179].

From some point of view, DM poses less problems than DE because no new kind of interaction, different from any which we already know, is automatically needed: the minimal and necessary requirement is that DM does not interact electromagnetically with light and ordinary matter (baryons) but for sure gravitationally, at least. Thus, we don't necessarily need to break down our knowledge of physics to introduce new exotic types of interactions, as it happens in the case of DE, and we can try to formulate everything within the borders of the Standard Model of Physics (SM), or with just some minimal extension. But this also poses an equally serious challenge to DM supporters: if that was the case, we should be able indeed, sooner or later, to detect these new particles. Looking at the present status, it seems that it might be better later than sooner. An absolutely non-exhaustive list of DM candidates could be (for more details and examples, see [39]):

- Massive Compact Halo Objects (MACHOs) – stellar objects too faint to be observed, like brown dwarfs, white dwarfs and neutron stars. Today this model is almost quite completely discarded, because even if MACHOs were effectively able to contribute to DM, they would not be enough to explain all the amount we detect and its properties.
- Weakly Interacting Massive Particles (WIMPS) – particles which interact via gravity and the weak force, or other kinds of force at least as weak as the weak one. Among them we have: nonbaryonic particles from within the SM like neutrinos which, by the way, have been proved to be too light to be important at cosmological scales; particles from supersymmetry (SUSY) and in particular from the minimal supersymmetric extension of the Standard Model, as neutralinos, gravitinos, axinos.
- Axions – particles which solve the strong-CP problem in SM. In a recent variant [33], axion DM can behave as a superfluid and supposedly unify the successes of MOND at galactic scale with those of the ΛCDM at cosmological scales.
- Sterile neutrinos – beyond SM particles which would interact with ordinary matter only and exclusively by gravitational interaction, with no other standard interaction involved.
- Kaluza-Klein DM – this model is somehow related to the notion of extra dimensions used to explain DE, but within inherently different scenarios. In this context, gravity and the other SM fields propagate in a higher-dimensional space-time (the bulk), and some states associated to excitations of such fields in the bulk could be linked to DM particles [39].

On top of that, we have also to recognize a more general classification of DM candidates, primarily related to the velocity of the DM particles and, thus, to their free streaming length or, equivalently, to the characteristic length of possible self-gravitating structures which could form from clustering processes. We have:

- hot dark matter (HDM), made of particles with ultra-relativistic velocities and thus near-zero mass; they should be able to create large structures but not small clustered ones, which should come from fragmentation in a top-bottom scenario.

As such, they are not in agreement with observations;

- cold dark matter (CDM) includes sub-relativistic particles with larger masses than HDM ones: they are able to create smaller scale structures which could evolve in larger ones by merging processes. This scenario seems to be in better agreement with observations and, for that reason, CDM is considered the preferred candidate for DM in the consensus ΛCDM model;
- warm dark matter, with intermediate properties between hot dark matter and CDM; fuzzy dark matter.

The ΛCDM model explains all the main observational data at cosmological level with great precision and details. At background level its simplicity outperforms other models explaining the observed geometry of the Universe. Besides, its perturbation theory explains the anisotropies seen on the CMB and most observations regarding the matter power spectrum of galaxies. The combined constraints of the model's parameters are nowadays very strong thanks to the extreme precision achieved by the space telescopes measuring the CMB power spectrum, and supported by big supernovae and galaxy catalogs. Nowadays, we have confirmation from: luminosity distances from Type Ia Supernovae (SNe) [40, 178, 186, 220]; the acoustic peaks in the Cosmic Microwave Background (CMB) [5, 236]; and their counterpart imprinted in clustered matter, i.e. Baryon Acoustic Oscillations (BAO) [8, 9, 44, 91, 97]; or through the matter power spectrum obtained from weak lensing [26, 241].

With the most common cosmic ingredients explained above, the Hubble function of Eq. (1.24) has the following form for the ΛCDM case

$$H^2_{\Lambda CDM} = H_0^2\, E^2(a) = H_0^2 \left(\frac{\Omega_m}{a^3} + \frac{\Omega_r}{a^4} + \Omega_\Lambda + \frac{\Omega_k}{a^2} \right) , \tag{1.39}$$

where matter accounts for both dark and baryonic matter. It is very common to assume a spatially-flat Universe, as the curvature is strongly constrained to zero by CMB data. Both dark and baryon matter are to be constrained by the corresponding parameters, $\Omega_m = \Omega_{DM} + \Omega_b$, and the density of dark energy in ΛCDM is completely described by $\Omega_\Lambda = 1 - \Omega_m - \Omega_r - \Omega_k$. The density of the photons is computed through the photon-baryon ratio and the CMB temperature (we will make it explicit in next sections).

2 Cosmological Observables

In this chapter, we will first introduce the definition of cosmological distances [115], which are of capital importance in modern cosmology, and then we will describe the observational probes which can be used nowadays to measure them, and which can be then used to quantify the dynamics of the expansion of our Universe and to provide constraints on any cosmological model proposal. We will describe the two main types of observations which are fit to that purpose, namely the standard candles, objects for which we know their intrinsic luminosity, and the standard rulers, objects for which we know their physical size. Any of them allows us to measure cosmological distances, and thus, to map the geometry of the universe.

2.1 Distances in Cosmology

The key requirement for a proper quantification of the expansion of the Universe at the background level is a procedure to measure cosmological distances. Obviously, we are unable to calculate the real physical distance between us and any other object in the space which is located at scales useful for our goals. Thus, we can only rely on indirect cosmological distances; as expected, their own definition is not an easy issue.

The most basic and simple definition of distance is obviously related to the path that light has been able to travel during a certain time period. In a FLRW metric, see Eq. (1.9), a line-of-sight or radial ($d\Omega = 0$) light-ray is defined by $ds^2 = 0$, which yields $c\,dt = -a(t)\,d\chi$ for an incoming photon. The total distance travelled by a photon emitted at time t_e and collected at time t_o is thus given by

$$\chi = c \int_{t_e}^{t_o} \frac{dt'}{a(t')} \,. \tag{2.1}$$

This distance is called *comoving distance* in complete similarity with the definition of comoving coordinates: it is not changing in time due to expansion, having been it factored out of the definition. A particular case is played by the total distance that light has

traveled since the beginning, i.e. $t_e = 0$, which is also known as *particle horizon*,

$$\mathcal{H}_p \equiv c \int_0^t \frac{dt'}{a(t')} \, . \tag{2.2}$$

This distance is important because no information could have propagated beyond it; thus, regions separated by more than this distance would be causally disconnected from each other.

Redshift

Hitherto, we have seen that the evolution of the Universe can be traced by several possible "evolutionary" variables, as for example the cosmic time t or the scale factor a. However, when dealing with observational data, it is more useful and straightforward to introduce another variable that tracks the passing of cosmic time, namely, the *cosmological redshift*, because it is a quantity which can be easily measured.

The redshift is defined as the fractional shift in wavelength of a photon emitted by a distant source in the past with wavelength λ_e, and detected later by an observer when that very photon has wavelength λ_o,

$$z = \frac{\lambda_o - \lambda_e}{\lambda_e} \, . \tag{2.3}$$

The two wavelengths are not the same, because during the evolution of the Universe, the expansion of the space-time stretches every wavelength, shifting their value towards the red end of the spectrum and thus decreasing the energy of photons.

While Eq. (2.3) is the operative way to define the redshift, we also need to relate it to other cosmic time variables. Let us consider the comoving distance defined as in Eq. (2.1): then, a light-ray which is emitted at time t_e and observed today at t_o will travel the same comoving distance as another light-ray emitted from the same location but at a slightly later time $t_e + \delta t_e$, and will be observed at $t_o + \delta t_o$, so that

$$c \int_{t_e}^{t_o} \frac{dt}{a(t)} = c \int_{t_e+\delta t_e}^{t_o+\delta t_o} \frac{dt}{a(t)} \, . \tag{2.4}$$

Thus, by the definition of the comoving distance, both integrals must be equal; rearranging properly their integration limits we get

$$c \int_{t_e}^{t_e+\delta t_e} \frac{dt}{a(t)} + c \int_{t_e+\delta t_e}^{t_o} \frac{dt}{a(t)} = c \int_{t_e+\delta t_e}^{t_o} \frac{dt}{a(t)} + c \int_{t_o}^{t_o+\delta t_o} \frac{dt}{a(t)} \, , \tag{2.5}$$

and simplifying it, we are left with the condition

$$c\int_{t_e}^{t_e+\delta t_e}\frac{dt}{a(t)} = c\int_{t_o}^{t_o+\delta t_o}\frac{dt}{a(t)}\ . \tag{2.6}$$

If the time intervals are small enough compared to the observation and emission cosmic times ($\delta t_e, \delta t_o \ll t_e, t_o$), the above equality can be well approximated by

$$\frac{c\,\delta t_e}{a(t_e)} = \frac{c\,\delta t_o}{a(t_o)}\ . \tag{2.7}$$

The small spatial intervals in the numerators correspond exactly to the emitted and observed wavelengths of the light-rays ($c\,\delta t \equiv \lambda$) considered, and their ratio at each pair of emission and observation events is the same as the ratio of the scale factors at those same times,

$$\frac{a(t_o)}{a(t_e)} = \frac{c\,\delta t_o}{c\,\delta t_e} = \frac{\lambda_o}{\lambda_e}\,. \tag{2.8}$$

The above ratios, alongside Eq. (2.3), lead to the well known relation between the emitted and observed radiation wavelengths and the scale factor:

$$\frac{a(t_o)}{a(t_e)} = \frac{\lambda_o}{\lambda_e} = 1 + z_e(t_o)\ , \tag{2.9}$$

which, as we remind here, holds only for the FLRW metric case we have been considering so far.

Comoving Distance

We have defined the comoving distance and redshift in Eq. (2.1) and in Eq. (2.9), respectively, where the emission and observation times have not been fully specified. Leaving the emission time free to depend on the source, we can set the observation time t_o at Earth as the age of the Universe today, $t_o \equiv t_0$. Thus, the basic building block for the rest of cosmological distances is achieved by simply changing the integration limits of the above Eq. (2.1),

$$D_C \equiv \chi = c\int_{t}^{t_0}\frac{dt'}{a(t')} = c\int_{a}^{a_0=1}\frac{da'}{a'^2 H(a')}\ , \tag{2.10}$$

where the integration over time t has been changed to integration over scale factor a, using the definition of the Hubble function given in Sec. 1.2. A further change of variables from scale factor to redshift, takes us to the following form

$$D_C(z) = D_H\int_0^z\frac{dz'}{E(z')}\ , \tag{2.11}$$

where $D_H \equiv c/H_0$ is the so-called Hubble distance and $E(z) \equiv H(z)/H_0$ is the dimensionless Hubble function. Up to this point, all the distance definitions rest on the assumption of a radial light-ray, which are different from the comoving *transverse* distance.

The comoving distance between two points in the sky separated by some angle $\delta\theta$ but located at the same radial distance from the observer ($d\chi = 0$ and constant χ) is $S_k(\chi)\,\delta\theta$, according to the notation of the metric in Eq. (1.9) (having set the observation time today, $a_0 = 1$). Taking into account the spatial curvature, the transverse comoving distance D_M can then be written in terms of the previous radial line-of-sight comoving distance D_C as

$$D_M(z) = \begin{cases} \frac{D_H}{\sqrt{\Omega_k}} \sinh\left(\sqrt{\Omega_k}\,\frac{D_C(z)}{D_H}\right) & \text{for } \Omega_k > 0 \\ D_C(z) & \text{for } \Omega_k = 0 \\ \frac{D_H}{\sqrt{|\Omega_k|}} \sin\left(\sqrt{|\Omega_k|}\,\frac{D_C(z)}{D_H}\right) & \text{for } \Omega_k < 0 \end{cases} \tag{2.12}$$

where the dependence on the spatial curvature is given by the corresponding parameter Ω_k introduced in Sec. 1.2.

The comoving distance is basically impossible to be directly measured. Thus, we need to rely on alternative but strictly related other types of distances, whose definition will be based on some specific indicators.

Angular diameter distance

Since the beginning of astronomy, a classical way to measure distances in the sky was through *parallax distance*. These measurements are inferred by the relative motion that the observed object shows in the sky with respect to the distant fixed background and due to Earth orbiting around the Sun. This apparent shift of position can be measured through the parallax angle, a small variation in the angular position of the observed object on the sky plane. By simple trigonometry, this angle can be then converted in a length once/if the distance that the observer has displaced perpendicular to the direction of observation is known [75, 242]. When the object under observation shows a parallax angle of one arc-second due to Earth's mean orbit of one astronomical unit (1AU) around the Sun, by definition the object is said to be at a distance of one *parsec* from Earth (3.26 light-years).

An equivalent definition can be found for the cosmological *angular diameter distance* D_A, where the size of the observed object is used as a ruler instead of the distance between the Earth and the Sun. Thus, measuring the angular size α observed in the sky corresponding to a certain object of *known physical transverse size* l, the angular diameter distance D_A can be also trigonometrically obtained. In principle, as long as the observed angle α is small, the angular diameter distance can be obtained through the relation

$$D_A = \frac{l}{\alpha}\,. \tag{2.13}$$

This transverse distance l can be measured in the comoving frame in terms of the line element ds^2 of Eq. (1.9), centering its origin around the observer. Taking into account that this distance l is the physical length of the observed object, in terms of the definition of transverse comoving distance above in Eq. (2.12), the physical transverse size of the object is

$$l = ds = a\, D_M\, d\theta \ . \tag{2.14}$$

The previous observed angle α and this angle $d\theta$ of the metric are the same, $d\theta \equiv \alpha$, as both are computed using the same radial propagating light-rays. The physical transverse size l of the observed object, instead, keeps constant during the expansion of the Universe. If we substitute this last definition of the physical size l in terms of the comoving coordinates in the previous definition of the angular diameter distance of Eq. (2.13), the angle gets simplified away and the relation between the angular diameter distance D_A and the transverse comoving distance D_M can be obtained:

$$D_A = a\, D_M = \frac{D_M}{1+z} \ . \tag{2.15}$$

Here we can clearly see how objects in the far past ($a \to 0$ or $z \to \infty$) appear closer, with a smaller angular diameter distance, and thus bigger.

Luminosity distance

The other commonly used cosmological distance is the luminosity distance D_L. Knowing the intrinsic luminosity L of a source, that is, the total energy emitted per unit time, the luminosity distance can be inferred by measuring its observed flux F, the energy density per unit time per unit area. The luminosity distance is defined so that it fulfills the well-known inverse-square law distance relation between the luminosity L and the flux F,

$$D_L = \left(\frac{L}{4\pi F}\right)^{1/2} \ . \tag{2.16}$$

This means that integrating the flux F over a closed spherical shell, or simply multiplying the flux by its area in the case of isotropic emission, the intrinsic luminosity L is recovered. If we now center the origin of the metric of Eq. (1.9) in the luminous source, and locate our detectors at the surface of the same sphere, we can easily see that the radius of the spherical shell is given by $a_0 S_k(\chi)$ or, equivalently, considering $a_0 = 1$, by the transverse comoving distance D_M, being the area $4\,\pi\, D_M^2$ and thus

$$F = \frac{L}{4\pi D_M^2} \ . \tag{2.17}$$

Therefore, the luminosity distance would be equivalent to the transverse comoving distance, but only in an static Universe. In the case of an expanding Universe, we have to take into account both the photon energy loss and the increase of the spherical physical surface.

The photon energy is diluted inversely proportional to the scale factor a, so the photons detected now have $\propto 1+z$ less energy than when they were emitted. Similarly, as the spherical surface is larger now than in the past, the number of photons crossing the surface now is $\propto 1+z$ smaller. Accounting for both effects, we have that the measured flux now is in fact

$$F = \frac{a^2 L}{4\pi D_M^2} \,, \tag{2.18}$$

where L is still the intrinsic luminosity of the source. Substituting this expression of Eq. (2.18) for the flux in the definition of the luminous distance D_L of Eq.(2.16), we have the relation

$$D_L = \frac{D_M}{a} = (1+z) D_M \,. \tag{2.19}$$

2.2 Standard Candles

In a Universe with scarcity of references to measure distances, one can compute the luminosity distance only if the intrinsic brightness of an object is known. The astronomical objects which have a known brightness, or for which at least we have been able to develop a system to infer it, are called standard candles. In fact, the precise known brightness must almost always be calibrated first, as the intrinsic luminosity of the object and its distance from us are correlated: a certain astronomical body which is fainter than expected could be or fainter or farther, with the same consequences.

For this reason, the astronomical community has put a lot of effort to build up a sort of *cosmic distance ladder* in terms of cosmological distances, where the calibration of the farther objects is performed by using closer ones in a range of distances (i.e. redshifts) where both distance indicators are overlapping. The most common example is the SNe Ia calibration using Cepheids, where the closest supernovae are calibrated with overlapping Cepheids in order to extend beyond the useful range provided by the SNe Ia. However, one can follow down to the very first rungs of the cosmic distance ladder, where the closest Cepheids are calibrated mainly using parallax distance measurements [94, 231].

Extending this procedure to larger scales, we can calibrate cosmological distances. Anyway, in the observations of standard candles, different electromagnetic wavelengths must be considered, as well as other details as dust absorption. Thus, the above derivation for the luminosity distance and the following standard candle definition have more subtleties than sketched here.

Magnitudes

The observable from which the luminosity distance information is extracted is built around the magnitudes, negative logarithmic scales for the observed brightness (i.e. radiant flux) of the astronomical objects. The apparent magnitude m is by definition the flux of any celestial body F compared logarithmically to a defined zero point offset flux F_0, the one

defined to give zero magnitude produced by a charted source:

$$m = -2.5 \log_{10} \left(\frac{F}{F_0} \right) \ . \tag{2.20}$$

There are several objects used as zero point offset sources. That point varies depending on the technology and filters used in the observation, but historically the most common is the Vega star. Nevertheless, the apparent magnitude can always be expressed as a function of the flux F of the observed object,

$$m = -2.5 \log_{10} F + constant \ , \tag{2.21}$$

where the constant accounts for the zero point offset source (used in the observation). An analogous relation is defined for the absolute magnitude M, but related to the intrinsic luminosity L of the observed object instead of its flux,

$$M = -2.5 \log_{10} L + constant \ . \tag{2.22}$$

In this case, the constant is defined so that the absolute magnitude is equal to the apparent magnitude of the same source as if it were located at a distance of 10 pc. Taking into account the flux's inverse square relation with the distance, the difference between both magnitudes is

$$m - M = 5 \log_{10} \left(\frac{D_L}{10\, pc} \right) \ , \tag{2.23}$$

where D_L is the luminosity distance defined in the previous Sec. 2.1. This quantity is called the *distance modulus* μ, and usually is used with the luminosity distance given in megaparsecs (Mpc), which simply transforms the relation to,

$$\mu = m - M = 5 \log_{10} D_L(Mpc) + 25 \ . \tag{2.24}$$

This distance modulus μ is the main quantity that catalogs relying on standard candles generally report.

2.2.1 Cepheids

These variable bright stars were the very first standard candles, used to measure distance within our galaxy or local group, and the first step in the cosmic ladder beyond parallax measurements. Cepheids are variable stars with radial pulsations whose high luminosity makes them perfect tools for distance estimation of mainly the local group galaxies, although the introduction of new technologies during late 80s made it possible to infer distances for galaxies further away [98, 99]. Though there are many variables stars identified nowadays [221], classical Cepheids are easily distinguishable due to their characteristic pulsations varying their brightness and color [228]. Their basic physics is quite well understood; for further insights, see the reviews [161, 203, 222] and references therein.

The first period-luminosity relation traces back to 1912 [144], but it has been repeatedly improved since; first with the connection of the color (or temperature) to both the period and the luminosity of the pulsation [202]; but then including also metallicity [198]. Keeping it simple, though, the linearized form of the relation is given by Stefan's law

$$L = 4\pi R^2 \sigma T_e^4 \,, \tag{2.25}$$

where the intrinsic luminosity L of the variable star is given by the effective temperature T_e at its surface of area $4\pi R^2$, depending on the radius R. Expressing Stefan's law in absolute magnitude, we have

$$M = -5 \log R - 10 \log T_e + C \,, \tag{2.26}$$

where the C term includes all the constants involved. Through the mechanical analysis of a spherical fluid object, a relation between the fundamental pulsation period P and the mean density ρ can be reached, it being $P \propto \rho^{-1/2}$ [83]. This relation can be used in order to constrain the system by its period P instead of the radius R, as its density ρ is related to both the radius and temperature. When this temperature T_e is also expressed in terms of the color (B-V for example), a relation for the observable period-luminosity-color (PLC) is achieved [161]:

$$M = \alpha \log P + \beta \log(B - V)_0 + \gamma \,. \tag{2.27}$$

The physics behind this phenomenological relation is quite well understood nowadays. Cepheid pulsations occur because, at a certain temperature range, the star has a layered structure where heat gets trapped inside, forced by a specific opaque layer. When heat increases, the temperature rises and the layered structure changes, releasing the accumulated energy until the temperature lowers enough to begin the process again. But this periodic mechanism only happens when the Cepheid star meets certain specific conditions [72]. For instance, in the case of colder stars, convection dilutes layers and the pulsation is prevented, whereas for hotter stars the layer which creates the mechanism is too hot in order to accumulate enough heat.

The observation of this phenomenon has various systematics like the mass loss or the helium abundance, or the dependence on metallicity of the PLC relation mentioned above. But the most important and studied systematics is the reddening and extinction due to the interstellar dust, which is somehow alleviated with observations in the near infrared and multiple bands observations.

Once the Cepheid brightness is modeled, a distance calibration is needed in order to adjust its absolute magnitude and extract the distance modulus. Classical procedures to calibrate their PLC relation are parallax distance measurements to galactic Cepheids [94] or the use of the Large Magellanic Cloud as independent distance indicator for the zero-point [160]. Nevertheless there are several other host galaxies that can be used as distance indicators to calibrate extra-galactic Cepheids [188]. With this calibration done, the next rung in the cosmic distance ladder can be taken.

2.2.2 Supernovae Ia

Type Ia supernovae are the most abundant and used standard candles nowadays, the probes which led to the discovery of the accelerated expansion of the Universe [178, 186]. Supernovae are gigantic explosions that happen in the last evolutionary stages of massive stars, which are visible as a "new" star for several weeks or months before fading away.

Most supernovae occur because the core of the progenitor star suffers a sudden gravitational collapse, led by several different mechanism. Usually the core stops its collapse quite abruptly when enough neutron degeneracy pressure is achieved, but the sudden release of energy alongside the shock wave created by the rebound ejects the outer layers of the star in the dramatic explosion known as supernova. Though these core-collapse supernovae can be used in cosmology [145], there are better candidates for our goals.

These are Type Ia supernovae, which occur in a totally different way. They are always binary star systems in which at least one of the star is a white dwarf, though several other details are still unknown [162]. When this star accumulates enough material from its binary companion (through accretion or via a merger), its core temperature raises enough to trigger runaway nuclear fusion and so the destruction of the star with the subsequent supernova explosion. This sudden runaway nuclear fusion always occurs at a precise temperature, just before reaching the Chandrasekhar mass limit of around 1.4 solar masses. Thus, as the energy released in the process is always fairly similar due to the uniform mass of the white dwarfs that explode via accretion, this type of supernovae produces a consistent peak luminosity and it can be calibrated as standard candle. Besides, these Type Ia supernova are easily distinguishable by their spectra, which show silicon absorption lines but no hydrogen lines in general, being thus different from the rest of supernovae.

SNe Ia calibration

When first SNe Ia were being calibrated as standard candles, an unaccounted scatter for the Type Ia supernovae absolute magnitudes of around 0.2 magnitude was found [116], which was difficult to explain theoretically. However, an empiric correlation was found between the peak luminosity of SNe Ia and the shape of their light curves, that is, how the observed luminosity flux evolves through time [180]. By measuring the magnitude decay in the B-band after 15 days from its maximum, $\Delta m_{15}(B)$, a linear relation gives the maximum magnitude of each supernovae,

$$M_{max} = a + b\Delta m_{15}(B) \ , \tag{2.28}$$

where a and b are parameters to fit commonly shared by all the SNe Ia. In this way, it is possible to know the luminosity peak of each SNe Ia through its light curve and, thus, to extract the true luminosity distance from the observed apparent magnitude, once a proper distance calibration is performed.

However, this relation has evolved and been improved, taking also into account the color of the supernovae. Therefore, nowadays the formula for distance modulus estimation is based on the empirical observation that the SNe Ia are homogeneous standard candles whose variability can be addressed with two parameters: the first one describing the time stretching of the light curve, and the second one the supernova color at maximum brightness.

Even though light curve fitting or calibration has improved, it always requires some overlapping independent distance observations [128], which makes it possible to build up the cosmic ladder for SNe Ia, where Cepheids and other distance measurements are used in order to fit the light curves of near SNe Ia and, then, extend the calibration to further SNe Ia. For this purpose, the light curve must be measured in a very detailed way taking into account all possible systematic effects. For instance, extinction from dust, both coming from the host and our Milky Way galaxy, is usually avoided using several filters with different wavelength pass bands, as the dust absorbs light differently depending its wavelength. Thus, several filters or pass band systems exist for cosmological observations, though the common and relevant ones for SNe Ia observations are in the optical and near-infrared wavelengths. Another important contribution to take into account is the K-correction [120], which compensates the shift suffered by the supernova spectrum due to the redshift. This correction is particularly important when the observations are done using filters [47], as each filter pass band would measure a slight intensity shift with respect the true one emitted by the SNe Ia. Thus, to properly determine a precise distance, it requires a well-observed SNe Ia light curve in multiple pass bands, to constrain not only the intrinsic luminosity but also the extinction by dust along the line of sight [185].

SNe Ia catalogs

As stated above, supernova catalogs usually give the measurement of the distance modulus to fit cosmological data, which is the case for the main SNe Ia catalog used in this thesis, Union2 [15] and Union2.1 [220]. They give the redshift, distance modulus and the full covariance matrix with the error for each SNe Ia on all the corresponding quantities (magnitude, stretch and color). Union2 has 557 SNe Ia in its catalog and Union2.1 extends to 580 SNe Ia, the latter having a redshift range of $0.015 < z < 1.414$.

Both catalogs use the SALT2 model [112] to fit light curves, which is based on a pseudo-principal component analysis [15]. Once fitted with near well-known SNe Ia, the parameters m_B^{max}, B-band flux at maximum light; x_1, stretch factor of the light curve; and C, SNe Ia color, are given for each observed SNe Ia by the fitted SALT2 model. With these parameters, the distance modulus can be formed for each SNe Ia

$$\mu_B = m_B^{max} + \alpha \cdot x_1 - \beta \cdot C - M_B \ , \tag{2.29}$$

where M_B is the absolute B-band magnitude for a SNe Ia with $x_1 = C = 0$; together with α and β, all three of them are nuisance parameters that are generally fitted simultaneously with the rest of the cosmological parameters. The Union2 and Union2.1 compilations,

though, were released in a version where the distance modulus was given with the parameters α and β fitted after raw-data processing. Therefore, this thesis uses the version where observational data come as the distance modulus with their redshift and their full covariance matrix, although the values for those parameters x_1 and C were also available alongside the full observational data.

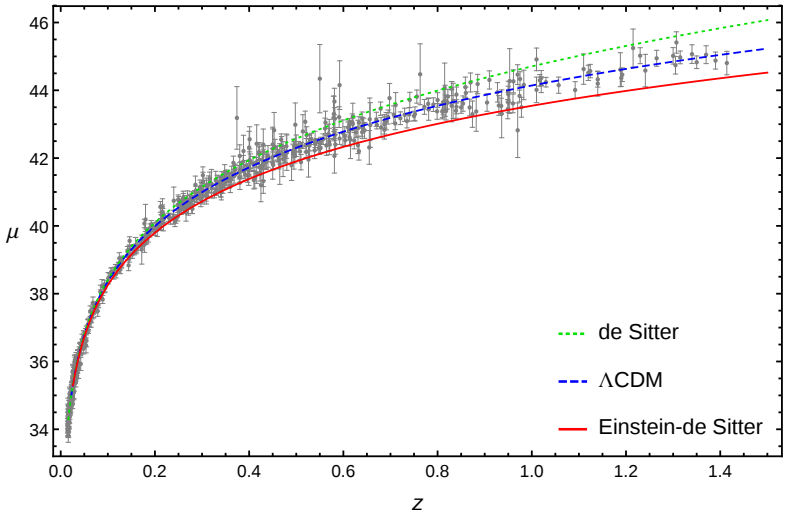

Figure 2.1: *Distance moduli μ and their error bars versus redshift from the Union2.1 catalog [220]. The distance modulus from three different flat models are also displayed, from top down: dotted green for de Sitter Universe $(\Omega_m = 0,\, \Omega_\Lambda = 1)$, dashed blue for ΛCDM $(0.3,\, 0.7)$, and solid red for Einstein-de Sitter Universe $(1,\, 0)$.*

In Fig. 2.1 observational data coming from the Union2.1 catalog [220] are displayed, showing the redshift dependence of the distance modulus μ. The same quantity derived from three different cosmological models is also shown: the agreement with a ΛCDM Universe is clear. A Universe fully filled only with matter and no dark energy at all, as in the Einstein-de Sitter case $(\Omega_m = 1,\, \Omega_\Lambda = 0)$, predicts a smaller distance modulus than measured, meaning that the SNe Ia should be closer than what is actually derived from observations. On the other hand, a Universe empty of matter but full of dark energy only, as in the de Sitter case $(\Omega_m = 0,\, \Omega_\Lambda = 1)$, predicts a bigger distance modulus, and thus the SNe Ia should be much further away than expected.

2.3 Standard Rulers

If instead of the intrinsic luminosity, it is the physical size what is known about an object, then one can measure the distance to that object by observing its apparent size, namely,

using the angular diameter distance. These astronomical objects or structures are called standard rulers.

The most common standard ruler for cosmology is the physical scale set by recombination physics, which left imprints both in the photon background and in the baryon spatial distribution, creating big structures or patterns whose physical size can be theoretically predicted with a quite large precision. The most notorious examples of such imprints are the shift parameters of the cosmic microwave background (CMB) and baryon acoustic oscillations (BAO) observed in the matter distribution at cosmological scales. Today, the smooth and linear fluctuations of the CMB radiation contrast the clustered and non-linear one at small scales observed for matter inhomogeneities. This discrepancy is due to their different evolution, where the matter perturbations has been growing due to the gravitational attraction, while radiation pressure has prevented photon fluctuations to suffer the same fate. However, both phenomena have the same physical origin.

Perturbations at recombination

First, it could be helpful to provide a first qualitative description of the process which seeded both CMB and BAO.

To understand it, we have to move backwards in time and follow the evolution of matter perturbations that have led to the present large scale structure of our Universe. We would see how these inhomogeneities became smoother and smoother in the past moving from non-linear matter inhomogeneities to the linear regime. At some time, matter perturbations (from BAO) would match photon fluctuations (from CMB). This moment is called *recombination*, a misleading term if we follow the evolution of the Universe from the beginning to now because, actually, it is the first time when in the Universe baryons and electrons can combine to form neutral hydrogen. Beyond recombination, photons and baryons are tightly coupled in a *photon-baryon plasma*, where both cosmic ingredients are mixed and share the same fluctuations. Photons interact strongly with free electrons through Thompson scattering; electrons interact with baryons through electromagnetic interaction; neutrinos are already decoupled, because the weak interaction decouples earlier than the electromagnetic one; and, finally, dark matter interacts only gravitationally with all the other components.

The key point is to understand where these fluctuations come from. In the inflationary scenario [28], we have quantum fluctuations of the inflaton, the scalar field which should drive the exponential expansion of the Universe at that epoch, corresponding to energy fluctuations, namely mass density fluctuations which, consequently, influence the space-time by curvature fluctuations. As inflation goes on, such fluctuations are stretched to cosmological scales and are led out of the Hubble horizon, i.e., out of the causal connection with each other (they are said to be "frozen"). As soon as inflation ends, fluctuations start to re-enter the horizon, getting in causal contact and evolving: perturbations in the curvature induce perturbations in the density of the plasma, corresponding to gravitational potential wells and hills with respect to the homogeneous background level. Whenever a

density perturbation appears, gravity tries to make this fluctuation grow by compressing the plasma; but the compression itself raises radiation pressure which eventually stops the compression and starts to dilute matter; dilution implies cooling, thus a lower radiation pressure, until gravity overcomes it again, and a new phase of compression begins. This back and forth play between gravity and pressure creates compressions and rarefactions in the plasma that propagate through it as sound waves with a specific sound speed.

These density perturbations can be translated into temperature fluctuations, with compression corresponding to higher temperatures and dilution to colder ones; it is thus easier and natural to quantify and describe the physics of the plasma at this epoch by a temperature fluctuation field $\Theta \equiv \Delta T/T$ which is, actually, what we effectively measure nowadays. If we want to approach this qualitative discussion now from a mathematical point of view, we can start by considering a simplified and idealized case of a perfect photon-baryon fluid where both gravity and the role of baryons are neglected. Combining the continuity and Euler equations of this fluid shows that the temperature fluctuations follow the basic oscillator equation in Fourier space [122],

$$\ddot{\Theta}(k) + c_s^2\, k^2\, \Theta(k) = 0 \,, \tag{2.30}$$

where the sound speed c_s can be taken at a first approximation $c_s = \sqrt{\dot{p}/\dot{\rho}} \cong 1/\sqrt{3}$, assuming radiation domination. Therefore, one can easily see how the solution to such equation would be simply $\Theta(t) = \Theta(0)\cos(k\, r_s)$, i.e. the temperature field follows the acoustic oscillations of the photon-baryon plasma, as its compressions and rarefactions heat and cool the fluid. We can also better understand what happens at recombination: as soon as the first atoms are formed, photons and baryons are decoupled, and oscillations are turned off. But the temperature at which they were is now imprinted in both photons and baryons. In particular, photons are now free to move in the Universe, and we collect them now as redshifted to the microwave band: the detected anisotropies of CMB are, thus, images of inhomogeneities at the time previous to recombination.

It is also clear how the oscillation pattern sets a characteristic fundamental length related to the extrema of the oscillations; such length is generally called as sound horizon, r_s, and it corresponds to the length travelled by the plasma from the beginning to the recombination epoch (we will defined it properly in next sections). It corresponds to photons which are in their maxima or minima at time of recombination; other modes or overtones are also present in the detected signal.

Actually, Eq. (2.30), while containing all the basic and general elements for our analysis, misses the most important and crucial ingredient: gravity. In fact, the density perturbations which are supposed to originate the sound waves in the plasma can originate if there are local gravitational potentials, so that higher density regions correspond to deeper potential wells, and lower density to potential hills. The main consequence of introducing gravity in Eq. (2.30) is to increase the extrema of the oscillation. Mathematically speaking, we first

need to perturb the FLRW metric, introducing the potentials Ψ and Φ,

$$\mathrm{d}s^2 = -\left[1+2\frac{\Phi(r,t)}{c^2}\right]c^2dt^2 + a^2(t)\left[1-2\frac{\Psi(r,t)}{c^2}\right]\delta_{ij}\mathrm{d}x^i\mathrm{d}x^j \ , \tag{2.31}$$

where Φ and Ψ are the Newtonian/gravitational potential (entering the Poisson equations) and the metric potential. Then one can check that in this case the oscillator equation would be changed in

$$\ddot{\Theta} + c_s^2\, k^2\, \Theta = -\frac{k^2}{3}\Psi - \ddot{\Phi} \ . \tag{2.32}$$

We are still in a photon-dominated regime, with $c_s^2 = 1/3$. Solution to the previous equation is just an offset of the previous one, i.e. we measure an effective temperature $(\Theta+\Psi)\,(t) = (\Theta+\Psi)\,(0)\cos(k\, r_s)$.

We need now to introduce baryons and their extra-mass contribution. Their contribution can be formalized with the baryon-to-photon ratio parameter, $R_b = (\rho_b + p_b)/(\rho_\gamma + p_\gamma)$; finally, the oscillations follow the equation

$$\left[(1+R_b)\dot{\Theta}\right]^{\cdot} + \frac{1}{3}k^2\,\Theta(k) = -\frac{1}{3}k^2(1+R_b)\Psi - \left[(1+R_b)\dot{\Phi}\right]^{\cdot} \ . \tag{2.33}$$

We now have a different sound speed, lowered to $c_s = 1/\sqrt{3(1+R_b)}$. Assuming $\dot{R}_b/R_b << kc_s$, we now have the solution

$$(\Theta + (1+R_b)\Psi)\,(t) = (\Theta + (1+R_b)\Psi)\,(0)\cos(k\, r_s)\,. \tag{2.34}$$

Thus, baryons not only change the overall amplitude of temperature oscillations, but also have a different effect on extrema: minima are relatively suppressed, and maxima are enhanced. We avoid here the description of many other effects [49, 81], we just recall them: the blueshifting and redshifting of photons as long as they climb in and out the potential wells; both effects are not balanced, because we have to consider the potential wells are stretched (decays) as long as the Universe expands; the Sachs-Wolfe effect on large scales [197]; the damping of the oscillations [210], due to viscosity of the plasma [124]; and others effects which have to be taken into account at the moment of analyzing the observed signal [149, 217–219].

This signal is observed in the closed sphere of the sky as anisotropies in the temperature fluctuations of the CMB, and once a multipole expansion is done, it gives its angular power spectrum. For each multipole ℓ, this power spectrum is characterized by C_ℓ, which is the Fourier transform of the temperature fluctuation variance for that multipole, that is, the variance of $\Theta_\ell(k)$ once integrated over all Fourier modes k. The main contribution to the variance at certain multipole ℓ is given by the Fourier mode k of the corresponding scale. The temperature power spectrum of the CMB redshifts with the expansion of the Universe until today's measured black body radiation with temperature $T_{CMB} = 2.725\,\mathrm{K}$ [95]. From this well measured power spectrum, geometric data can be extracted as shift parameters.

2.3.1 CMB shift parameters

The redshift to the *last-scattering surface*, that is, the last surface from which photons have scattered during recombination, is given by atomic physics rather than cosmology. Once some quantities regarding the ionization history of the Universe are set (mainly neutrino and helium fractions), and the CMB temperature today is measured, a fitting formula can be derived for the last-scattering surface redshift, which only depends on the two cosmological parameters $\Omega_b h^2$ and $\Omega_m h^2$ [123]:

$$z_* = 1048\left[1 + 0.00124(\Omega_b h^2)^{-0.738}\right]\left[1 + g_1(\Omega_m h^2)^{g_2}\right], \tag{2.35}$$

where

$$g_1 = \frac{0.0783(\Omega_b h^2)^{-0.238}}{1 + 39.5(\Omega_b h^2)^{0.763}} \tag{2.36}$$

$$g_2 = \frac{0.560}{1 + 21.1(\Omega_b h^2)^{1.81}}. \tag{2.37}$$

With the redshift of the photon decoupling epoch at recombination, we can now evaluate different functions at the time this process occurs. One of the most important quantity is the sound speed

$$c_s \equiv \sqrt{\frac{\dot{p}}{\dot{\rho}}} = 1/\sqrt{3(1 + \bar{R}_b a)}\,, \tag{2.38}$$

where now the effects of baryons are taken into account with the baryon-to-photon ratio $R_b = \bar{R}_b a = 3\rho_b/(4\rho_\gamma)$ and $\bar{R}_b = 31500\Omega_b h^2 (T_{CMB}/2.7K)^{-4}$ [238], given that $T_{CMB} = 2.725\,\mathrm{K}$ [95]. The distance that light can travel, slowed down through the plasma, by the time of recombination is the comoving sound horizon

$$\begin{aligned} r_s(z_*) &= D_H \int_{z_*}^{\infty} dz' \frac{c_s}{E(z')} = D_H \int_0^{a_*} \frac{da'}{a'^2} \frac{c_s}{E(a')} \\ &= \frac{c}{H_0} \int_0^{a_*} \frac{da'}{\sqrt{3(1 + \bar{R}_b a') a'^4 E^2(a')}}, \end{aligned} \tag{2.39}$$

which characterizes the scale of the CMB physics and is well known and measured to be $r_s(z_*) = 144.43$ Mpc (*Planck* collaboration, [6]) being very likely model independent. It can be seen in the temperature power spectrum that the modes corresponding to acoustic peaks, that is, modes that are caught at their maxima or minima at recombination, are the ones that have an harmonic relationship with this length scale, $k_n = n\pi/r_s(z_*)$.

The mode which follows this relation has a spatial inhomogeneity in the CBM temperature of wavelength λ_n, that appears in the sky with an angular scale of $\theta \approx \lambda_n/D_M(z_*)$,

being $D_M(z_*)$ the transverse comoving distance[1]. If we decompose it in harmonic space, $\ell = 2\pi/\theta$, the relation gives us the multipoles at which the peaks are, $\ell_n = nl_a$, where

$$l_a \equiv \pi \frac{D_M(z_*)}{r_s(z_*)} \tag{2.40}$$

is the angular scale of the sound horizon at recombination.

At first approximation, the angular scale of the sound horizon at recombination l_a gives us also the position of the first peak of the temperature power spectrum. This leads to strong constrains for the geometry of the Universe; because if the scale of the sound horizon is well known, the observed angle in the sky must be given solely by the comoving distance at known last-scattering redshift z_*. Any curvature of the space-time would change this distance, making the observed angle bigger for closed Universe and smaller for the open case, and shifting the position of the peak accordingly.

However, the position of the first peak is shifted with respect to l_a, because there is another variable to take into account, the baryon fraction, parameterized by the dimensionless baryon density Ω_b. Baryons shift the frequency of all modes of the acoustic oscillations compared to the case with only photons, increasing their frequency, and hence their multipoles, as the baryon density grows. This can be easily seen in the sound speed c_s of the plasma in Eq. (2.38), and in the way it depends on the baryon-to-photon ratio $\bar{R}_b$. But, as we have said above, baryons have other main effects in the acoustic oscillations, the extra gravity provided by their mass enhances compression into potential wells, leaving unmodified the maximum rarefactions. Therefore, baryons increase the amplitude of the compression peaks (odds ones) compared to the rarefaction peaks (even ones), and as a result, the ratio between the first and second peak amplitude is given by Ω_b.

And yet, another effect can be appreciated in the CMB temperature power spectrum from where geometric data can be extracted. Non-relativistic matter, characterized with the matter density Ω_m, creates a similar effect to the one from baryons. But these effects appear only during the matter-dominated era, not before, during the radiation-dominated era. The presence of non-relativistic matter can be inferred because it changes the height of the lower multipole peaks compared to the higher multipoles, and it also shifts slightly the position of the peaks.

Thus, if the first three peaks of the CBM temperature power spectrum can be measured with good precision, the geometry of the Universe, the baryon density, and the total non-relativistic matter density can be constrained, though they are all correlated. So the idea behind the definition of the CBM shift parameters is to condense all this information in a few quantities, with as little correlation between them as possible. With this in mind, the scaled distance to the photon-decoupling surface can be defined as

$$R \equiv \sqrt{\Omega_m H_0^2} \frac{D_M(z_*)}{c} \,, \tag{2.41}$$

[1]It would be the angular diameter distance D_A if λ_n was a physical length rather than a comoving one.

and along with l_a and $\Omega_b h^2$, the three of them create a set of parameters that is very powerful so as to summarize and characterize the power spectrum of the CMB [237] at the background level, i.e. as long as we are not interested in analyzing cosmological perturbations. For example, if R is fixed, any variation of l_a creates a very different power spectrum, as l_a sets the structure of the acoustic peaks. In the opposite case, even if l_a is fixed different R changes the height of the peaks. Besides, as R and $r_s(z_*)$ have different dependencies on Ω_m, the measurement of R and l_a strongly constraints Ω_m.

For these reasons, the parameter set $(l_a, R, \Omega_b h^2)$ uniquely characterizes the power spectrum with as little correlation between them as possible [237]. The values for these quantities are obtained by extracting their probability distribution function through Markov chain Monte Carlo (MCMC) fitting of the power spectrum (more details regarding parameter estimation will be given in the next Chap. 3). When *Planck* 2013 temperature + lensing [3] and WMAP7 [139] and WMAP9 [31] polarization data are used, the mean values and standard deviations for the triplet shift parameters are [238]

$$\begin{aligned} \langle l_a \rangle &= 301.57 \quad ; \quad \sigma_{l_a} = 0.18, \\ \langle R \rangle &= 1.7407 \quad ; \quad \sigma_R = 0.0094, \\ \langle \Omega_b h^2 \rangle &= 0.02228 \quad ; \quad \sigma_{\Omega_b h^2} = 0.00030 \ , \end{aligned} \tag{2.42}$$

with the corresponding normalized covariance matrix, that is, the correlation matrix, as

$$\mathbf{C}_{CMB}^{norm} = \begin{pmatrix} 1.0000 & 0.5250 & -0.4235 \\ 0.5250 & 1.0000 & -0.6925 \\ -0.4235 & -0.6925 & 1.0000 \end{pmatrix} . \tag{2.43}$$

In order to obtain the full covariance matrix $\mathbf{C}_{CMB}$, we need the transformation: $(C_{CMB})_{ij} = (C_{CMB}^{norm})\sigma_i\sigma_j$, where σ_i are the 1σ errors of the measured best fit values given in Eq. (2.42).

2.3.2 Baryonic Acoustic Oscillation

Baryonic acoustic oscillations (BAO) [27] are the baryonic counterpart for the anisotropies of CMB radiation. The BAO characteristic length (standard ruler) was set at the moment when acoustic oscillations in the photon-baryon plasma froze, that is, at recombination, when baryons were not affected by photons any more. The sound horizon was imprinted in the matter perturbations and is now hidden in the correlation function between galaxies as a preferable clustering distance, or as a characteristic oscillation in the power spectrum in Fourier space.

One could think that baryons stopped noticing photons at the photon-decoupling epoch computed previously, the last-scattering redshift of Eq. (2.35), but they actually have inertia. So, the sound horizon related to baryons is different from the one for photons;

the time when baryons do no longer feel the Compton drag of photons is known as the *drag epoch*. Similarly, as in the photon-decoupling redshift z_* in Eq. (2.35), the redshift of this drag epoch z_d can be given by a fitting formula [88],

$$z_d = \frac{1291(\Omega_m h^2)^{0.251}}{1+0.659(\Omega_m h^2)^{0.828}}\left[1+b_1(\Omega_b h^2)^{b_2}\right] , \tag{2.44}$$

with

$$b_1 = 0.313(\Omega_m h^2)^{-0.419}\left[1+0.607(\Omega_m h^2)^{0.674}\right] \tag{2.45}$$

$$b_2 = 0.238(\Omega_m h^2)^{0.223} . \tag{2.46}$$

This way, if we evaluate the comoving sound horizon of Eq. (2.39) at the drag epoch instead, we get a slight different value for the sound horizon for baryons $r_s(z_d) = 147.09$ Mpc (*Planck* collaboration, [6]) which is, as expected, larger than the sound horizon for photons. Thus, it is such length which is actually frozen in the matter distribution and appears as a density excess in the baryon distribution at cosmological scales, and it can be used as a standard ruler.

More exactly, after the drag epoch, we have an interaction between the dark matter sitting at the center of the original density perturbation, and such baryon excess located at a distance $r_s(z_d)$ from it. Dark matter follows the perturbations only through gravity, influencing slightly the acoustic oscillations and staying mainly apart from them. However, after recombination the baryon excess at the BAO scale is enough to attract gravitationally part of the dark matter, clustering both massive ingredients at the same scale as it can be seen in Fig. 2.3. Therefore, the probability to form a galaxy at this BAO scale is bigger due to its higher density.

The objective of BAO measurements is to extract this scale, whether as oscillations in the matter power spectrum or as the preferred scale in its spatial distribution, so that it can be used as a standard ruler, at different redshifts if possible. But this ruler is hidden in the sky, because the spherical shells with higher density centered around the original point-like perturbations (Fig. 2.3) are randomly superimposed. Besides, the low proportion of baryons compared to dark matter made this density excess at the BAO scale small compared to the central over density. Nevertheless, through statistical analyses using the two-point correlation function $\xi(r)$ it is possible to detect the BAO signal with big catalogs of galaxies [91].

This two-point correlation function $\xi(r)$ (Fig. 2.2), also called the two-point autocorrelation function, describes the probability distribution of two galaxies depending on their separation. In our case, it can quantify the excess clustering of galaxies on a given scale, normalized to a uniform distribution with mean density. Besides, this two-point correlation function is the Fourier transform of the density fluctuations power spectrum, which can be taken as the matter power spectrum. Thus, a characteristic scale in the two-point correlation function appears in the power spectrum as an oscillation of the corresponding scale, the baryon acoustic oscillations.

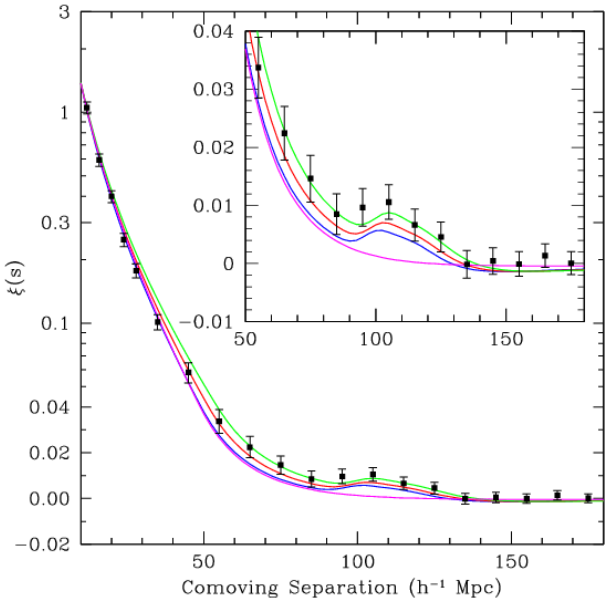

Figure 2.2: *One of the first detection of the BAO scale as a peak in the redshift-space two-point correlation function. The signal was evidenced in the clustering of the SDSS LRG galaxy sample, sensitive to the matter density ($\Omega_m h^2 = 0.12$ (top peak, green), 0.13 (middle peak, red) and 0.14 (bottom peak, blue), all with $\Omega_b h^2 = 0.024$). The bottom magenta line without peak is the correlation function in the pure CDM model, with $\Omega_b = 0$. Figure taken from Eisenstein* et al. *[91]*

However, the computation of the correlation function to get the BAO scale is a challenging work that requires overcoming several difficulties (for further details, see reviews [27, 241]). For instance, the galaxies used to compute the correlation function account only for the small baryonic part of the matter power spectrum, leaving the main contribution of dark matter without direct measurement. For this reason, the object chosen as tracer of the underlying matter power spectrum is important, Luminous Red Galaxies (LRG) being the most common ones mostly for low redshift and Blue galaxies for higher redshift, though there are more possibilities [27].

The fact that during cosmic evolution matter continues clustering reaching the non-linear regime at small scales does not help either. These non-linearities slightly modify the linearly predicted BAO signal [73], though there are reconstruction techniques to ameliorate the BAO signal reversing those effects at some degree [89].

The peculiar velocity of galaxies also modify their observed redshift through Doppler shift, introducing redshift-space distortions (RSD) and increasing uncertainties in the line-of-sight direction. The most common effects are the apparent stretching of galaxies in

virialised clusters along the line-of-sight due to their random velocity (finger of god), and the flattening effect of galaxies in coherent gravitational collapse (Kaiser effect) [129].

These non-linearities and redshift space distortions, coupled to the use of baryonic tracers, make the observed power spectrum biased from the real one [209]. Besides, the fiducial model chosen to infer the real-space distances and other BAO properties can also modify the result of the observation, though in general this influences at a lesser level if models fulfilling CMB requirements are considered [224].

Once all the uncertainties and complications above mentioned have been taken into account, the information of the BAO scale can be extracted from the galaxy surveys, usually with the two-point correlation function, but also computing directly the power spectrum [223]. However, due to the different analysis methods and the finite volume of the surveys, both approaches cannot be translated into each other using Fourier transforms directly [62]. Besides, the BAO scale is so large that a great number of galaxies are required to improve statistics and achieve small errors, which requires surveys volumes of order $1h^{-3}Gpc^3$ [241].

This increased difficulty for statistical analysis alongside the previous challenges, requires a proper estimator for computing the two-point correlation function [141]. Moreover, the theoretical correlation function must be expanded in spherical harmonics [113] so that the information of the BAO scale longitudinal to the line of sight and perpendicular to it can be detached. In this way, the observed redshift depth Δz along the line of sight gives the Hubble function when it is compared to the BAO scale r_s,

$$H(z) = \frac{c\Delta z}{r_s} \; ; \tag{2.47}$$

while the angle $\Delta\theta$ subtended in the sky by the BAO scale perpendicular to the line of sight measures its angular diameter distance, and therefore

$$D_A(z) = \frac{r_s}{\Delta\theta(1+z)} \; . \tag{2.48}$$

Without this multipolar expansion of the two-point correlation function, the spherically averaged correlation function is achieved instead, which blends together the information coming from transverse and longitudinal observations. Nevertheless, in these cases it is still possible to extract BAO information, where the baryon acoustic oscillation scale parameter $A(z)$ is best used, a quantity which does not depend on H_0 [91],

$$A(z) \equiv 100 D_V(z)\sqrt{\Omega_m h^2}/cz \; , \tag{2.49}$$

and depends on the volume-averaged distance,

$$D_V(z) = \left[(1+z)^2 D_A(z)^2 \frac{cz}{H(z)}\right]^{1/3} \; , \tag{2.50}$$

a distance which is approximately the radius of the spherical volume filled by the BAO shell. This function of Eq. (2.49) is built as a mixture of the Hubble function $H(z)$ and the angular diameter distance $D_A(z)$, and so the baryon acoustic scale parameter $A(z)$ is a dimensionless quantity.

If one wants to use the proper multipolar expansion of the two-point correlation function in order to extract the information of the BAO scale along and perpendicular to the line of sight, an anisotropic analysis of the survey must be done so that the two-dimensional two-point correlation function is computed [62]. This way, the measurement of the Hubble function $H(z)$ and the angular diameter distance $D_A(z)$ is possible. However, these quantities are quite correlated and are not robust enough with respect to systematics, therefore the following dimensionless quantities are recommended instead [62],

$$\frac{H(z)r_s(z_d)}{c} = \Delta z \,, \quad \frac{D_A(z)}{r_s(z_d)} = \frac{1}{\Delta\theta(1+z)} \,. \tag{2.51}$$

These new quantities, which are constructed by normalizing the Hubble function $H(z)$ and the angular diameter distance $D_A(z)$ with the comoving sound horizon $r_s(z_d)$, effectively measure the redshift depth and observed angle of the BAO feature, respectively.

Hitherto, we have used the comoving sound horizon r_s as a standard ruler because its size could be given by CMB measurements. If this were unknown, we could still extract information through the fact that we are observing a spherical structure. In this way, the Alcock-Paczynski test can be used [10], which gives the product $D_A(z)H(z)$ from measuring $\Delta z/\Delta\theta$, and its distortion parameter has the following form

$$F(z) \equiv (1+z)D_A(z)H(z)/c \,. \tag{2.52}$$

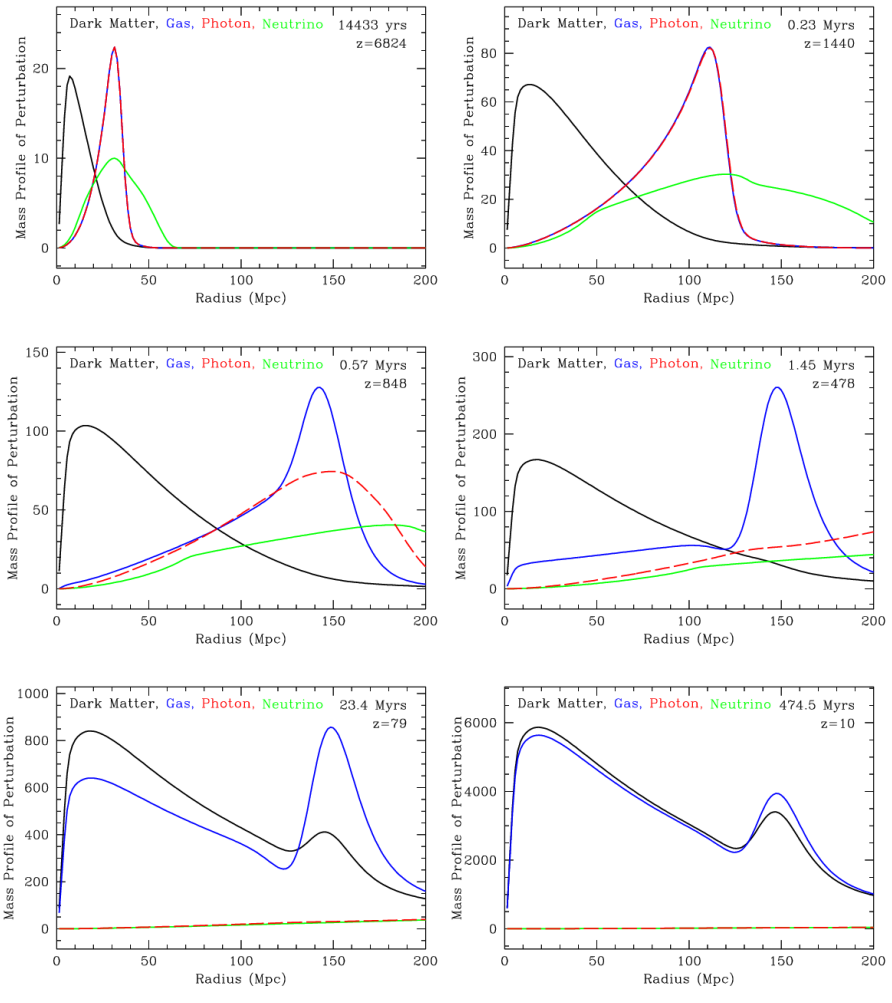

Figure 2.3: *Evolution of radial mass profile of several species as a function of the comoving radius for an initial point-like over-density perturbations at the origin, from the early time before decoupling ($z = 6824$, top left panel) to long after it ($z = 10$, bottom right). We see how the baryon (blue) and photon (red) perturbations share the same profile as they propagate coupled (top right), until recombination when photons leak away from baryons (middle left). After recombination, the baryon perturbation does not propagate any more creating an over-density shell (middle right), while dark matter perturbation (black) has not propagate during all the process. Through gravitational instability, both dark matter and baryons are attracted to the origin and shell over-densities (bottom left), until both species have a similar mass profile (bottom right). Figure taken from Eisenstein* et al. *[90]*

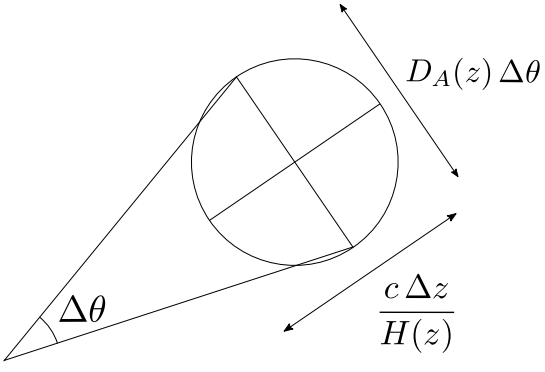

Figure 2.4: *Graphical explanation of the BAO observations regarding the longitudinal and transverse modes with respect the line of sight.*

3 Statistical Inference

In the previous chapters we have introduced some of the main cosmological observables which are used nowadays to probe and constrain the properties of the cosmological background. In this chapter we will describe some relevant statistical tools required in order to set up the reliability of any given theoretical model to describe the available observations in the most satisfactory way.

Specifically, the main goal of any kind of statistical analysis of a given set of data, $\mathbf{d}$, is to obtain the "best" values which help a given model to describe the given measurements and, most important, the corresponding uncertainties on each theoretical parameter set $\boldsymbol{\theta}$. Therefore, we introduce and aim to reconstruct the joint distribution $P(\boldsymbol{\theta}, \mathbf{d})$, defined as the probability distribution function (pdf) of having the parameters $\boldsymbol{\theta}$ given the data $\mathbf{d}$, when both the data and the parameters are considered as random fields. From such pdf the main statistical properties (mean, median, standard deviation of the parameters) can be eventually extracted.

This specific task can be tackled within two approaches sharing subtle differences in their implementation and philosophy: the frequentist and the Bayesian approach.

The frequentist approach considers the data as a random field generated by an underlying unknown model characterized by some fixed, well defined and equally unknown parameter values. It relies on the possibility that the same experiment can be repeated as many times as required in order to properly recover the pdf of the data given the model. This pdf is precisely the conditional probability of having the data $\mathbf{d}$ given the parameters $\boldsymbol{\theta}$, namely, $P(\mathbf{d}|\boldsymbol{\theta})$. Within the frequentist approach, statistical inference is not a hard task, as long as one can repeat the experiment many times collecting more and more data to improve the constraints of the parameters.

In cosmology, however, we have just a single realization of one humongous experiment, our Universe. Thus, strictly speaking, we cannot consider the observational data as a random field as in the frequentist approach; its direct application to the cosmological case would end up with a very poor statistical inference for the parameters involved. Nevertheless, we have another statistical approach to tackle this problem which is better suited for the purposes and properties of cosmology, the Bayesian inference. For a useful

and detailed reading about Bayesian inference, see [159, 174].

3.1 Bayesian Inference

In the Bayesian approach, we seek the probability distribution of the parameters, which are considered as random fields, given the available "fixed" data. Thus, in this case, the main goal is to derive the so-called posterior probability $P(\boldsymbol{\theta}|\mathbf{d})$, or equivalently the conditional probability of the parameters $\boldsymbol{\theta}$ given the data $\mathbf{d}$ which we can observe and measure. From this posterior probability of the parameters any kind of statistical information about them can be eventually derived. Examples of Bayesian inference applied to cosmology can be found in [61, 148, 207, 225, 226].

This posterior probability $P(\boldsymbol{\theta}|\mathbf{d})$ can be related to the above mentioned joint distribution $P(\boldsymbol{\theta}, \mathbf{d})$, if the probability of having the data $\mathbf{d}$, $P(\mathbf{d})$, is known. A similar expression is also possible in the frequentist approach, for the conditional probability $P(\mathbf{d}|\boldsymbol{\theta})$, if the probability $P(\boldsymbol{\theta})$ to have a certain set of parameters $\boldsymbol{\theta}$ is also known. Indeed, all these probabilities are related to each other by the following expression [174, 225],

$$P(\boldsymbol{\theta}|\mathbf{d})P(\mathbf{d}) = P(\boldsymbol{\theta}, \mathbf{d}) = P(\mathbf{d}|\boldsymbol{\theta})P(\boldsymbol{\theta}) \,, \tag{3.1}$$

the well-known Bayes' theorem.

3.1.1 Bayes' Theorem

The Bayes' theorem describes the conditional probability of an event based on the probability of another one, and it is usually used to invert such conditional relation. The most common expression for the Bayes theorem can be derived from Eq. (3.1) as [46, 71]

$$P(\boldsymbol{\theta}|\mathbf{d}) = \frac{P(\mathbf{d}|\boldsymbol{\theta})P(\boldsymbol{\theta})}{P(\mathbf{d})} \,. \tag{3.2}$$

It allows us to compute the posterior probability $P(\boldsymbol{\theta}|\mathbf{d})$, through the conditional probability of having certain data $\mathbf{d}$ given the parameters $\boldsymbol{\theta}$, $P(\mathbf{d}|\boldsymbol{\theta})$. Given that this latter probability can be interpreted as how likely it is to have the observed data as a function of the parameter values, it is commonly known as the *likelihood function* and indicated as $L(\mathbf{d}|\boldsymbol{\theta})$. On the other hand, the probability $P(\boldsymbol{\theta})$ to have a certain set of parameters $\boldsymbol{\theta}$ is also known as the *prior distribution* $\Pi(\boldsymbol{\theta})$, while the probability of having the data $P(\mathbf{d})$ is generally called *evidence*, $E(\mathbf{d})$. Rewriting Eq. (3.2) in terms of the Bayesian inference quantities [159], we thus have

$$P(\boldsymbol{\theta}|\mathbf{d}) = \frac{L(\mathbf{d}|\boldsymbol{\theta})\Pi(\boldsymbol{\theta})}{E(\mathbf{d})} \,. \tag{3.3}$$

Prior

The prior distribution $\Pi(\boldsymbol{\theta})$ contains all the possible previous knowledge about the parameters which we can infer/collect before performing the measurements. This information can include any sort of physically well-motivated property of the model proposed; generally, this is realized by defining a validity range for the parameters of the model, given by insights into the experimental setup and its performance, or regarding estimations from previous experiments.

However, it is quite common to choose priors that influence the least possible the Bayesian inference. For that purpose, flat priors are taken, where the probability for a given parameter is one within a certain range of values, and zero outside of it. This *uninformative prior* can be easily achieved, for example, using Heaviside functions or simply defining limits on the range of values that each parameter can take, in which case it is also usually known as *top hat prior* [207]. Nevertheless, due to the role and definition of the priors and the consequent possibility to induce a possible bias, the Bayesian approach is sometimes considered subjective [174]. However, this possible bias can be minimized or alleviated (even if not eliminated in its entirety) by choosing a range for the parameters which is large enough to cover all the possible reasonable values that this parameter can achieve, so that a possible extension of the prior function does not produce statistically significant changes in the parameters' pdf.

Evidence

For a proper definition of probability distributions, both sides of Eq. (3.3) must be normalized to unity. For the right hand side, this is done by the factor in the denominator, the evidence $E(\mathbf{d})$. From Eq. (3.3) and the definitions of the quantities in it, we can easily see that if we marginalize the likelihood over the full parameter set $\boldsymbol{\theta}$, the Evidence can be equivalently seen as the weighted average likelihood of a given model [29], with the prior function acting as weighting function:

$$E(\mathbf{d}) = \int L(\mathbf{d}|\boldsymbol{\theta})\Pi(\boldsymbol{\theta})d\boldsymbol{\theta} \ . \tag{3.4}$$

From this definition, it is clear that the Evidence somehow measures the support of the data to a given model once every possible values for the parameters $\boldsymbol{\theta}$ have been considered. As the Evidence is in principle independent of the parameters $\boldsymbol{\theta}$, when performing a fitting procedure (as we will show in next sections) it only appears as a normalization factor of the posterior probability, and thus usually is left aside because its contribution is just in the form of a scaling factor which does not alter the statistical outputs. But as we will show in Sec. 3.3, the evidence is very useful for model comparison, though its computation might be (analytically) difficult or even not manageable in most of the cases, or (numerically) hardware and time consuming [153, 172].

3.1.2 Likelihood

The likelihood $L(\mathbf{d}|\boldsymbol{\theta})$ is the conditional probability of having certain data $\mathbf{d}$ given the parameters of a model $\boldsymbol{\theta}$ [174]. If the measurements d_i are independent, it can be written as

$$L(\mathbf{d}|\boldsymbol{\theta}) = \prod_i P(d_i|\boldsymbol{\theta}) \ . \tag{3.5}$$

In the frequentist approach the likelihood is a function of the data $\mathbf{d}$, which is considered as a random field. However, in the case of Bayesian inference, once the observations have been done and the data are known and fixed, the likelihood can be considered as a function of the unknown parameters $\boldsymbol{\theta}$ for a given fixed value of $\mathbf{d}$. Therefore, usually the likelihood function is expressed as function of the model parameters only, $L(\mathbf{d}|\boldsymbol{\theta}) \equiv L(\boldsymbol{\theta})$, in Bayesian statistics.

When the measurements are considered to have a normal distribution around their (unknown) true values (a proper consideration with enough data points due to the central limit theorem), the likelihood takes the following exponential form [133, 226],

$$L(\mathbf{d}|\boldsymbol{\theta}) \propto e^{-\frac{1}{2}\chi^2(\boldsymbol{\theta})} \ , \tag{3.6}$$

where the proportionality factor we miss to introduce is exactly the Evidence, whose value is unimportant in this case. Instead, $\chi^2(\boldsymbol{\theta})$ is the chi-squared function, or simply chi-square, needed to evaluate the goodness of a fit through some tests of some parameters $\boldsymbol{\theta}$ with respect to the data $\mathbf{d}$. If the data set is made of independent data points, then the χ^2 reduces to the simple expression of

$$\chi^2(\boldsymbol{\theta}) \equiv \sum_i \left(\frac{d_i^{obs} - d_i(\boldsymbol{\theta})}{\sigma_i^{obs}} \right)^2 \ , \tag{3.7}$$

where $d_i(\boldsymbol{\theta})$ are the data values generated by the model given the parameters $\boldsymbol{\theta}$, and d_i^{obs} are the observed data points with the Gaussian dispersion σ_i^{obs} given by the observational error. In general, however, the different data points d_i^{obs} are correlated among each other through a covariance matrix C_{ij} given by the experiment or observations. In this case, the χ^2 has the following matrix form,

$$\chi^2(\boldsymbol{\theta}) \equiv \left[\mathbf{d}^{obs} - \mathbf{d}(\boldsymbol{\theta})\right]^T \mathbf{C}^{-1} \left[\mathbf{d}^{obs} - \mathbf{d}(\boldsymbol{\theta})\right] \ , \tag{3.8}$$

where the above uncorrelated case is recovered when the covariance matrix is diagonal, taking $C_{ij} = \delta_{ij}\sigma_i^2$.

Once the likelihood function has been constructed, we can now search for the true parameter values of the model that supposedly have created the data observed. For that purpose, the maximum likelihood principle affirms [133] that the value $\boldsymbol{\theta}^*$ can be taken as a proper estimator for the true values of the parameters $\boldsymbol{\theta}$ when the likelihood is

maximized with respect to the parameters,

$$L(\mathbf{d}|\boldsymbol{\theta}^*) \geq L(\mathbf{d}|\boldsymbol{\theta}) \ , \quad \forall \boldsymbol{\theta} \ . \tag{3.9}$$

However, instead of maximizing the likelihood, from Eq. (3.6) the most common approach is to minimize the $\chi^2(\boldsymbol{\theta})$, which is fully equivalent regarding the maximum likelihood principle.

3.1.3 Marginalization of parameters

There can be situations where some of the parameters are not of direct interest in the analysis, either because of being nuisance parameters of the observations rather than of the model, or because the observations cannot properly measure them. In both cases, the unwanted parameters can be omitted with the proper proceeding in order to ease the computations or simplify the analysis. Such procedure is calling *marginalization*.

Marginalization is done when the unwanted parameters are integrated out of the probability distribution. If we divide the parameters $\boldsymbol{\theta} = (\boldsymbol{\theta_d}, \boldsymbol{\theta_u})$ in the desired $\boldsymbol{\theta_d}$ and unwanted $\boldsymbol{\theta_u}$ set of parameters, we can integrate the corresponding pdf on the last ones in order to get a pdf with no dependence on them [232],

$$P(\boldsymbol{\theta_d}) = \int P(\boldsymbol{\theta_d}, \boldsymbol{\theta_u}) d\boldsymbol{\theta_u} \ . \tag{3.10}$$

The integration is performed over the entire range of the parameters $\boldsymbol{\theta_u}$. In the Bayesian context, where conditional probabilities are used, the above marginalization is done in a similar way. In the case of the likelihood, for example, we have

$$L(\mathbf{d}|\boldsymbol{\theta_d}) = \int L(\mathbf{d}|\boldsymbol{\theta_d}, \boldsymbol{\theta_u}) \Pi(\boldsymbol{\theta_u}) d\boldsymbol{\theta_u} \ , \tag{3.11}$$

where the integration range is the same of the prior $\Pi(\boldsymbol{\theta_u})$, when it is properly defined.

The marginalization can be done both numerically, once the posterior is obtained, or analytically before any computation to obtain the posterior is done.

Instead of the marginalization, maximization is another option. It consists on fixing the unwanted parameters at the values which yield maximum likelihood, $\boldsymbol{\theta_u^*}$, and restrict the likelihood function to the parameter-subspace of the desired parameters. This maximization procedure, though, generally overestimates the likelihood creating tighter contours in parameter-space than with respect to the case where marginalization is performed on the likelihood function [84, 226].

We show now one simple but specific example for the analytical marginalization of the likelihood, which will enter many of the analysis we will use in the next sections, and which can be employed only when constant additive parameters appear in the data $\mathbf{d}$ [68]. Let us consider N data points d_i^{obs} that are modeled by $d_i(\boldsymbol{\theta}, \mathcal{C})$, where $\mathcal{C}$ is a

nuisance parameter different from the parameter set of the model $\boldsymbol{\theta}$. As long as the nuisance parameter $\mathcal{C}$ is an additive constant, namely, we can write $d_i(\boldsymbol{\theta}, \mathcal{C}) = \mathcal{C} + \tilde{d}_i(\boldsymbol{\theta})$, the following analytical marginalization can be performed starting from the usual χ^2 definition,

$$\chi^2(\boldsymbol{\theta}, \mathcal{C}) = \boldsymbol{X}(\boldsymbol{\theta}, \mathcal{C})^T \cdot \boldsymbol{C}^{-1} \cdot \boldsymbol{X}(\boldsymbol{\theta}, \mathcal{C}). \tag{3.12}$$

where $\boldsymbol{X}(\boldsymbol{\theta}, \mathcal{C}) = \boldsymbol{d}^{obs} - \boldsymbol{d}(\boldsymbol{\theta}, \mathcal{C})$. This expression of the χ^2 depends on the nuisance parameter $\mathcal{C}$, and so the likelihood does. The marginalization is done through the integration of the likelihood and taking into account the prior distribution $\Pi(\mathcal{C})$ of the nuisance parameter,

$$\chi^2_{marg}(\boldsymbol{\theta}) = -2 \ln \left[\int_{-\infty}^{\infty} \exp\left(-\frac{1}{2} \chi^2(\boldsymbol{\theta}, \mathcal{C}) \right) \Pi(\mathcal{C}) d\mathcal{C} \right] . \tag{3.13}$$

Assuming an uninformative uniform flat prior to simplify the integration and computing its analytical solution, one obtains the marginalized χ^2 [68, 108]

$$\chi^2_{marg}(\boldsymbol{\theta}) = a + \ln \frac{d}{2\pi} - \frac{b^2}{d} , \tag{3.14}$$

where $a \equiv \mathbf{X}(\boldsymbol{\theta})^T \cdot \mathbf{C}^{-1} \cdot \mathbf{X}(\boldsymbol{\theta})$, $b \equiv \mathbf{X}(\boldsymbol{\theta})^T \cdot \mathbf{C}^{-1} \cdot \mathbb{1}$, and $d \equiv \mathbb{1}^T \cdot \mathbf{C}^{-1} \cdot \mathbb{1}$ have no dependence on the nuisance parameter $\mathcal{C}$ (equivalent to setting $\mathcal{C} = 0$).

3.1.4 Probability intervals

Once the likelihood is maximized and the most "likely" values of the parameters are known, the attention shifts to inferring their uncertainties. In this case, an approach similar to the frequentist one can be applied, with the confidence intervals or regions defined from the parameter-space around the maximum likelihood point.

Centered around this point, the boundary of the parameter-space region that contains the $100\gamma\%$ of the likelihood is given by the difference between the smaller value of the χ^2, labeled as χ^2_{min}, and the constant $\chi^2(\boldsymbol{\theta}) = \chi^2_{min} + \Delta\chi^2_k(\gamma)$ value, which is given by the quantity $\Delta\chi^2_k(\gamma)$ and defines the confidence contours in the parameter-space [207]. This $\Delta\chi^2_k(\gamma)$ increment depends on the confidence level γ which is required and on the number of parameters, k. It can be computed by the following integration

$$\gamma = \int_0^{\Delta\chi^2_k(\gamma)} P_{\chi^2_k}(x) dx , \tag{3.15}$$

where $P_{\chi^2_k}(x)$ is the χ^2 distribution [226]. The most common values for γ, corresponding to different likelihood content, are shown in Tab. 3.1 for the case of 1 and 2 parameters which can be easily and usually represented graphically.

This procedure, similar to the frequentist approach, is based entirely on the likelihood function, or equivalently on the χ^2. But in the Bayesian approach, we usually have access

Table 3.1: *Values for different likelihood content and their respective standard error and χ^2 increment depending on the number of parameter k.*

Likelihood content	1σ	2σ	3σ
$100\gamma\%$	68.3%	95.4%	99.7%
$\Delta\chi^2_{k=1}(\gamma)$	1.00	4.00	9.00
$\Delta\chi^2_{k=2}(\gamma)$	2.3	6.17	11.80

to the probability distribution functions of the parameters in form of the posterior function, from which the intervals can be computed. The main idea is that the confidence level γ includes a parameter-space volume $100\gamma\%$ of the posterior distribution around the best-fit values of the parameter or maximum likelihood point. Quantiles can be calculated from the distribution in order to have insights on the wanted percentage confidence levels. Therefore, once the posterior is marginalized in order to obtain the probability distribution function of each parameter, we can easily compute their confidence intervals by simply taking their quantiles corresponding to the desired percentage $100\gamma\%$. In order to draw 2D contours, the posterior is marginalized except for the desired 2 parameters, thus obtaining their joint probability distribution function where the contours are given by the $100\gamma\%$ volume filled by it.

3.2 Parameter estimation with MCMC

There are several methods to maximize the likelihood or minimize the χ^2 in order to perform the Bayesian inference. The first very intuitive approach is the minimization of the χ^2 by building a grid in the parameter-space and evaluating the χ^2 in each point of that grid. In this case, the minimum in the χ^2 can be found out by progressive refining of the grid, while the confidence intervals can be approximated by calculating (numerically) how the likelihood varies around the minimum by means of finite difference algorithms [226]. However, this method is limited by the resolution of the chosen grid, and even if there are techniques to improve the performance [207], the number of points in the grid escalates exponentially with the number of parameters.

Nevertheless, there are other approaches called Markov Chain Monte Carlo (MCMC) where the number of points escalates more or less linearly with respect to the number of parameters. Besides, once the MCMC is correctly applied to the data set, it will result in a list of random points directly drawn from the posterior distribution, which can thus be easily reconstructed. For this reasons MCMCs give very suitable tools to perform statistics.

Markov Chain

Every discrete stochastic process describing a sequence of possible states $\{\theta^{(i)}\}$ where its present step $\boldsymbol{\theta}_t$ summarizes all the relevant information to describe with probability its future steps can be defined as a Markov chain [174]. In other words, the probability $p_{t+1}(\theta^{(j)})$ of moving to the state $\theta^{(j)}$ on the next step $t+1$ depends only on the probability distribution of all states $\boldsymbol{\theta}_t \equiv \{p_t(\theta^{(i)})\}$ on the current step t, not on the previous ones. In our case, states $\{\theta^{(i)}\}$ are points in the parameter-space of the model which is being tested, and we seek their statistical data given the available observations.

To define a Markov chain, it is enough to specify the transition probabilities $T_t(\theta^{(i)}, \theta^{(j)})$ for the subsequent states and its initial probability distribution over all states, $\boldsymbol{\theta}_0 \equiv \{p_0(\theta^{(i)})\}$, the first step of the chain. From these initial settings for a Markov chain, the most important feature is usually the transition probability, which can be time independent $T(\theta^{(i)}, \theta^{(j)})$, that is, it is the same at every step t. Markov chains with this property are labeled as time-homogeneous, and this type of chains are mostly used to create MCMC algorithms. In general, any transition probability can be expressed as a matrix $\mathbf{T}_t$; when each step t is written as a row vector $\boldsymbol{\theta}_t$ of the chain, then the next step is computed as

$$\boldsymbol{\theta}_{t+1} = \boldsymbol{\theta}_t \mathbf{T}_t \ . \tag{3.16}$$

In the case of time-homogeneous chains, the transition matrix $\mathbf{T}_t$ is given by the t-th power of the matrix $\mathbf{T}$, so that the above equation simplifies to

$$\boldsymbol{\theta}_t = \boldsymbol{\theta}_0 \mathbf{T}^t \ . \tag{3.17}$$

Once defined the transition probability, Markov chains have invariant (or stationary) final asymptotic distributions $\boldsymbol{\pi}$, which, once reached, do not change any more as the chain keeps evolving [174]. Therefore, once the chain has reached this invariant distribution $\boldsymbol{\pi}$, it keeps there forever. Generally, all Markov chains have at least one invariant distribution, and for finite state-space chains this is guaranteed [174].

Nevertheless, we want our target posterior to be a single invariant distribution from where sampling points can be collected. In order to easily set the invariant condition for this distribution, time-homogeneous Markov chains which fulfill the more restrictive condition of detailed balance are taken, also called time-reversible homogeneous Markov chains [174]. This detailed balance condition means that, within an invariant distribution, transition probability from state $\theta^{(i)}$ to $\theta^{(j)}$ has the same probability that the opposite transition from $\theta^{(j)}$ to $\theta^{(i)}$. Or stated mathematically,

$$\pi(\theta^{(i)})\, T(\theta^{(i)}, \theta^{(j)}) = \pi(\theta^{(j)})\, T(\theta^{(j)}, \theta^{(i)}) \ . \tag{3.18}$$

If this type of chains reaches its invariant distribution $\boldsymbol{\pi}$ regardless of the initial starting one, the chain is also said to be ergodic. Though there are several definitions for ergodicity, we follow the definition given by [174]: a chain is ergodic if the invariant distribution is

eventually reached,

$$\lim_{t\to\infty} p_t(\theta^{(i)}) = \pi(\theta^{(i)}) \,, \tag{3.19}$$

independently from the starting distribution $p_0(\theta^{(i)})$. This single invariant distribution $\boldsymbol{\pi}$ is also called the equilibrium distribution, which can be reached by an ergodic chain in a finite number of steps.

Although there are chains with a step dependent transition probability which have also an invariant distribution, to build a MCMC algorithm we are interested in time-reversible homogeneous Markov chains which are also ergodic. In this way, through the detailed balance, we can be sure that the posterior distribution we seek is indeed an invariant distribution of the Markov chain [226]. And through the ergodicity, this posterior distribution is going to be the equilibrium distribution to which the chain goes each time we perform the Markov chain, regardless of the initial starting distribution.

However, in the most common cases where the chains are performed computationally, it is not easy to say when a finite Markov chain is ergodic, that is, whether it has really reached the equilibrium distribution or not.

Monte Carlo

Monte Carlo methods are a broad class of computational algorithms that rely on repeated random sampling to obtain numerical results [159]. In principle, Monte Carlo methods can be used to solve any problem which can have a probabilistic interpretation or approximation. However, these methods are also used to perform numerical approximate computations of deterministic problems.

A very common use of the Monte Carlo approach is to compute numerical integration of high dimensional functions [173]. As the number of dimensions increases, so does exponentially the computational effort of these integrations, as in the above mentioned grid case. Besides, the integration limits can be very complicated and difficult to implement in high dimensional situations. The similarity with our case is that MCMC methods can be seen as the numerical integration of the posterior distribution function.

3.2.1 General description

After a general summarized explanation of the two main basic ideas on which MCMC methods are based, we describe now the generic features that most of the MCMC techniques share. The idea behind any MCMC algorithm is to design a judicious Markov chain model with a stationary probability distribution corresponding to the joint pdf of the parameters, the posterior, and to use the MCMC sampler to get enough points to reveal it through Monte Carlo approximation.

Proposal density

The first step to build the MCMC sampler is to define the transition probability of the Markov chain, also called proposal density when the space of states of the MCMC (in our case, the parameter space of the theoretical model) is continuous. A good choice for this proposal density is of utmost importance for an efficient MCMC code to run, as it is a local algorithm, that is, a sampler which has a finite reach and does not (or cannot) explore the entire parameter space. This means that it can be trapped inside a local maximum far away from the global maximum likelihood of the posterior, which could be then out of reach.

A simple candidate for the proposal density $Q(\boldsymbol{\theta}_t, \boldsymbol{\theta}_{t+1})$ is a multivariate Gaussian of zero mean with a step size s_i for each parameter θ_i which is kept constant at every step of the chain [226]. If this step size s_i is too large, the chain might have difficulties to find out the maximum likelihood point wandering in the parameter space without finding it or being able to set down in the maximum likelihood region [159]. On the other hand, if the step size s_i is too small, the chain might need a much longer time to find the maximum likelihood value, or being unable to sample the tails of the distribution in a satisfactory way or, in the worse scenario, the sampler might be trapped in a local maximum instead of the global one.

Therefore, the best value for the step size s_i is a trade-off between these two behaviors, which can also happen simultaneously for different parameters. A simple way to optimize this step size is by adopting as proposal density a multivariate Gaussian with step sizes given by the covariance matrix of the parameters which are going to be sampled by the MCMC [226]. In such a way, the sampler is pushed to explore the parameter space following paths which are approximately aligned with the degeneracy directions of the parameters, ensuring a more efficient exploration of the total space. This covariance matrix can be easily obtained from within the running MCMC [225], updating it after some number of steps, or by performing preliminary exploratory MCMCs, which roughly sample the posterior distribution and provide a covariance matrix which works better than any a priori s_i as covariance matrix of the proposal density [148].

Burn-in period

To start the Markov chain, we have to set an initial starting point, which is unlikely to be close to the maximum likelihood point. Therefore, the first steps of the sampler constitute the so called *burn-in period*: initial samples from this stage are discarded, since the chain is not yet sampling from the equilibrium distribution which is asymptotically found around the maximum likelihood point. This period can be easily identified by two different but related ways.

The first and simplest method consists on checking the evolution of the posterior, which is maximized and stabilized around the maximum likelihood point. Once the chain is around this point, it starts to sample the target posterior distribution and its values

fluctuates around its maximum.

The second way to identify the burn-in period is by keeping track of the position of the chain in the parameter space as a function of the step number. During the burn-in period, the values of the parameters move quite clearly towards the values that nature has used to produced the observed data. Only when the chain will be effectively sampling from the sub-space around the maximum of the likelihood, the values of the parameters will be fluctuating quite randomly around their true values. If this criteria is chosen, all the parameters should be checked, as there is a possibility that some parameters reach their true values before the rest.

Both methods are related, because as long as any single parameter is not around its most probable value, the posterior will never reach its maximum value. Nevertheless, in a well-behaved situation, that is, in ergodic Markov chains, all cases converge after the burn-in period to the same region around the maximum likelihood point regardless of the initial starting point [226], as shown in Fig. 3.1.

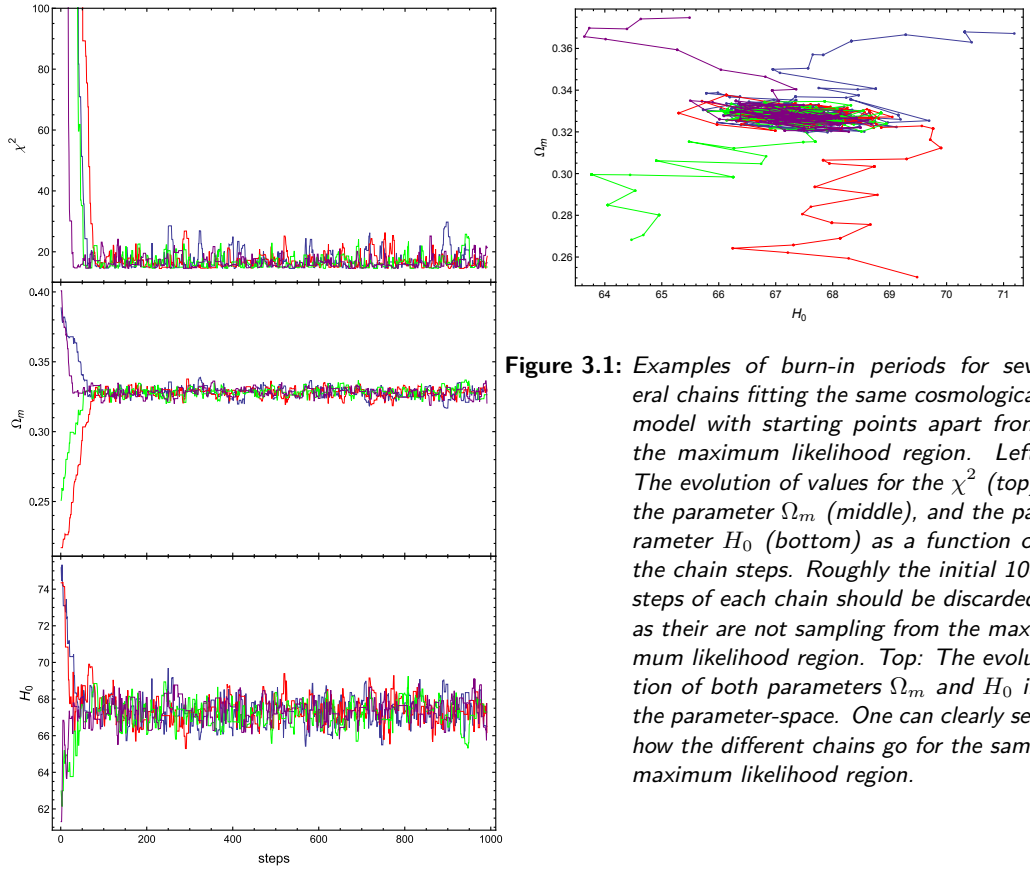

Figure 3.1: *Examples of burn-in periods for several chains fitting the same cosmological model with starting points apart from the maximum likelihood region. Left: The evolution of values for the χ^2 (top), the parameter Ω_m (middle), and the parameter H_0 (bottom) as a function of the chain steps. Roughly the initial 100 steps of each chain should be discarded, as their are not sampling from the maximum likelihood region. Top: The evolution of both parameters Ω_m and H_0 in the parameter-space. One can clearly see how the different chains go for the same maximum likelihood region.*

Convergence

Once the burn-in period is set, the chain will start to sample properly from the posterior distribution. However, we cannot be fully sure if the distribution obtained from a finite MCMC chain is the unknown target posterior, or if their properties are equivalent, because the amount of collected points in the sample necessary to characterize the posterior distribution is also unknown a priori [207].

The definition of a converged chain is that it has reached the equilibrium distribution of the Markov chain. Theoretically, for an infinite chain this convergence is defined asymptotically: it can be proved that the chain reaches the invariant distribution within infinity steps [174]. Nevertheless, practically this is impossible to achieve, and in order to save time and computational effort, the convergence is defined as the point/time after which the sampled distribution describes the properties of the target one with enough accuracy. Therefore, assessing the convergence of the MCMC chain means to know when to stop collecting points, as the gathered number of sample points is large enough to describe properly the posterior distribution [226].

There is not a single definition or prescription to check the convergence. The most common test is based on the convergence ratio,

$$r = \frac{\sigma^2}{\sigma_0^2} \, , \tag{3.20}$$

which compares the variance of the mean of the sample σ^2 with the one of the underlying distribution σ_0^2 (usually taking $\sigma_0^2 = 1$ as standard distributions are used). This parameter is used alone by itself and inside other tests, as in the Gelman-Rubin test [102] for example, where the convergence of a MCMC run with several parallel chains is tested measuring the variance within and between chains.

Nonetheless, this approach requires parallel chains to be run, and it might result hardware consuming. Thus, alternatively, less demanding but equally rigorous convergence test can be used. In our work we have referred mainly to the method described in [82]. After the burn-in period, and approaching convergence, the MCMC does not depend anymore on the initial starting points and, when the maximum likelihood value is also (approximately) found, the sample points are not as highly correlated as they were in the first steps of the chain. Exploiting this fact, a convergence ratio based on the spectral analysis of a single MCMC chain can be performed. First, one has to compute the discrete power spectrum of the finite MCMC chain,

$$P_j = |a_N^j|^2 \, , \tag{3.21}$$

where its Fourier coefficients are

$$a_N^j = \frac{1}{\sqrt{N}} \sum_{n=0}^{N-1} x_n \exp\left[2\pi i \frac{j}{N} n\right] \, , \tag{3.22}$$

N being the length and x_n the n-th element of the chain. The discrete spectrum ranges from $j = 1$ to $j = N/2 - 1$, the wave number for each case being $k_j = 2\pi j/N$.

Any correlation in the power spectrum could be related to a position dependence along different elements of the chain. In fact, small scale correlations are unavoidable, due to the Markovian nature of the MCMC algorithm; in this case, the power spectrum will look similar to that of a random walk. Thus, a convergence criterion can be build by demanding a flat uncorrelated (white noise) spectrum for every scale bigger than a given threshold k^* (i.e. for $k < k^*$, or equivalently, a minimum number of steps in the MCMC).

For this purpose, an analytical template for the power spectrum is defined, where the flat white noise spectrum at large scale ($k_j \ll k^*$) and the correlation at small scale ($k_j \gg k^*$) are connected at the turn-over scale, k^*. The expression for this template is the following

$$P'_j = P_0 \frac{(k^*/k_j)^\alpha}{1 + (k^*/k_j)^\alpha} \ , \tag{3.23}$$

where the shape of the spectrum is tuned by the already mentioned turn-over scale k^*, but also by the parameter P_0 which gives the white noise amplitude at $k \to 0$, and by α. Once the template is fitted to the power spectrum of the chain, as shown in Fig. 3.2, the analysis of the resulting values of k^* and P_0 gives the sought convergence information.

The white noise amplitude P_0 is related to the previously mentioned convergence ratio, $r \approx P_0/N$, and it has to be lower than 0.01 in order to fulfill the convergence criteria. The turn-over scale k^* gives the point where the correlated spectrum becomes flat. The bigger k^* is, the more points are drawn from the true underlying posterior distribution without being affected by the small scale correlation of the chain. This convergence criteria is achieved with a value of $j^* \gtrsim 20$. However, this spectral analysis has to be done for each free parameter of the model that is being varied in the chain.

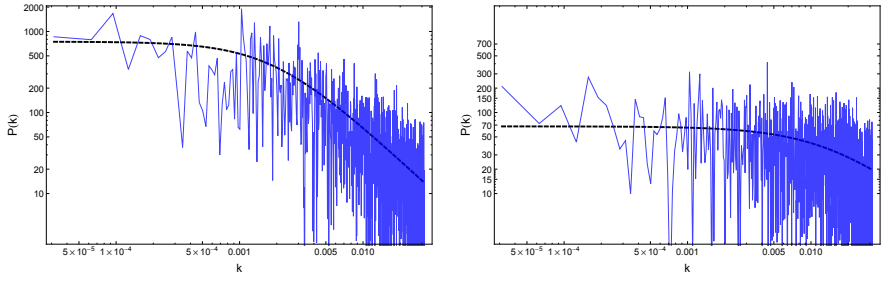

Figure 3.2: *Examples of discrete power spectrum (thin blue) and its template fitted (dashed black) for two parameters of the same cosmological model. The parameter of the left panel is converged, though it still shows small-scale correlations. This is not the case for the parameter of the right panel, where small-scale correlations barely appear and the spectrum is mostly flat white noise.*

3.2.2 Metropolis-Hastings Algorithm

The Metropolis-Hastings algorithm [114, 168] is one of the most used algorithms for MCMC sampling in cosmology [61, 148], and well-known in the Bayesian inference approach in general. The Markov chain created with this algorithm has as its invariant distribution the target posterior $P(\boldsymbol{\theta}|\mathbf{d})$ which is built through Bayes' theorem.

This is done through the transition probability $T(\boldsymbol{\theta}_t, \boldsymbol{\theta}_{t+1})$, which specifies the probability that the chain at state $\boldsymbol{\theta}_t$ moves to the next step $\boldsymbol{\theta}_{t+1}$. This transition is defined by a proposal density $Q(\boldsymbol{\theta}_t, \boldsymbol{\theta}_{t+1})$ and an acceptance criteria $\alpha(\boldsymbol{\theta}_t, \boldsymbol{\theta}_{t+1})$ given by

$$\alpha(\boldsymbol{\theta}_t, \boldsymbol{\theta}_{t+1}) \equiv \min\left\{1,\ \frac{P(\boldsymbol{\theta}_{t+1}|\mathbf{d})Q(\boldsymbol{\theta}_{t+1}, \boldsymbol{\theta}_t)}{P(\boldsymbol{\theta}_t|\mathbf{d})Q(\boldsymbol{\theta}_t, \boldsymbol{\theta}_{t+1})}\right\}\ , \tag{3.24}$$

so that the transition probability is

$$T(\boldsymbol{\theta}_t, \boldsymbol{\theta}_{t+1}) = \alpha(\boldsymbol{\theta}_t, \boldsymbol{\theta}_{t+1})\, Q(\boldsymbol{\theta}_t, \boldsymbol{\theta}_{t+1})\ . \tag{3.25}$$

$\alpha(\boldsymbol{\theta}_t, \boldsymbol{\theta}_{t+1})$ determines if the next point $\boldsymbol{\theta}_{t+1}$ in the chain is a proper candidate compared to the current state $\boldsymbol{\theta}_t$, and gives the acceptance/rejection probability. The proposal density $Q(\boldsymbol{\theta}_t, \boldsymbol{\theta}_{t+1})$ used in this algorithm is usually a multivariate Gaussian centered on the current state $\boldsymbol{\theta}_t$, but it can be simply any fixed density from which we can draw samples.

The Metropolis-Hastings algorithm works as follows. At step $t+1$ a tentative new state $\boldsymbol{\theta}'$ is generated from the proposal density $Q(\boldsymbol{\theta}_t, \boldsymbol{\theta}')$. To decide whether to accept the new state or not, a random number u, from the range $[0, 1]$ is generated and compared with the acceptance criteria $\alpha(\boldsymbol{\theta}_t, \boldsymbol{\theta}')$: if $u \leq \alpha$ the new state is automatically accepted and will become the new starting point of the next step in the algorithm, i.e. $\boldsymbol{\theta}_{t+1} = \boldsymbol{\theta}'$; otherwise, it is rejected, and the new step $t+1$ will start again from the same point of the step t, i.e. $\boldsymbol{\theta}_{t+1} = \boldsymbol{\theta}_t$. Thus, the new state is accepted only with a probability α.

To compute the acceptance probability we need to compute the probability ratios $P(\boldsymbol{\theta}_{t+1}|\mathbf{d})/P(\boldsymbol{\theta}_t|\mathbf{d})$ and $Q(\boldsymbol{\theta}_{t+1}, \boldsymbol{\theta}_t)/Q(\boldsymbol{\theta}_t, \boldsymbol{\theta}_{t+1})$. But in the case when the proposal density is a simple symmetrical density, such as a Gaussian centered on the current point $\boldsymbol{\theta}_t$, then the latter factor cancels out and the Metropolis-Hastings method simply involves the ratio of the posterior probability of the target density at the two points. In any case, with the above definitions for the transition probability, the detailed balance condition is fulfilled [148, 225],

$$P(\boldsymbol{\theta}_t|\mathbf{d})\, T(\boldsymbol{\theta}_t, \boldsymbol{\theta}_{t+1}) = P(\boldsymbol{\theta}_{t+1}|\mathbf{d})\, T(\boldsymbol{\theta}_{t+1}, \boldsymbol{\theta}_t)\ , \tag{3.26}$$

which means that the posterior $P(\boldsymbol{\theta}|\mathbf{d})$ is the invariant distribution of the Markov chain we are sampling it.

3.3 Model selection

Hitherto, we have seen which methods can be used to fit certain given observational data by some models defined through a set of theoretical parameters. But this is not the end of the story. In most of the cases, the most important part is to compare statistical results about a model with those from another model. So, a maybe even more important task in a statistical analysis is to find a way to assess which one of the constrained models is most probably the true one behind the observations, and this usually translates into finding a way to set which model fits best the data. The critical point is to define objective and quantitative criteria for such a comparison to be performed. Also in this case, we have many methods and approaches [82].

The first and rough approach is simply to compare the values of the minimum in the χ^2 achieved by each model when their parameters are fitted. In general, and broadly speaking, the lower is the achieved χ^2 the better the model fits the data. But this only works when models with the same number of degree of freedom are compared, that is, models which have the same number of free parameters.

Models with different numbers of parameters have different capabilities to adapt to the same data; in general, those with more free parameters should be able to match better any peculiarity shown by the data but this is done, of course, adding degrees of freedom (i.e. more parameters). Thus, when comparing models with a different number of parameters, the gain in the fit of the model with more parameters should be enough to justify the extra parameters, otherwise it is said that they are *overfitted*. To account for the extra parameters in a fast and easy way, the reduced χ^2 is used,

$$\chi^2_{red} = \frac{\chi^2}{DoF} = \frac{\chi^2}{N_{data} - k - 1} \,, \tag{3.27}$$

where the degree of freedom DoF depends on the number of points included in the data N_{data} and the dimension of the parameter space or the number of parameters k. In this way, the flexibility of any model due to its bigger number of free parameter is taken into account. Any model correctly fitted should achieve a χ^2_{red} around unity, but still we might have problems. If a model fitting certain data gets a χ^2_{red} far bigger than unity, it could also mean that possibly the observational errors from the data might be underestimated. On the contrary, if the χ^2_{red} is noticeably smaller than one, it means that the errors are overestimated and the model fits the data too easily.

However, there are other forms and tools better suited to model selection, which can also show in a easier way whether a model is overfitted or not. For instance, various prescriptions to compute the approximate evidence, namely the Information Criteria, are possible [233]. These criteria tend to take into account the number of parameters that the considered model has, as well as the number of data points, so that an appropriate information criterion can be built.

For example, we have the Akaike information criterion (AIC) which is defined as

$$AIC = -2 \ln L_{max} + 2k \, , \tag{3.28}$$

where the first term with the maximum likelihood L_{max} is equivalent to the minimum χ^2 and k is the number of free parameter of the model [7]. This criterion, though, makes the assumption that the number of data points is very big, towards infinity. So in the cases where data points are not enough, the AIC could prefer overfitted models (although there is a correction term accounting this).

Another information criterion, closely related to the Akaike one, is the Bayesian information criterion (BIC) [206],

$$BIC = -2 \ln L_{max} + k \ln N_{data} \, , \tag{3.29}$$

where apart of the maximum likelihood L_{max} and the dimension of the parameter space k, it also takes into account the number of data points N_{data}. As this information criterion takes into consideration both the number of parameters and data points, it severely penalizes models with unnecessary parameters. Nevertheless, the assumption of large sample size or number of points is still necessary.

The last criterion we are showing, though there are lots of more, is the deviance information criterion (DIC), introduced in [215]. The definition, in its simplest incarnation, is

$$DIC = 2\langle \chi^2 \rangle - \chi^2_{min} \, , \tag{3.30}$$

where it relates the mean χ^2 with its minimum. This criterion is very useful when the posterior of the model is sampled through MCMC techniques because all the statistical data required by its computation is given by the distribution obtained.

3.3.1 Bayesian Evidence

All these information criteria can only be used to make comparisons between models, but they do not give an absolute quantification of the model's quality or of the goodness of fit. This goal is better achieved by the evidence, also named as the marginal likelihood or integrated likelihood [246], as shown previously in Eq. (3.4).

Evidence is mainly used for model comparison, which is done by computing the ratio of the Evidences of two different models,

$$B_{ij} = \frac{E(\mathcal{M}_i)}{E(\mathcal{M}_j)} \, . \tag{3.31}$$

This ratio is called the Bayes factor [227]. When taking the logarithm of this ratio, we can properly compare the statistical weight of the model $\mathcal{M}_i$ over $\mathcal{M}_j$ according to the so-called Jeffreys' scale [110].

It has to be stressed that, from its definition, the Evidence clearly does not depend on the model parameters or, better and equivalently, these are automatically taken into account by the marginalization procedure on the likelihood, so that more parameters automatically correspond to a smaller Evidence value. But it is also clear how it could depend on the prior function, so, when models with different priors are compared, there might be an intrinsic bias. That is the reason why large-range uninformative priors are the best choice (when possible).

Moreover, the same Jeffreys' scale suffers some arbitrariness in the statement of the "strength of evidence", so that, in general, one could simply prefer to rely on the absolute value of the Bayes factor instead of trying to argue a "degree of strength" in favor or not of one model or another.

Table 3.2: *Values for various evidence difference and their convention according the Jeffreys' scale.*

$\ln B_{ij}$	Odds	Strength of evidence
< 1.0	$\lesssim 3:1$	Inconclusive
1.0	$\sim 3:1$	Weak evidence
2.5	$\sim 12:1$	Moderate evidence
5.0	$\sim 150:1$	Strong evidence

For the computation of the Evidence we have used the nested sampling algorithm [172], which transforms the problem of computing the evidence of Eq. (3.4) to a one dimensional integral that can be evaluated through Monte Carlo technique. For a thorough insight, see [211].

The method starts from the same definition of Evidence we have given in the previous section, Eq. (3.4). We define X as the fraction of the total prior volume such that $dX = \Pi(\boldsymbol{\theta})d\boldsymbol{\theta}$ is the prior volume corresponding to the likelihood range $[L,\, L + dL]$ and $X(L)$ is defined as the prior volume fraction which corresponds to a likelihood value bigger than L. With these definitions now Eq. (3.4) can be rewritten simply as

$$E = \int_0^1 L(X)\, dX \ , \tag{3.32}$$

where $L(X)$ is the inverse of $X(L)$. Thus, the multi-dimensional original integral in the definition of the Evidence is now a one-dimensional integral which ranges from zero prior volume for the case of maximum likelihood, $X(L = L_{max}) = 0$, to the full prior range where the likelihood is minimal, $X(L = 0) = 1$.

Knowing some m points of prior volume X_i and their corresponding likelihood values $L_i = L(X_i)$, the integration in Eq. (3.32) can be numerically approximated by the well-known trapezoid method, summing columns of width $w_i = \frac{1}{2}(X_{i-1} - X_{i+1})$ and

height $L_i = L(X_i)$, so that

$$E = \int_0^1 L(X)\, dX \simeq \sum_{i=1}^{m} w_i\, L_i \ . \tag{3.33}$$

The nested algorithm for this numerical integration starts selecting N random points of equal prior volume X_i and sorting them from minimum likelihood (the full prior range, $X = 1$) to maximum likelihood (zero prior volume, $X = 0$),

$$1 > X_1 > X_2 > \cdots > X_N > 0 \ . \tag{3.34}$$

The iteration works by taking the biggest X_i value (corresponding to the available lowest likelihood, i.e. the lowest index i once sorted) and increasing the evidence by $w_i\, L_i$ before this X_i point is discarded. Then, in order to substitute the discarded point, the iteration starts again selecting a new random point from the full range $[0, X_i]$, i.e. the new point must have a corresponding likelihood greater than the previously discarded value L_i. The new set of N values is sorted again, and the process is performed N_s times in total. In such a way, in terms of the parameter space, the most external layer of equal likelihood is numerically integrated at each step, peeling off nested layers of Evidence, while advancing to the center of maximum likelihood.

The number of random X_i points at each step, N, is generally smaller than the number of total iterations, N_s, so that most of the initial N points will be probably discarded once their contribution to the integration are taken into account. The process keeps going up the likelihood surface until almost the entire prior volume is evaluated up to a desired precision. For an optional refinement, a final summation of $X_i(L_1 + \cdots + L_N)/N$ to the evidence can be done in order to take into account the remaining N points which are left apart at the final step. Therefore, if this last step is taken, the total m terms in the summation of Eq. 3.33 will be $m = N + N_s$.

The exact values for the variable $X = (X_1, X_2, ...)$ may be unknown, but statistically can be deduced that the enclosed prior volume decreases logarithmically on average with each step of the nested sampling method [211]. Therefore, the proper sampling for X should be linear in $\ln X$ instead of linear in X, and a simple way to implement this is by taking $X_i \equiv e^{-i/N}$.

The implementation of the nested algorithm is easy when the results of an MCMC run are available, because one has already the likelihood values evaluated in many points in the parameter space compatible with the prior range. Thus, all the initial N random points are directly sampled from the likelihood list given by the MCMC run and they are assigned their corresponding X_i label when their sorting of Eq. 3.34 is done. The condition for the subsequent points, which are randomly drawn at each step from the interior of the remaining prior volume ($X_{i+1} < X_i$), is easily set by requiring to have a higher likelihood than the discarded point ($L_{i+1} > L_i$). Their X_i label is again statistically assigned when the points are sorted at each step. Due to this statistical uncertainty, the nested algorithm should be performed several times in order to get an average value of the Evidence.

PART II

Cosmological constrain from real data

4 Cosmological constraints on unified dark matter-energy models

As we have summarized in Sec. 1.3, while the effects of the two elusive dark components, i.e. dark matter and dark energy, are clear and widely accepted, no strong clue about their nature has been obtained so far, and we have seen that a huge variety of explanations for both of them can be provided. Normally considered as separated components of the universe, their effects could perhaps be explained by one sole component. In the literature we find the two most popular ways to achieve this unification.

The first one makes the phenomenological assumption of an explicit parametrization of the equation of state in terms of the scale factor so that the pressure/density ratio ($w = p/\rho$) has a nearly null value at the early stages of the evolution, whereas it becomes negative enough ($w < 1/3$) at late epochs. These models have different names as Unified Dark Fluid approach or quartessence, but they are more usually called Unified Dark Matter (UDM) models, which is a colloquial simplification of 'unified dark matter-energy', the original meaning of the acronym UDM first proposed in [163] [1]. For early proposals of this sort one can also check references [42, 130], whereas [36] reviews the topic.

The second broad idea relies on putting forward some specific coupling/interaction, i.e. writing the respective energy conservation equations of dark matter and dark energy so that they have extra terms which cancel each other out in the conservation equation of the sum of the two fluids.

For UDM models it is far from trivial how the two components are to be separated so as to analyze physical quantities such as the speed of sound, required for a full fledged analysis of cosmological constraints (i.e. a study including perturbations). In general, this is an involved problem, and, in some sense, it still remains open. Despite this difficulty, we find these models offer an interesting arena to test whether non-conventional evolutions are admissible or even preferable.

In contrast, the coupling/interaction displays a natural separation scheme right from its inception, and typically models in which the dark energy is a scalar field are used to model the dark energy component. But the complexity of the equations, along with the

[1] We will follow the original proposal, reinstating the naming 'unified dark matter-energy' as the meaning of the well-established acronym UDM.

extra number of degrees of freedom, precludes the power to reconstruct explicitly the evolution of the background (depending on the scale factor). In fact, this is only possible if initial conditions are set, or in other words, if a specific path is chosen in the highly multidimensional phase-space of the model. These are basically the so-called coupled quintessence scenarios, which, despite their interest, lay beyond the main focus of this project (see [16] for one of the first representative contributions to the topic). But just let us mention that recent sound observational support for some such scenarios have been presented [200, 230].

UDM models, which are our main interest here, have in general been found to be somewhat inconsistent because they have to become indistinguishable from ΛCDM in order to fit the observational data [204]. This is the case for the generalized Chaplygin gas for example, which even in non linear evolution fails condensation to act as CDM [43]. But among the different UDM models, a new class has emerged that offers a way out of that difficulty: models with a fast transition between a matter-driven-like era and a dark-energy-driven-like era. They are believed to provide an alternative and defendable explanation of the accelerated expansion of the universe [182], as they can fit the observational data quite well while they display interesting and different new features. Besides, fast transitions UDM models with scalar fields are also compatible with observational data [37].

The theoretical reasoning on which fast transition UDM models rely provides hints towards well mathematically/analytically-defined expressions for their equation of state parameter $w_{\mathrm{U}DM}$, as discussed in [182], but this parametrization scheme turns out to be computationally expensive when tested with likelihood techniques. Taking into account this, and without a fundamental model, it is worth to consider simple phenomenological models for the fast transition UDM in order to achieve as much theoretical progress as possible from analytical calculations. A simple model, gentle on computations, must be one whose most important variables required for the numerical calculations can be expressed analytically. Thus, instead of implementing the UDM model in the equation of state $w_{\mathrm{U}DM}$, as in [182], we believe a more convenient way to proceed analytically is to prescribe the evolution of the UDM energy density at the level of the Hubble factor itself [48]. Here we present (in Sec. 4.1) two parametrizations for these UDM set-ups with fast transition. Then we describe (in Sec. 4.2) the CMB, Galaxy Clustering and type Ia Supernovae data we use to constrain the models. After that we discuss (in Sec. 4.3) our most relevant results, and in particular, whether the models are statistically favoured or not as compared to the concordance scenario, ΛCDM. To close up, we present some final conclusions (in Sec. 4.4).

4.1 Phenomenological fast transition unified dark matter-energy

The background geometry considered for the phenomenological UDM models in this chapter is a spatially flat Friedman-Lemaître-Robertson-Walker (FLRW) metric, $ds^2 = -dt^2 + a^2(t)\delta_{ij}dx_i dx_j$, where $a(t)$ is the scale factor as a function of the cosmic time t, and δ_{ij} is the Kronecker delta. We will consider perfect fluids with densities ρ_i as sources; and taking $8\pi G = c = 1$, the Friedman equation takes the form

$$H^2 = \left(\frac{\dot{a}}{a}\right)^2 = \sum_i \frac{\rho_i}{3}, \tag{4.1}$$

where $H = \dot{a}/a$ is the Hubble function and the dot denotes differentiation with respect to the cosmic time. If we introduce the corresponding fractional matter-energy densities

$$\Omega_i(a) = \frac{\rho_i(a)}{3H^2(a)}\ , \tag{4.2}$$

Eq. (4.1) becomes

$$E^2(a) = H^2/H_0^2 = \sum_i \Omega_i(a), \tag{4.3}$$

with H_0 representing the Hubble factor at present.

Being more specific about the sources, we need to clarify the role and form of our proposed UDM fluid: we want a UDM fluid which exhibits a fast transition from the pure dark matter stage to a scenario that resembles a ΛCDM set-up. From [48], we borrow the analytical form

$$\Omega_{UDM} = \Omega_t \left(\frac{a_t}{a}\right)^3 + \Omega_\Lambda \left[1 - \left(\frac{a_t}{a}\right)^3\right] \Theta(a - a_t), \tag{4.4}$$

with $\Theta(a - a_t)$ playing the role of a transition function, and a_t the value of the scale factor at which the transition happens. We can easily see that for $a < a_t$ the fluid behaves like a pure dark matter fluid, with density $\Omega_t \left(a_t/a\right)^3$. For $a > a_t$, the fluid will rather have a density with the expression $\left(\Omega_t - \Omega_\Lambda\right)\left(a_t/a\right)^3 + \Omega_\Lambda$, thus resembling a ΛCDM scenario, as intended.

Note that, as shown in Ref [239], any description for the fluid content driving the background evolution of a UDM setting can be mapped into that of a scenario in which dark matter and dark energy are separate components. This is so because the large-scale evolution is only sensitive to the total energy-momentum tensor, and not to the features of its separate components. But this issue should be examined under a different light if one considered perturbations, because the unified and non-unified scenarios do not have perfectly matching perturbations, as also discussed in Ref. [76, 240].

Given the properties of the transition function, one can match the usual dark matter density Ω_c with the term $\Omega_t a_t^3$. Thus, the total matter component will be $\Omega_m = \Omega_t a_t^3 + \Omega_b$ when the baryonic matter term is also considered. In principle, the Hubble factor would suffer from a degeneracy between its terms proportional to Ω_c and Ω_b if we were using only low redshift observational data. Given that, we are going to use high redshift CMB data as well, for which this degeneracy is broken. Moreover, the use of the CMB data makes it necessary to add a radiation term, Ω_r [238], which has no influence on the late-time expansion, but is fundamental in the early stages of the universe history. Thus, all in all, Eq. (4.3) can be finally written as

$$E^2(a) = \Omega_c a^{-3} + \Omega_\Lambda \left[1 - \left(\frac{a_t}{a}\right)^3\right] \Theta(a - a_t) + \Omega_b a^{-3} + \Omega_r a^{-4} \,. \tag{4.5}$$

For the purpose of the statistical analysis we will perform, it is also useful to take advantage of the fact that the parameter Ω_Λ can be written as a function of the other parameters by simply evaluating at the present time the Friedmann equation, Eq. (4.5), finally having

$$\Omega_\Lambda = \frac{1 - \Omega_c - \Omega_b - \Omega_r}{(1 - a_t^3)\Theta(1 - a_t)} \,. \tag{4.6}$$

The last ingredient missing to provide a round model for this UDM transition is the choice of Heaviside-like functions. We will propose two different ones; the first model for the transition will be:

$$\Theta(a - a_t) = \frac{1}{2} + \frac{1}{\pi} \arctan\left(\beta\pi(a - a_t)\right) \,; \tag{4.7}$$

whereas the second transition function considered will be:

$$\Theta(a - a_t) = \frac{1}{2}\left[1 + \tanh\left(2\beta(a - a_t)\right)\right] \,. \tag{4.8}$$

In both cases, the transition happens slowlier than in a pure Heaviside function, with the parameter β mainly controlling the velocity of the transition; that parameter is in fact (and in both cases) the value of the first derivative with respect to the scale factor of the transition functions, evaluated at the transition point a_t.

4.2 Observational data

In this section we specify details of the observational data sets we have used for our analysis, as well as the analytical expression of the χ^2 we are going to minimize in order to perform our statistical Bayesian analysis. We use CMB shift parameters as explained in Sec. 2.3.1, Union2.1 SNe catalog as standard candles of Sec. 2.2, and specific BAO data (Sec. 2.3.2) coming from galaxy clustering (GC). A Gaussian prior for the Hubble constant is also assumed: $H_0 = 100\,h$ km s^{-1} Mpc^{-1} $= 69.6 \pm 0.7$ km s^{-1} Mpc^{-1} [30];

thus, its contribution to the total χ^2 is the following:

$$\chi^2_{H_0} = (100\,h - H_0)^2/\sigma^2_{H_0}. \tag{4.9}$$

The total χ^2 will be, of course, the sum of all the considered terms:

$$\chi^2 = \chi^2_{CMB} + \chi^2_{SN} + \chi^2_{GC} + \chi^2_{H_0}\,. \tag{4.10}$$

4.2.1 CMB shift parameter data

As explained in Sec. 2.3.1, CMB data are taken from [238], where distance priors for l_a and R were derived from *Planck* first release data [3]. The mean values for these parameters are

$$\big(\langle l_a\rangle,\, \langle R\rangle,\, \langle \Omega_b h^2\rangle\big) = (301.57,\, 1.7407,\, 0.02228)\,, \tag{4.11}$$

and taking their 1σ errors from Eq. (2.42), we construct the full covariance matrix $\mathbf{C}_{CMB}$ from the given correlation matrix of Eq. (2.43). In order to write the CMB contribution to the χ^2, we first define the difference vector between the model and observations as

$$\mathbf{X}_{CMB} = \begin{pmatrix} l_a - \langle l_a\rangle \\ R - \langle R\rangle \\ \Omega_b h^2 - \langle \Omega_b h^2\rangle \end{pmatrix}\,, \tag{4.12}$$

and using the inverse of the covariance matrix $\mathbf{C}_{CMB}$, the CMB contribution to the χ^2 is

$$\chi^2_{CMB} = \mathbf{X}^T_{CMB}\mathbf{C}^{-1}_{CMB}\mathbf{X}_{CMB}\,. \tag{4.13}$$

4.2.2 Supernovae Ia data

The SNe Ia data set we have used is the Union2.1 compilation [220], made of 580 Type Ia Supernovae distributed in the redshift interval $0.015 < z < 1.414$. The data set provides full statistical plus systematics covariance matrix for the distance modulus $\mu(z_i)$ Eq. (2.24) of each SN. All the SNe uncertainty as the SNe Ia absolute magnitude alongside constants as the value of the Hubble constant H_0, for example, are included in the nuisance parameter μ_0, so that the distance modulus $\mu(z_i)$ of Eq. (2.29) can be rewritten in this case as

$$\mu(z) = 5\log_{10} d_L(z) + \mu_0\,, \tag{4.14}$$

where the dimensionless luminosity distance d_L in a spatially flat universe is given by

$$d_L(z) = (1+z)\int_0^z \frac{dz'}{E(z')}\,. \tag{4.15}$$

In order to get the χ^2 contribution, first we define the difference vector between the model and the observed magnitudes

$$\mathbf{X}_{SN} = \begin{pmatrix} \mu_{model}(z_1) - \mu_{obs}(z_1) \\ \dots \\ \mu_{model}(z_{\mathcal{N}}) - \mu_{obs}(z_{\mathcal{N}}) \end{pmatrix} . \tag{4.16}$$

However, instead of simply compute the usual χ^2 term as $\chi^2_{SN} = \mathbf{X}^T_{SN} \cdot \mathbf{C}^{-1} \cdot \mathbf{X}_{SN}$, we follow the marginalization of Sec. 3.1.3 to get rid of the nuisance parameter μ_0. This way, the SNe Ia χ^2 contribution becomes

$$\chi^2_{SN} = a + \log \frac{d}{2\pi} - \frac{b^2}{d} , \tag{4.17}$$

where: $a \equiv \mathbf{X}^T_{SN} \cdot \mathbf{C}^{-1} \cdot \mathbf{X}_{SN}$, $b \equiv \mathbf{X}^T_{SN} \cdot \mathbf{C}^{-1} \cdot \mathbb{1}$, and $d \equiv \mathbb{1}^T \cdot \mathbf{C}^{-1} \cdot \mathbb{1}$, with $\mathbb{1}$ standing for the identity matrix.

4.2.3 Galaxy Clustering data

The Galaxy Clustering (GC) data we use are the measurements of $H(z)r_s(z_d)/c$ and $D_A(z)/r_s(z_d)$ from the two dimensional two-point correlation function measured by [63] and [64], respectively at $z = 0.35$ using the SDSS DR7 Luminous Red Galaxies sample [132], and at $z = 0.57$ using the CMASS galaxy sample from BOSS [92]. Here, $H(z)$ is the Hubble function defined in Eqs. (4.3) - (4.5); and $D_A(z)$ is the angular diameter distance of Eq. (2.15) in the case of spatially flat universe:

$$D_A(z) = \frac{c}{1+z} \int_0^z \frac{dz'}{H(z')} . \tag{4.18}$$

The comoving sound horizon $r_s(z_d)$ is evaluated at the drag epoch [88], whose redshift z_d is given in Eq. (2.44). The mean values and the 1σ errors for these quantities are

$$\begin{aligned} \left\langle \frac{H(0.35)r_s(z_d)}{c} \right\rangle &= 0.0434 \pm 0.0018 \\ \left\langle \frac{D_A(0.35)}{r_s(z_d)} \right\rangle &= 6.60 \pm 0.26 , \end{aligned} \tag{4.19}$$

with normalized correlation coefficient $r_{0.35} = 0.0604$; and

$$\begin{aligned} \left\langle \frac{H(0.57)r_s(z_d)}{c} \right\rangle &= 0.0454 \pm 0.0031 \\ \left\langle \frac{D_A(0.57)}{r_s(z_d)} \right\rangle &= 8.95 \pm 0.27 \end{aligned} \tag{4.20}$$

with normalized correlation coefficient $r_{0.57} = 0.4874$. The GC contribution is calculated independently for each redshift, $\chi^2_{GC} = \chi^2_{GC1} + \chi^2_{GC2}$. In each case, taking into account the correlation r_i between the two observables, the usual term of $\chi^2_{GCi} = \mathbf{X}^T_{GCi} \cdot \mathbf{C}^{-1} \cdot \mathbf{X}_{GCi}$ can be directly expanded as

$$\chi^2_{GCi} = \frac{1}{1-r_i^2}\left(\frac{X1^2_{GCi}}{\sigma^2_{1i}} + \frac{X2^2_{GCi}}{\sigma^2_{2i}} - 2r_i\frac{X1_{GCi}}{\sigma_{1i}}\frac{X2_{GCi}}{\sigma_{2i}}\right), \tag{4.21}$$

where $X1_{GCi}$ and $X2_{GCi}$ are the difference between observation and models for each quantity

$$X1_{GCi} = \frac{H(z_i)r_s(z_d)}{c} - \left\langle\frac{H(z_i)r_s(z_d)}{c}\right\rangle, \tag{4.22}$$

$$X2_{GCi} = \frac{D_A(z_i)}{r_s(z_d)} - \left\langle\frac{D_A(z_i)}{r_s(z_d)}\right\rangle. \tag{4.23}$$

4.3 Statistical analysis on fast transition unified dark matter-energy

The statistical analysis will be performed by minimizing the χ^2 function using the Markov Chain Monte Carlo (MCMC) Method [61, 148, 226] described in Sec. 3.2. The statistical convergence of each MCMC round has been tested using the spectral method given by [82] and described in Sec. 3.2.1. In order to state the effective statistical weight and validity of our UDM models, we have also analyzed the ΛCDM model using the expression in Eq. (1.39)

$$E^2_{\Lambda CDM}(z) = (\Omega_c + \Omega_b)a^{-3} + \Omega_r a^{-4} + \Omega_\Lambda\,, \tag{4.24}$$

and the quiessence model [137, 187]

$$E^2_Q(z) = (\Omega_c + \Omega_b)a^{-3} + \Omega_r a^{-4} + \Omega_\Lambda a^{-3(1+w)}. \tag{4.25}$$

In both cases, the usual matter density Ω_m has been split into the dark matter Ω_c and the baryonic Ω_b densities terms, in order to have the same parameters as the UDM models.

The priors on the parameters that we have chosen are as general as possible: a positive dark matter density between $0 < \Omega_c < 1$; a positive baryonic matter density smaller than the dark matter density $0 < \Omega_b < \Omega_c$; a positive Hubble function $E(a) > 0$ for all a values; and $0 < a_t < 1$ because we want the transition to actually have happened.

Fig. 4.1 shows confidence regions for the ΛCDM and quiessence models, while a summary of the results of our statistical analysis can be found in Tab. 4.1 where the reduced best-fit χ^2 is also shown. However, more robust conclusions for the model selection can be drawn only from the Bayes factors after having computed the statistical evidence. For the computation of the evidence we have used the nested sampling algorithm [172] explained in Sec. 3.3.1. The Bayes factor [227] is obtained comparing the UDM

Table 4.1: *Summary of constraints. Median values for the free parameters and the corresponding value for the parameters Ω_Λ and q_0, using CMB, GC and SNe data. The value for the minimum χ^2_{red} and the Bayesian ratios with respect to ΛCDM are also shown.*

Model	arctan	tanh	ΛCDM	quiessence
h	$0.69508^{+0.00068}_{-0.00064}$	$0.69587^{+0.00065}_{-0.00061}$	$0.6906^{+0.0090}_{-0.0093}$	$0.696^{+0.016}_{-0.017}$
Ω_c	$0.2445^{+0.0011}_{-0.0012}$	$0.2436^{+0.0011}_{-0.0011}$	$0.245^{+0.011}_{-0.010}$	$0.243^{+0.012}_{-0.012}$
Ω_b	$0.04626^{+0.00024}_{-0.00026}$	$0.04597^{+0.00023}_{-0.00024}$	$0.04692^{+0.00097}_{-0.00096}$	$0.0461^{+0.0024}_{-0.0022}$
parameter $\sharp 4$	$a_t = 0.170^{+0.010}_{-0.011}$	$a_t = 0.1809^{+0.0099}_{-0.0105}$	$-$	$w = -1.029^{+0.062}_{-0.067}$
β	552^{+75}_{-69}	771^{+71}_{-67}	$-$	$-$
Ω_Λ	$0.7091^{+0.0015}_{-0.0013}$	$0.7103^{+0.0014}_{-0.0013}$	$0.708^{+0.011}_{-0.012}$	$0.712^{+0.014}_{-0.015}$
q_0	$-0.56907^{+0.00099}_{-0.00120}$	$-0.57181^{+0.00085}_{-0.00103}$	$-0.562^{+0.017}_{-0.017}$	$-0.597^{+0.085}_{-0.087}$
χ^2_{red}	0.9501	0.9498	0.9488	0.9503
$lnB_{i\Lambda}$	$+0.791$	$+0.902$	0	-0.242

and quiessence models with the ΛCDM, assumed as reference model, and the results are shown in the last column of Tab. 4.1.

Fig. 4.2 show the constraints on the free parameters for the models Eq. (4.7) and Eq. (4.8) respectively, and the Tab. 4.1 summarise the results. The late time dark energy density Ω_Λ is also computed in this case, evaluating the Eq. (4.6) and inferring its statistics from the MCMC output on the main fitted parameters. We also study the deceleration function, which is used as a further marker to characterize the behaviour of our models and, eventually, to better distinguish them from ΛCDM:

$$q = -1 - \frac{d\log E(a)}{d\log a}. \tag{4.26}$$

The deceleration function evaluated today $q_0 \equiv q(a=1)$ is also shown on the Tab. 4.1, while its global evolution is represented in Fig. 4.3.

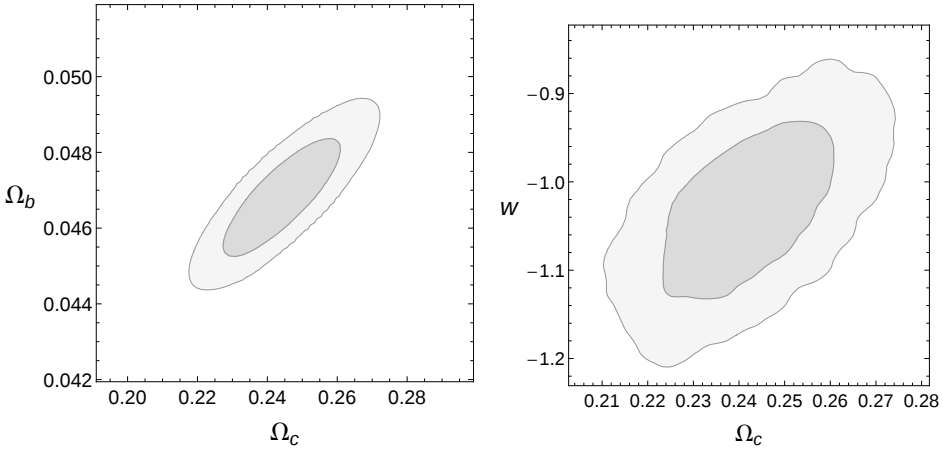

Figure 4.1: *Contour plot for the ΛCDM (left) and quiessence (right) models, dark grey areas are 1σ region and light grey areas are 2σ region.*

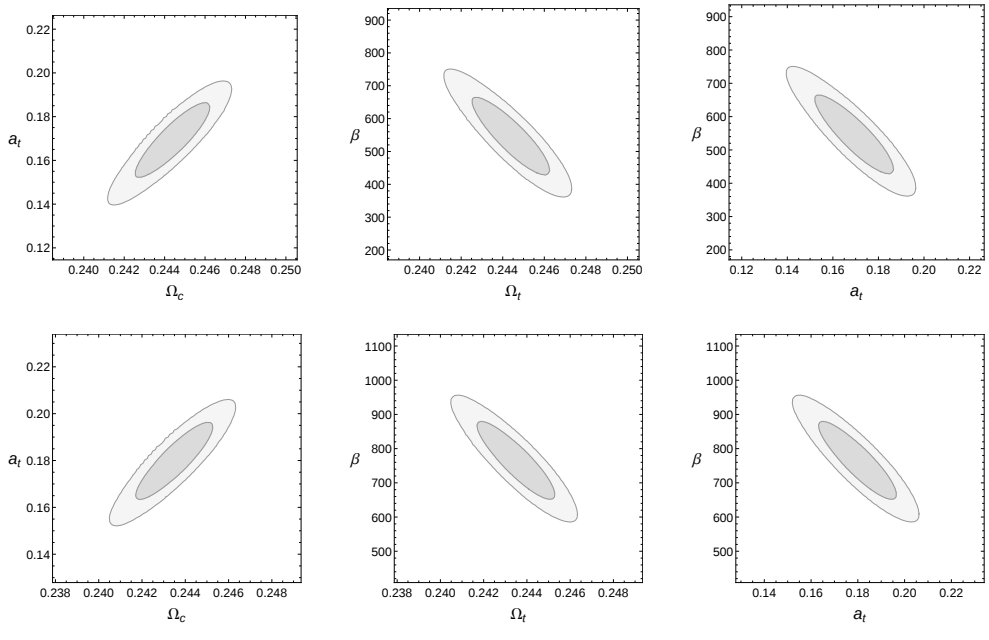

Figure 4.2: *Confidence regions for the arctan (top) and tanh (bottom) models; dark grey areas are 1σ region and light grey areas are 2σ region.*

4.4 Take-home lesson about unified dark matter-energy models

Results from the Bayesian Evidence show that the proposed UDM models cannot be discarded in favour of the ΛCDM model, as it can be seen in the Tab. 4.1. All models

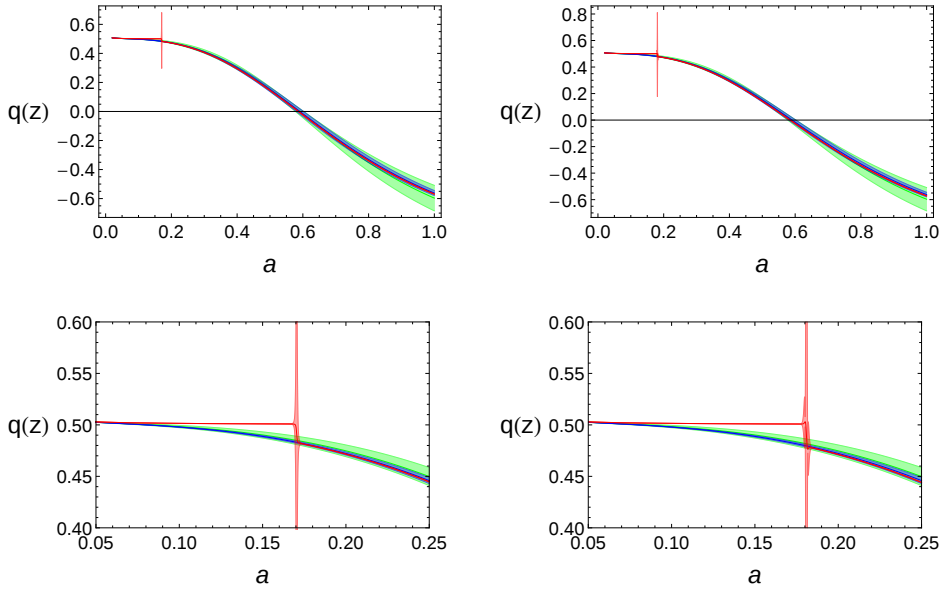

Figure 4.3: *Evolution of the deceleration parameter for the arctan (left, red) and tanh (right, red) models, compared with the deceleration of the ΛCDM (blue) and quiessence (green). Top figures show the entire evolution, bottom figures are zoomed in the transition.*

get a very similar evidence compared each other. Even if the difference, according to the so-called "Jeffreys' scale" [110], still falls in the "inconclusive evidence" range for all of them when compared to ΛCDM, we have to highlight the higher values obtained by our UDM models.

When comparing the same parameters in different models, we can see that in all four models the best fits have similar values. Nevertheless, comparing the errors of the the UDM models to the ones of ΛCDM and quiessence models, the former ones are slightly smaller than last ones.

These differences in the errors can be well appreciated in the plot of the deceleration Fig. 4.3, where the differences are highlighted by the dependence of the deceleration on all free parameters of the models. We can see that, in general, the biggest error corresponds to the quiessence model, and to the lowest the UDM models. However, during the transition, due to the rapid change of the transition function, the error of the deceleration in the UDM models greatly increases. We can also appreciate that the slight difference between the deceleration function of the UDM models and the ΛCDM model progressively increases until the transition, but then both UDM and ΛCDM models decelerate in almost the same manner. Besides, the deceleration function of all the models, including quiessence, has a quite similar behaviour (and value range) during the whole evolution of the universe.

This transition is characterized by the transition functions of Eq. (4.7) and (4.8), which is shaped by the parameters a_t and β. For both UDM models the transition occurs in the past, and is centered around $a_t \approxeq 0.17 - 0.18$. The transitions occur very fast, in a narrow fraction of the entire cosmic time.

The mayor differences between the UDM models and ΛCDM occur before the transition. In this way, they could be considered as early time deviations from ΛCDM, where there would be no need for dark energy in the past. Furthermore, the dark sector of the universe could be explained by a single UDM fluid instead of the two components necessary with ΛCDM.

5 Cosmological constraints on a unified dark matter-energy scalar field model

In this chapter we will consider a well studied variation of ΛCDM: the Unified Dark Fluid approach, also known as quartessence, sometimes as Unified Dark Energy, but more usually known as Unified Dark Matter[1]. A plethora of UDM models have been proposed, see [36] for a review, after the pioneering introduction of the Chaplygin gas [32, 42, 130]. The unification of dark matter and dark energy is an interesting approach that assumes the existence of a single fluid capable of accounting for both the accelerated expansion at late times and the large-scale structure formation at early times, due to the evolution of its equation-of-state (EoS) and speed of sound. In principle this is more efficient than postulating two different fluids and equally valid, since the nature of the fluids is still elusive. It also has the advantage of evading, by definition, the coincidence problem [216].

A serious issue in most UDM models is the presence of an effective speed of sound that can be very different from zero during the cosmological evolution. This prevents the dark fluid to cluster below a thresholding scale (the Jeans scale) [101, 121, 183]. In addition, the evolution of the gravitational potential may also give rise to a strong signature in the Integrated Sachs Wolfe (ISW) effect [34]. It is therefore crucial to make sure that the single dark fluid is able to cluster and create the observed cosmic structures as well as reproducing the well-known pattern of CMB temperature anisotropies [58]. However, for the majority of UDM models in the literature, these requirements, together with the necessity of having a background evolution that complies with observations, leads to severe fine-tuning of the parameters, to the point that the models become almost indistinguishable from ΛCDM, and are thus less interesting [107, 181, 204, 205].

The problem of the lack of clustering, or production of oscillations, can be avoided with a technique introduced in [35]. In particular, the dark fluid is a scalar field, φ, with a non-canonical kinetic term, i.e., a term $f(\dot{\varphi}^2)$ instead of the standard $\dot{\varphi}^2/2$. In this way it was possible to build a UDM model with a small effective sound speed that allows structure formation and has a weak ISW effect, being compliant with weak lensing data [53, 54]. This model has, however, the same background evolution as ΛCDM. A more recent alternative are the so-called UDM models with fast transition where, during a short

[1] Again, we will follow the original proposal of 'unified dark matter-energy'.

period, the effective speed of sound can be large, but is otherwise zero. This produces a fast transition between a CDM-like era, with an Einstein-de Sitter evolution, and an accelerated DE-like era, and allows for strucure formation. In addition, these models are not forced by construction to have the same background evolution as ΛCDM and are free from the problem of fine-tuning the parameters that plagues many UDM models.

The dynamics of UDM models with fast transition can be prescribed in three different ways: starting from either the EoS w, the pressure p or the energy density ρ. The first UDM model with fast transition was introduced in [182] and prescribed the evolution of p. The pressure and energy density were related by a barotropic EoS, $p = p(\rho)$ and the perturbations were adiabatic. A second UDM model with fast transition was presented in [37] and was built from a k-essence [19, 60] scalar field Lagrangian (see also [74, 131, 193, 194]). This model also prescribed p but, differently from the first one, since it is based on a scalar field the perturbations are naturally non-adiabatic [41, 80], allowing for a small Jeans length even when the speed of sound is non negligible. The model also contains a future attractor that acts as an effective cosmological constant[2], ρ_∞, i.e., an asymptotic limit $w = -1$ is built in. A third UDM model with fast transition was proposed in [48]. This is a phenomenological model, with the dynamics prescribed through the fluid density ρ, and it has adiabatic perturbations.

Models with a fast transition might also be a step towards a unified description of dark matter, dark energy and inflation [152] but, regardless of that possibility, they are considered among the most promising UDM models [17]. Even though they are built with the goal of enabling structure formation, it is also important to test them at the background level since they may have a background evolution quite distinct from ΛCDM. In particular, such tests will constrain the rapidity of the transition and may already give an indication whether the allowed rapidity range favors structure formation. The phenomenological UDM model, and variations of it, were recently constrained at background level in [143]. In the present work, we apply Supernova, BAO and CMB data to test the scalar field UDM model of [37], constraining its parameters and making a statistical model comparison with both ΛCDM and the phenomenological UDM model of [48] tested in [143].

In the rest of the chapter, we present in Sec. 5.1 the UDM model that will be tested in Sec. 5.3 using the data and methods described in Sec. 5.2. We conclude with a summary and some remarks in Sec. 5.4.

[2]A scalar field with a potential that admits a minimum $V_0 = V(\phi_0) \neq 0$ is equivalent to a cosmological constant $\rho_\Lambda = V_0$ and a scalar field in a potential $\tilde{V} = V - V_0$.

5.1 Computation of the Hubble function

We consider the scalar field UDM model proposed in [37], where the evolution of the pressure has the following form:

$$p(a) = -\rho_\infty \left\{ \frac{1}{2} + \frac{1}{2} \tanh \left[\frac{\beta}{3} \left(a^3 - a_\mathrm{t}^3 \right) \right] \right\} . \tag{5.1}$$

This model allows for a fast transition in the pressure evolution, since for large values of β the $\tanh$ function tends to a step function. The transition occurs at a scale factor a_t, with rapidity parameterized by β, while ρ_∞ parameterizes the pressure amplitude. The fluid goes from an Einstein-de Sitter DM era ($p = 0$ at early times), through $p(a_t) = -\rho_\infty/2$ at transition, to a DE era at late times (with p reaching $-\rho_\infty$ the sooner for faster transitions).

Considering a Friedmann-Lemaître-Robertson-Walker (FLRW) background metric (and a frame with proper time coicinding with the cosmic time), the density can be derived from the pressure using the energy conservation equation

$$\dot{\rho} = -3H \left(\rho + p \right) = -3H\rho \left(1 + w \right) , \tag{5.2}$$

where $w = p/\rho$ is the EoS and the dot means differentiation with respect to time. The density is obtained from the pressure by integrating Eq. (5.2):

$$\rho(a) = \rho_\infty \left\{ \frac{1}{2} + \frac{3}{2\beta} a^{-3} \ln \left(\cosh \left[\frac{\beta}{3} \left(a^3 - a_\mathrm{t}^3 \right) \right] \right) \right\} + \rho_0 a^{-3} . \tag{5.3}$$

The integration introduces another constant. It is usual to choose it as the amplitude of a "CDM sector of the UDM": ρ_0, defined at $a_0 = 1$. Note that the density does not have a fast transition, since the $\ln(\cosh)$ function is not a step function. The density decreases smoothly from its maximum amplitude at $a = 0$, through $\rho(a_t) = (\rho_0 a_t^{-3} + \rho_\infty)$ at transition, to ρ_∞ when $a \to \infty$. Note also that for fast transitions (large β) and after the transition, $\tanh \sim 1$ and $\ln[\cosh(x)]/x \sim 1$, and thus $p \sim -\rho_\infty$ and $w \sim -\rho_\infty/(\rho_\infty + \rho_0)$. This means that fastest models become degenerate and are more similar to ΛCDM than the slower ones (with the exception of the singular case $\beta = 0$).

The UDM model contains thus four parameters: ρ_0, ρ_∞, β and a_t. With this choice of parameters, the density is written as the sum of three parts: the CDM-like term $\rho_c(a) = \rho_0 a^{-3}$, a constant term $\rho(a) = \rho_\infty/2$ and the $\ln\cosh$ term, with the latter two defining a "dark energy sector". To compare UDM models with ΛCDM, it is useful to define today's densities for these two sectors. Introducing the critical density today, $\rho_{cr} = 3H_0^2$, we define the two dimensionless density parameters:

$$\Omega_c = \frac{\rho_0}{3H_0^2} \tag{5.4}$$

and

$$\Omega_{DE} = \frac{\rho_\infty}{3H_0^2}\,. \tag{5.5}$$

All the background probes we will use in the likelihood analysis depend on the Hubble function

$$E^2(a) = H^2/H_0^2 = \Omega_r a^{-4} + \Omega_b a^{-3} + \Omega_{\rm UDM}(a)\,, \tag{5.6}$$

where Ω_b and Ω_r are the baryonic matter and radiation [238] densities and

$$\Omega_{\rm UDM}(a) = \Omega_c a^{-3} + \Omega_{DE}\left\{\frac{1}{2} + \frac{3}{2\beta}a^{-3}\ln\left\{\cosh\left[\frac{\beta}{3}\left(a^3 - a_{\rm t}^3\right)\right]\right\}\right\}\,. \tag{5.7}$$

The four parameters Ω_{DE}, Ω_c, β and a_t are not all independent. Indeed, applying Friedmann's equation, $\sum\Omega_i = 1$, we can write

$$\Omega_{DE} = \frac{1 - \Omega_r - \Omega_b - \Omega_c}{\frac{1}{2} + \frac{3}{2\beta}\ln\left\{\cosh\left[\frac{\beta}{3}\left(1 - a_{\rm t}^3\right)\right]\right\}}. \tag{5.8}$$

The definition of two sectors allows the introduction of an EoS of the dark energy sector,

$$w_{\rm DE}(a) = \frac{p(a)}{\rho(a) - \rho_0 a^{-3}}\,, \tag{5.9}$$

in addition to the EoS $w(a) = p(a)/\rho(a)$.

We finally note that an explicit analytical Lagrangian can be written for this model, since the general Lagrangian for a UDM scalar field φ, within the framework of k-essence is

$$L = L_G + L_\varphi = \frac{1}{16\pi G}R + L_\varphi(\varphi, X), \tag{5.10}$$

where X is the kinetic term and the pressure can be identified with the term $p = L_\varphi(\varphi, X)$.

5.2 Observational data

We test the model with a Markov Chain Monte Carlo (MCMC) exploration of the parameter space [61, 148] as described in Sec. 3.2, combining various probes of the expansion history of the Universe: luminosity distances to type Ia supernovae (Sec. 2.2.2), baryon acoustic oscillation scale parameter and also Alcock-Paczynski distortion parameter (Sec. 2.3.2), and CMB distance priors (Sec. 2.3.1). These various data sets are uncorrelated and thus the total χ^2 used in the analysis is simply the sum

$$\chi^2 = \chi^2_{CMB} + \chi^2_{BAO} + \chi^2_{SN}\,. \tag{5.11}$$

Besides these observations, we also include some broad and flat conditions as priors: dark matter density must be positive $0 < \Omega_c < 1$; baryonic matter density must be positive and smaller than the dark matter density $0 < \Omega_b < \Omega_c$; the Hubble function must be positive for all values of the scale factor a, $E(a) > 0$; and $0 < a_t < 1$ because we want the transition to actually have happened. Finally, the Hubble constant H_0 is analitically marginalized in the SN likelihood and is left as a free parameter, with a broad flat prior, in the BAO and CMB likelihoods.

5.2.1 CMB shift parameter data

In order to reduce the volume of the parameter space in the MCMC analysis, it is useful to include the so-called CMB distance priors [238] in our analysis. As explained in Sec. 2.3.1, these are priors on the CMB shift parameters, geometrical quantities that effectively summarize the CMB data, since they capture the degeneracies between the parameters that determine the CMB power spectrum [237]. These CMB distance priors are the same explained in the previous Chap. 4, using the same χ^2_{CMB} construction as in Eq. 4.13.

5.2.2 Supernovae Ia data

As in the previous analysis [143] of Chap. 4, we use the same Union2.1 compilation [220], which provides not only the distance modulus $\mu(z_i)$ for each SN, but also the full statistical plus systematics covariance matrix of all 580 Type Ia Supernovae of the catalog. The additive nuisance parameter μ_0 of Eq. 4.14, involving the values of all constants from the distance modulus, is again marginalized according Sec. 3.1.3, yielding the same expression for the χ^2_{SN} as Eq. 4.17.

5.2.3 Baryonic Acoustic Oscillation data

Unlike the previous analysis [143] of Chap. 4, we will now use the baryon acoustic oscillation scale parameter $A(z)$ of Eq. (2.49) and the Alcock-Paczynski distortion parameter $F(z)$ of Eq. (2.52) provided by the WiggleZ Dark Energy Survey [44], as the BAO observables. They probe the volume-averaged distance $D_V(z)$ of Eq. (2.50) and the angular-diameter distance $D_A(z)$ of Eq. (2.15), which can be expressed in the following way for the spatially flat case,

$$D_A(z) = \frac{c}{(1+z)} \int_0^z \frac{dz'}{H(z')} \,. \tag{5.12}$$

WiggleZ measured these observables in three overlapping redshift bins, with effective redshifts $(z_1,\, z_2,\, z_3) = (0.44,\, 0.60,\, 0.73)$. The data values are

$$\mathbf{X}_{obs} = (A_1, A_2, A_3, F_1, F_2, F_3) \tag{5.13}$$

$$= (0.474, 0.442, 0.424, 0.482, 0.650, 0.865) \tag{5.14}$$

with correlated errors described by the covariance matrix

$$\mathbf{C}_{BAO} = 10^{-3} \times \begin{pmatrix} 1.156 & 0.211 & 0.0 & 0.400 & 0.234 & 0.0 \\ 0.211 & 0.400 & 0.189 & 0.118 & 0.276 & 0.336 \\ 0.0 & 0.189 & 0.441 & 0.0 & 0.167 & 0.399 \\ 0.400 & 0.118 & 0.0 & 2.401 & 1.350 & 0.0 \\ 0.234 & 0.276 & 0.167 & 1.350 & 2.809 & 1.934 \\ 0.0 & 0.336 & 0.399 & 0.0 & 1.934 & 5.329 \end{pmatrix} . \tag{5.15}$$

The BAO contribution to the total χ^2 is

$$\chi^2_{BAO} = \mathbf{X}^T_{BAO} \cdot \mathbf{C}^{-1}_{BAO} \cdot \mathbf{X}_{BAO} \tag{5.16}$$

where $\mathbf{X}_{BAO} = (\mathbf{X}_{obs} - \mathbf{X}_{mod})$ is the difference vector in this case.

5.3 Statistical analysis on unified dark matter-energy scalar field model

We ran a set of Markov chains on the five-dimensional parameter space $(h, \Omega_c, \Omega_b, a_t, \beta)$, using the following three-step procedure. We start by running a short preliminary chain of around 20 000 iteration in order to find the region of maximum probability density. Then we make a second run for around 50 000 iterations to find a tentative covariance matrix. Finally, we start the final chain, using the previously found covariance matrix as a proposal step. The final chain has around 200 000 points and we assess its convergence using the ratio of variances proposed in [82] and explained in Sec. 3.2.1.

Besides the UDM scenario, we also ran an MCMC for the ΛCDM scenario. Fig. 5.1 shows the posterior probabilities for each parameter of the UDM and ΛCDM models, along with 1- and 2-σ two-dimensional confidence regions. Tab. 5.1 gives the corresponding median and marginalized 1-σ interval for each chain parameter and some derived parameters.

The constraints on the three standard parameters are similar in the two models. The probability contours of the Hubble parameter vs densities show the usual anti-correlations that arise because Hubble function and distance measurements probe physical densities $\Omega_i h^2$. The main new feature is a slight correlation between the scale factor of transition a_t and Ω_c, especially for higher values of a_t (and a corresponding anti-correlation with h). This degeneracy broadens the Ω_c contours, being responsible for the decrease of precision in the Ω_c estimate quoted in Tab. 5.1. This differs from the behavior found in the analysis of the phenomenological UDM models [143] of the previous Chap. 4, where the constraint on Ω_c was found to be stronger than in the ΛCDM model, even though the evidence was not conclusive in favor of that UDM model.

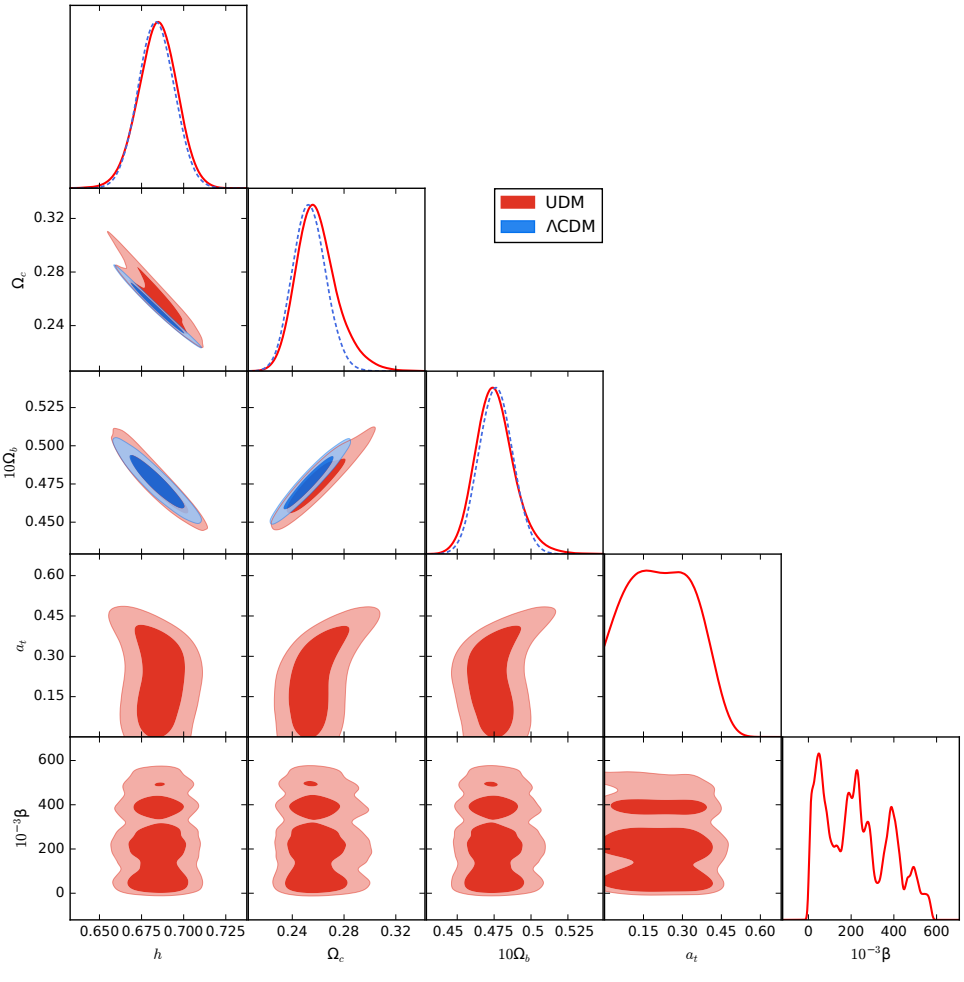

Figure 5.1: *Posterior distribution from the full-range MCMC chains. Diagonal panels: one-dimensional marginalized posterior distributions for UDM (red, solid lines) and ΛCDM (blue, dashed lines) parameters. Off-diagonal panels: 1- and 2-σ two-dimensional marginalized contours for UDM (red) and ΛCDM (blue) parameters.*

Table 5.1: *Median and 1-σ uncertainty for the UDM and ΛCDM model parameters, from the full-range MCMC chains.*

Parameter	UDM	ΛCDM
h	0.685 ± 0.012	0.684 ± 0.011
Ω_c	$0.259^{+0.012}_{-0.018}$	0.253 ± 0.013
Ω_b	$0.0476^{+0.0011}_{-0.0014}$	0.0476 ± 0.0011
a_t	$0.22^{+0.13}_{-0.15}$	-
β	$227500^{+200000}_{-200000}$	-
Ω_{DE}	$0.693^{+0.019}_{-0.013}$	0.699 ± 0.014
w_{DE}	$-1.011^{+0.011}_{-0.0039}$	-1
w	$-0.735^{+0.013}_{-0.015}$	-1

For model comparison purposes, we start by noticing in Tab. 5.2 that the UDM best-fit has a lower χ^2 value than found in the ΛCDM analysis. This may be due to over-fitting, and indeed the best-fit reduced χ^2 is larger than for the ΛCDM case. A more robust way to compare the models is through the ratio of the model evidences, i.e., the Bayes factor [227]. We compute the evidences with an implementation of the nested sampling algorithm [172] explained in Sec. 3.3.1. In particular, we use 10^3 sample points, chosen randomly, and compute the evidence in up to 10^4 steps. We repeat the procedure 100 times, varying the sample points, and quote the average evidence from the 100 realizations. We obtain a Bayes factor very close to 0, and thus the model comparison is highly inconclusive, according to Jeffreys' scale [110].

Table 5.2: *Values from 5 methods to perform model comparison between UDM, ΛCDM and the phenomenological UDM.*

	UDM	ΛCDM	UDM_{ph}
χ^2_{min}	552.59	552.77	552.75
χ^2_{red}	0.9478	0.9449	0.9481
$\ln B_{U\Lambda}$	-0.0196	0	0.6850
BIC	584.485	571.902	584.644
DIC	553.250	552.770	552.814

With a Bayes factor so close to 0, we decided to investigate if the behaviour would be any different when using approximate evidence measures, namely information criteria. The Bayesian Information Criterion (BIC) is defined as [206]

$$\mathrm{B}IC = -2\ln \mathrm{L}_{max} + k \ln N. \tag{5.17}$$

Since the nunber of data points used, N, was the same for the two models, BIC directly penalizes the lower minimum χ^2 of UDM with the higher number of free parameters k. For the Deviance Information Criterion (DIC), we followed [215] and computed

$$\mathrm{DIC} = 2\left\langle \chi^2 \right\rangle - \chi^2_{\mathrm{min}}, \tag{5.18}$$

where the average χ^2 were computed from the chains and not with the nested sampling code. The results are consistent with the comparison of evidences in that both information criteria assign a weak but inconclusive preference to ΛCDM.

We are also interested in comparing the stronger motivated scalar field UDM model with the phenomenological one. For that purpose we made a new analysis of the latter, testing it with the same set of data used in our present analysis. The results from this second model comparison analysis are also summarized in Tab. 5.2. Model comparison between the two UDM models is more direct, since both have the same number of parameters and data points. Therefore, BIC reduces to a measure of the best-fit, which is slightly in favor of the scalar field model. It is interesting to note that even though the scalar field model shows a better best-fit χ^2, it has a worse χ^2 behaviour on average and consequently a lower DIC value and evidence. Again, the analysis does not favor one model over the other, with a weak but inconclusive preference for the phenomenological model.

We can also look at the dark energy sector of the UDM model. A DE density may be defined as in Eq. (5.5) and its value computed from Eq. (5.8) as a function of all the other parameters. The corresponding EoS is dynamical and can be computed from Eq. (5.9). The constraints on $\Omega_{\mathrm{D}E}$ and $w_{\mathrm{D}E}(a=1)$, derived from the MCMC chains, are shown in Tab. 5.1. The evolution of $w_{\mathrm{D}E}$ for the best-fit parameter values is shown in Fig. 5.2, together with its 1-σ variation. Notice that even though w_{DE} is phantom after the fast transition, approaching $w_{DE} \sim -1$ today from the negative side, the UDM fluid does not violate the null energy condition because its EoS, also shown in Fig. 5.2, does not cross the phantom divide.

We have thus a UDM model with fast transition that is viable given background data. Let us analyze now the behavior of its core parameters: the scale factor at the transition, a_t, and the rapidity of transition, β. Their constraints, also shown in Fig. 5.1 and Tab. 5.1, are weak. The 1-σ interval for the transition redshift ranges from $z \sim 2$ to $z \sim 13$, while β does not show a correlation with the other parameters. The posterior probability of β shows a peaked structure. Looking in more detail into the likelihood values, we see the likelihood is essentially flat for $\beta > 1000$. The peaks in the β posterior indicate the chain is not yet converged for this parameter, meaning there was not enough time to sample the unbound flat distribution and the chain remained occasionally stuck in some

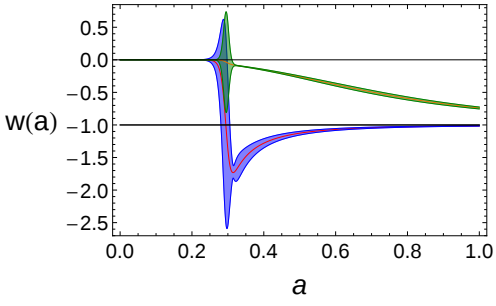

Figure 5.2: *Evolution of the EoS of the UDM fluid (green) for the best-fit model parameters, including derived uncertainty, and EoS of the DE section of the fluid (blue).*

positions of the flat distribution. We have thus found that β is unbound from above, which reflects the fact that for $\beta >\sim 1000$ the Hubble function is essentially identical for all β values. On the other hand, β is bound from below, we do not impose a $\beta > 0$ prior in the analysis.

These considerations led us to probe the low β limit with better resolution. For this, we ran new chains considering only the range $\beta < 100$. Given the low level of correlation with other parameters, we keep the density parameters fixed at the best-fit values, varying only β and a_t. The scale factor at the transition must be kept free, since it is coupled with β in the evolution of pressure and density, Eqs. (5.1) and (5.3), even though a degeneracy with β does not show in Fig. 5.1. Notice also that this setup will artificially tighten the a_t constraint due to its correlation with Ω_c. We also ran separate chains for each data set and show the results in Fig. 5.3. We see now a sharp peak in the posterior of β at $\beta = 0$ that had not been picked up before. This point is basically a singularity in the space of UDM parameters. Indeed, in the $\beta = 0$ limit, Eq. (5.7) no longer presents a transition and the model reduces to ΛCDM, which explains its high likelihood. No transition, also means that the value of a_t is meaningless, which explains the horizontal very narrow contour seen in the contour plot at $\beta = 0$. As β increases, the Hubble function starts to deviate from ΛCDM, until $\beta \sim 15$, and afterwards it approaches it again. This explains the dip in the β posterior seen in all data sets. This effect is especially dramatic for the CMB shift parameters, which are able to reject the range $\beta < 40$.

Regarding a_t, the noisy structure seen in its posterior corresponds to the $\beta = 0$ solution, while the rest of the probability volume lies along a well-defined degeneracy in the (β, a_t) plane. Indeed, in this regime of low β the data is able to pick up the degeneracy that arises from the fact that a slower transition needs to occur earlier in order to be able to reach today's density ratio. We fit the degeneracy direction with a cubic polynomial $\beta - \beta_0 = (a_t/0.22)^3$ to capture the (β, a_t) dependence in the Hubble function, Eqs. (5.6) and (5.7). Here $\beta_0 = 54.6$ is the average chain value of β for $a_t = 0$, while $a_t = 0.22$ is the median a_t value quoted in Tab. 5.1. With these assumptions, we find the following

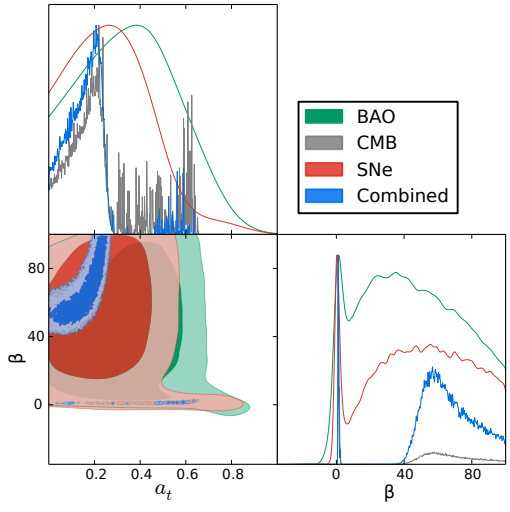

Figure 5.3: *Posterior distribution from the slow transition MCMC chains. Diagonal panels: one-dimensional marginalized posterior distributions for the UDM model parameters, for different data sets (SN, BAO, CMB, all combined). Off-diagonal panel: 1- and 2-σ two-dimensional (a_t, β) contours for the same data sets.*

1-σ constraint

$$(\beta - \beta_0)\left(\frac{a_t}{0.22}\right)^{-3} = 24.8 \pm 5.9\,. \tag{5.19}$$

We also need to look with higher resolution to the intermediate regime of β, to compare the likelihoods of the slow transition models with the fast transition ones. This is the regime of β of a few hundreds, where the $\tanh$ function is not yet a step function. We thus ran a new (a_t, β) chain restricted to $\beta < 2000$. The results of this analysis are shown in Fig. 5.4. The distribution of a_t is now well constrained, showing a tight peak with a low-likelihood tail for low a_t values. The tail corresponds to the slow transition regime studied in Fig. 5.3. This result then strongly favors intermediate and fast transitions over slow ones. This is confirmed by the posterior of β that shows a strong increase from slow to fast transition, peaking around $\beta = 600$. After the peak, the distribution falls down slowly with a long tail, which is just an effect of the strong prior $\beta < 2000$ imposed in this analysis, since the likelihood is essentially flat. We see then that the β distribution is far from Gaussian and we can only find a lower limit for this parameter. From the $\Delta\chi^2$ values, we find a 1-σ lower bound of $\beta > 300$.

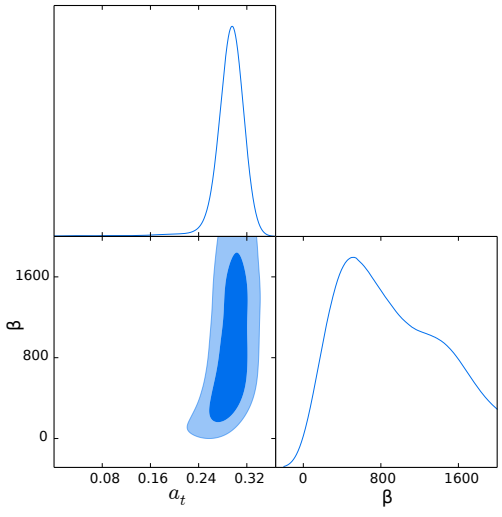

Figure 5.4: *Posterior distribution from the fast transition MCMC chains. Diagonal panels: one-dimensional marginalized posterior distributions for the UDM model parameters. Off-diagonal panel: 1- and 2-σ two-dimensional (a_t, β) contours.*

5.4 Take-home lesson about unified dark matter-energy scalar field model

In recent years, UDM models, for which DM and DE are described by a single dark fluid, have become increasingly popular and drawn a considerable amount of attention. These models are undoubtedly promising candidates as effective theories. In this chapter, we have constrained a UDM scalar field model with a fast transition. The scalar field used has a non-canonical kinetic term in its Lagrangian and accounts for both the accelerated expansion of the Universe at late times and the clustering properties of the large-scale structure of the Universe at early times. The fast transition occurs between a Einstein-de Sitter CDM-like epoch and a late accelerated DE-like epoch and allows to have a sufficiently small Jeans length, even if the speed of sound is large during the transition, because this happens so quickly that its effect is negligible.

In this study we investigated the regimes of slow and fast transition and assessed if they were distinguishable at background level. For this analysis we tested the models using Supernovae Ia, Baryon Acoustic Oscillations and CMB distance data. We have found a lower bound constraint for the rapidity of the transition $\beta > 300$, independent of the transition redshift. Slow transition models $\beta < 40$ were ruled out, while low-likelihood intermediate rapidity models featured a correlation between the transition redshift and rapidity.

The evidence of this model was compared to the evidences of ΛCDM and a phenomenological fast transition UDM model that was previously shown to be a good-fit to background data. In both comparisons the model fared well, with no conclusive evidence against it.

The preference found for the fast transition regime, which is the condition required for enabling structure formation, together with the fact that the model has a similar evidence to ΛCDM and is a k-essence type physically motivated model with a well defined Lagrangian, makes it an interesting and viable fundamental cosmological model.

PART III

Forecasting future observations

6 Forecast and analysis of the Sandage-Loeb test

Most, if not all the probes we have described in Sec 2 involve a time (or better redshift) integral of the Hubble parameter $H(z)$, and are enough to constrain quite satisfactorily the geometry and energy content of the universe. But on the other hand, one expects that the accelerated expansion of the universe will make the redshift of a given astrophysical object exhibit a drift over time, which should in principle be amenable to giving an accurate description of that very same expansion once an underlying model is chosen. While looking for a possible temporal variation of the redshift of extra-galactic sources, Sandage came in 1962 [11] to the conclusion that it should indeed occur. But, alas, the limited technological resources on deck at that epoch, lead to the inference that a measurement time interval of the order of 10^7 years would be required for a signal detection. When new spectroscopic techniques became available to astrophysicists, Loeb paid a new visit to the concept [157] in 1998, and concluded that the new technology would allow a reduction in the observation time interval to a few decades. This cosmological redshift drift measurement, also called Sandage-Loeb (SL) test, would then provide a direct proof of the accelerated expansion of the universe. In fact, this temporal variation is directly related to the expansion rate at the source redshift, being thus a direct measurement of the Hubble function.

The last results of the *Planck* survey [6], have made us enter an ultra high precision cosmology era; and other future surveys are scheduled which should further improve the accuracy of cosmological measurements, as for example *Euclid* [142], *Wide-Field Infrared Survey Telescope (W-First)* [214] or Square Kilometer Array (SKA) [2].

Thus, in the near future, available resources will allow us to start thinking about the next level of cosmological observational data, to which the cosmological redshift drift will contribute, complementing the previously cited surveys. However, even with future precision radio telescopes, the measurement of the SL effect represents a difficult enterprise [134], as it demands several years of observation (usually some decades) to register enough signal-to-noise ratio so as to yield a possible reliable detection of the cosmological redshift drift signal. Best candidate objects for a feasible detection of this faint signal are good Hubble flow tracers as far as possible [165]. As put forward by Loeb [157], an auspicious target would be the Lyman-α forest measurements of distant

quasars (QSO). With spectroscopic techniques to be operational in the near future, like CODEX (COsmic Dynamics and EXo-earth experiment) experiment [155], proposed for the European-Extremely Large Telescope (E-ELT), or radio telescopes as SKA [136], these observations will grant access to direct measurements of the Hubble parameter up to redshift ~ 5, a so far not yet observed redshift range. Thus, the SL test will open a new "cosmological window".

Due to the near future possibilities to measure the cosmological redshift drift, this type of observations has recently drawn some attention. The reconstruction of the theoretical SL signal that different cosmological models would produce has been explored quite extensively [234, 250]. It comes out that the range and variety of the different cosmological redshift drift signals created by various models is remarkable: from those created by different proposals for dark energy's equation of state or modified gravity [70, 170], to the ones created by backreaction in an inhomogeneous universe without the presence of dark energy [138]; from the peculiar signals for Lemaître-Tolman-Bondi models [18, 247], to even a null signal [167] for the $R_h = ct$ Universe, or other several exotic scenarios [22, 23, 25, 78, 169, 249]. SL signals have been used as an hypothetical geometric cosmic discriminant [103, 104, 111] to show the corresponding improvement in the constraints that can be achieved due to the degeneracy breaking (around 20% of improvements for dark energy parameters and even 65% for matter density). SL mock data sets have been applied with similar results as cosmic observational discriminators to test other various models, like interactive dark energy models [106, 251], modified gravity [105, 151], and other exotic cosmologies [248, 254]. Their power to differentiate models has been exploited also in the context of the model-independent approach of cosmography [166, 252]. Besides, some new approaches [135] can lead to ambitious ideas, such as real-time cosmology [184].

We stress again the fact that the measurement of the cosmological redshift drift is not an easy pursuit, and requires quite a lot of planning due to the large observation time interval of the survey. Thus, foreseeing the contribution and behaviour of this type of measurements is important, and we precisely carry out here a quite thorough forecast analysis of cosmological redshift drift constraints on various cosmological models. The analysis includes a comparison between the proposed SL data with other future planned surveys, generating mock data based on the given specifications. Furthermore, unlike previous works, all mock data sets are generated in a fully model independent way, with no fiducial cosmological model chosen to generate the points. In Sec. 6.1 we introduce the mathematical formalism of the cosmological redshift drift, and then we give the details of the mock data sets we use for our predictions. We find it convenient to produce a SL data set, but also auxiliary SNe and BAO data. In Sec. 6.2, we explain our MCMC procedure which will eventually constrain the cosmological models we have chosen as reference. Finally, in Sec. 6.3, we present and discuss the outcomes of that statistical analysis, and then summarize and outline the main conclusions.

6.1 Cosmological Redshift drift

A preliminary straightforward calculation introduces the main observable quantity we are going to focus on, i.e. the cosmological redshift drift, (see for example [155] or [70]). In an homogeneous and isotropic universe with a Friedmann-Lemaître-Robertson-Walker metric Eq. (1.8), let us consider a source at rest emitting electromagnetic waves isotropically, without any (significant) peculiar velocity. Thus, the comoving distance of Eq. (2.11) between the source and an observer can be considered fixed and constant through time. If the source emits electromagnetic waves during time $(t_e, t_e + \delta t_e)$, and they are detected by the observer in the interval $(t_o, t_o + \delta t_o)$, where t_e is the emission time and t_o is the time they reach the observer, then the following relation is satisfied:

$$\int_{t_e}^{t_o} \frac{dt}{a(t)} = \int_{t_e+\delta t_e}^{t_o+\delta t_o} \frac{dt}{a(t)} \,, \tag{6.1}$$

provided the universe through which the waves travel is a spatially flat Friedmann-Lemaître-Robertson-Walker space-time. If the time intervals are small $(\delta t_e, \delta t_o \ll t_e, t_o)$, the above expression leads to the well known redshift relation between the emitted and the observed radiation:

$$\frac{\delta t_e}{a(t_e)} = \frac{\delta t_o}{a(t_o)} \quad \Rightarrow \quad \frac{\lambda_o}{\lambda_e} = \frac{a(t_o)}{a(t_e)} = 1 + z_e(t_o) \,, \tag{6.2}$$

where $z_e(t)$ is the redshift of the source as measured at a certain observation time t_o. Other waves can be emitted by the source δt_e time later, specifically, at time $t_e + \delta t_e$, and they will be observed at $t_o + \delta t_o$. In the case of these waves, it is straightforward to modify Eq. (6.2) regarding the new time periods and redshift. Thus, the observer can measure the difference between the redshifts observed at t_o and $t_o + \delta t_o$:

$$\Delta z_e = z_e(t_o + \delta t_o) - z_e(t_o) = \frac{a(t_o + \delta t_o)}{a(t_e + \delta t_e)} - \frac{a(t_o)}{a(t_e)} \,. \tag{6.3}$$

Within the $\delta t/t \ll 1$ approximation, the first ratio can be expanded to linear order:

$$\frac{a(t_o + \delta t_o)}{a(t_e + \delta t_e)} \simeq \frac{a(t_o)}{a(t_e)} + \frac{\dot{a}(t_o)\delta t_o}{a(t_e)} - \frac{a(t_o)\dot{a}(t_e)\delta t_e}{a(t_e)^2} \,. \tag{6.4}$$

Inserting Eq. (6.2) into the first order expansion in Eq. (6.4), an approximated expression for the redshift variation can be obtained:

$$\Delta z_e \simeq \left[\frac{\dot{a}(t_o) - \dot{a}(t_e)}{a(t_e)}\right] \delta t_o \,. \tag{6.5}$$

Under the assumption that the observation time is today, we normalize by letting the corresponding scale factor satisfy $a(t_o) = 1$; and then, using both the Friedmann equation and the known redshift relation Eq. (6.2), we can rewrite the above expression in terms

of the Hubble parameter $H(z) = \dot{a}(z)/a(z)$:

$$\Delta z_e = \delta t_o \left[H_0(1+z_e) - H(z_e) \right] \ , \tag{6.6}$$

with $H_0 = H(z_0)$ being the Hubble constant today. This redshift variation can be expressed as a spectroscopic velocity shift $\Delta v \equiv c\Delta z_e/(1+z_e)$, and using the dimensionless Hubble parameter $E(z) = H(z)/H_0$, we get the final expression

$$\Delta v = cH_0\delta t_o \left[1 - \frac{E(z_e)}{1+z_e} \right] \ . \tag{6.7}$$

6.1.1 Sandage-Loeb mock data set

In order to generate our SL observational mock data set in a fully model independent manner, we try to derive a Hubble function from a phenomenological distance modulus μ (Eq. (2.24)), in a fashion similar to [175]. We propose this observable because it is well measured by Type Ia Supernovae (SNe) and can be extended to high redshifts, even if with lower precision, by Gamma Ray Bursts (GRBs, Mayflower sample) [156]. We model this phenomenological distance modulus as

$$\mu_{fit}(z) = a + 5\log_{10}\left[F_{fit}(z;b,c,d,e) \right] \ , \tag{6.8}$$

where F_{fit} is an *ad* hoc proposed function (among many) mimicking the luminosity distance. This phenomenological function is then fitted using the SNe data set Union 2.1 [220] for the low-redshift regime, and the GRBs sample calibrated by the Padé Method [156] for the high-redshift one. Once μ_{fit} is fitted, other observational quantities relevant to our work can be easily obtained. For instance, the Hubble function can be derived recalling the relation of Eq. (2.24):

$$\mu(z) = 5\log_{10} d_L(z) + \mu_0 \ , \tag{6.9}$$

where, in the spatially flat universe we are considering, the dimensionless luminosity distance d_L of Eq. (2.19) is defined as

$$d_L(z) = (1+z)\int_0^z \frac{dz'}{E(z')} \ , \tag{6.10}$$

and μ_0 stores all the information related to the constants involved such as the speed of light c, the Hubble constant H_0, and the SNe absolute magnitude. By comparing both distance moduli, μ from Eq. (6.9) and μ_{fit} from Eq. (6.8), one can realize that the dimensionless luminosity distance $d_L(z)$ is equivalent to the function F_{fit}. Thus, the dimensionless Hubble function is

$$E_{fit}(z) = \left(\frac{d}{dz}\frac{F_{fit}(z;b,c,d,e)}{(1+z)} \right)^{-1} \ . \tag{6.11}$$

Once such phenomenological dimensionless Hubble parameter $E_{fit}(z)$ is obtained, we can "mimick" all the cosmological probes we need for our analysis, as they are all related to it. In this way, we can create cosmological-model-independent mock data sets, where the only intrinsic information we are using for E_{fit} is that it has to be able to fit present data (in this case, SNe and GRBs). Of course, some arbitrariness lies behind the choice of the phenomenological function F_{fit}; we have tried to use the most general type of functions possible, and we have selected the best one based on a simple best-fitting (minimum χ^2) criterium. The best performing function we have found is

$$F_{fit}(z;b,c,d,e) = \frac{z(1+b\log[1+z]^d)}{(1+c\log[1+z]^e)} \ , \tag{6.12}$$

where the values for the parameters are shown in Tab. 6.1. It can be seen in Fig. 6.1, in the top left panel, that this function fits the distance modulus points of the Union 2.1 [220] and Mayflower [156] data sets as much satisfactorily as a ΛCDM with *Planck* values, $\Omega_m = 0.3121$ (sixth column of Table 4 in [5]). In the top right panel, we also compare the expansion rate function $H(z)$ which can be derived from Eq. (6.12) with the same *Planck* ΛCDM and with data from cosmic chronometers [171]. In the bottom left panel, the comparison between angular diameter distance derived from Eq. (6.12) and the same *Planck* ΛCDM is done, with the data coming as comoving angular diameter distance from galaxy clustering (BAO+FS column of Table 7 in [9]) and physical angular diameter distance coming from quasar cross-correlation (Eq. (21) in [97]). Finally, in the bottom right panel, we can also appreciate that the difference between our model and the *Planck* ΛCDM is minimal for the case of the distance modulus ($\sim 0.1\%$), and small for both the Hubble function ($\sim 2.5\%$) and the angular diameter distance ($\sim 2\%$), all over the redshift range we cover with our mock data in our analysis.

Table 6.1: *Parameter values of F_{fit}.*

	Estimate	Standard Error
a	43.2025	0.146659
b	2.29876	1.60875
c	0.92048	0.969826
d	1.05317	0.62311
e	0.814751	0.922533

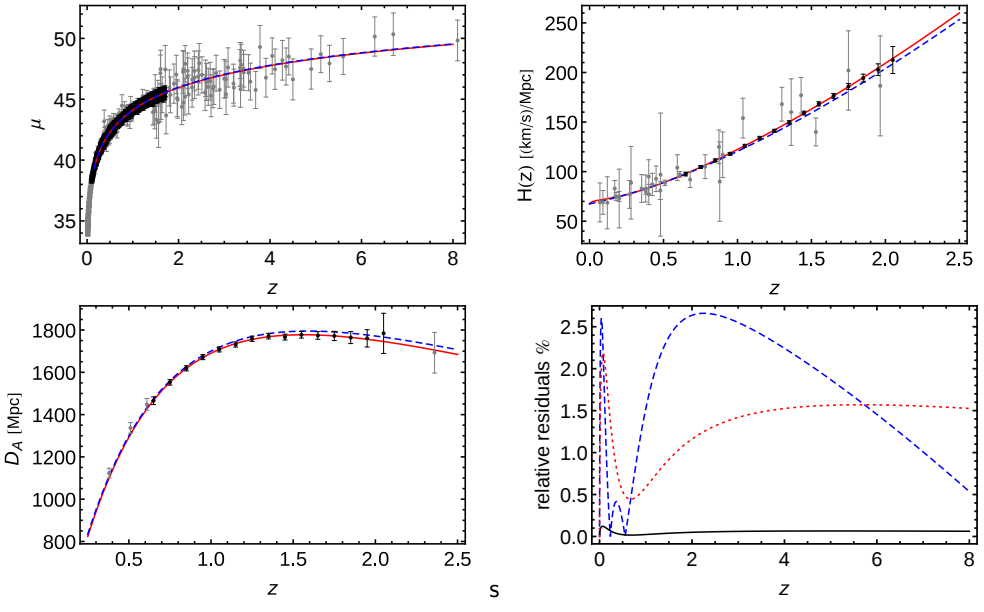

Figure 6.1: *Top left panel: Comparison between the selected phenomenological function* $F_{fit}(z; b, c, d, e)$ *given in Eq.* (6.12) *(solid red) with the Planck* Λ*CDM (dashed blue) described in the text. Grey dots and bars are distance modulus values and related errors for SNe Union and Mayflower GRBs samples, and black ones are for our generated SNe mock data. Top right panel: comparison between the* $H(z)$ *function derived from Eq.* (6.12) *(solid red) with that corresponding to the Planck* Λ*CDM (dashed blue) described in the text. Grey dots and bars are expansion rate values and related errors from cosmic chronometers and black ones our generated mock data. Bottom left panel: comparison of the* $D_A(z)$ *function derived from Eq.* (6.12) *(solid red) with that corresponding to the Planck* Λ*CDM (dashed blue) case described in the text. Grey dots and bars are angular diameter distances values and related errors from BOSS and SDSS, and black ones our generated mock data. Bottom right panel: relative residuals between our model and the Planck* Λ*CDM for the Hubble function (dashed blue), the distance modulus (solid black) and the angular diameter distance (dotted red).*

Once we have our $E_{fit}(z)$, we only need to specify a fiducial value for the Hubble constant to insert in Eq. (6.7), whose effect is only the rescaling of the velocity shift value. We fix the value of $H_0 = 67.51\,km/s/Mpc$ from the TT,TE,EE + lowP + lensing baseline model of *Planck* [5]. Then, for what concerns SL data, the points lie in the redshift range $2 < z < 5$, randomly distributed within the following bins: $2 < z < 3$ (13 points), $3 < z < 3.5$ (7 points), $3.5 < z < 4$ (4 points), $4 < z < 4.5$ (3 points) and $4.5 < z < 5$ (3 points). This way, we try to mimick the reduction of the number of data points while increasing the redshift as in [189].

According to Monte Carlo simulations carried out to eventually mimick results from CODEX [1, 155], the standard deviation on the measured spectroscopic velocity shift Δv can be estimated as

$$\sigma_{\Delta v} = 1.35 \frac{2370}{S/N} \sqrt{\frac{30}{N_{QSO}}} \left(\frac{5}{1 + z_{QSO}} \right)^{x} cm\, s^{-1} \,, \tag{6.13}$$

where x is 1.7 for $z \leq 4$, and 0.9 beyond that redshift, S/N is spectral signal-to-noise ratio of Ly-α, N_{QSO} is the number of observed quasars and z_{QSO} their redshift. The error for the mock data is given by assuming a fix number of integration time hours which yields a value of $S/N = 3000$ for the signal-to-noise ratio and $N_{QSO} = 30$ for the number of quasars observed [165]. We also introduce some noise to disperse the data points around the fiducial value derived from E_{fit}, using a Gaussian distribution centered on such values, and with a standard deviation corresponding to the expected error on the SL observation, $\sigma_{\Delta v}$, obtained by error propagation from the fitted parameters of the selected function of Eq. (6.12).

Note that the size of the observed cosmological redshift drift is proportional to the observation period, although the error does not depend on it as long as the dedicated integration time neither varies, i.e. the same signal-to-noise ratio is considered. Thus, once a data set for some given observational time Δt_A is created, any new mock data set with different observation period Δt_B can be easily calculated by

$$\Delta v_B = \frac{\Delta t_B}{\Delta t_A} \Delta v_A \,. \tag{6.14}$$

We use three observation periods of 24, 28 and 32 years, which are the most illustrative among the data sets tested. The resulting data sets for SL test can be seen on Fig. 6.2.

6.1.2 Auxiliary Mock Datasets

We include additional future mock data sets alongside the cosmological redshift drift data set so as to constrain models better. Basically, the reason why we introduce in the picture these other probes is our interest on studying and quantifying the relative performance of SL with respect to more standard and used probes, and our aim of finding out whether the cosmological redshift drift data have some degree of complementarity with them, thus

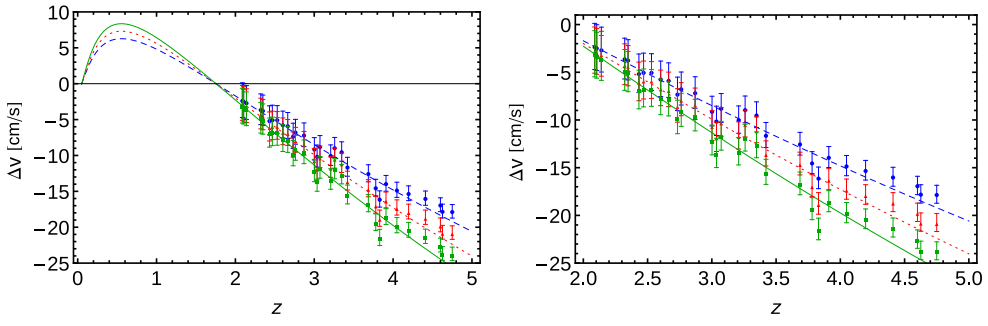

Figure 6.2: *Data sets for SL test based on $F_{fit}(z; b, c, d, e)$ of Eq.* (6.12) *for different observation periods: blue (circle and dashed line) for 24 years, red (triangle and dotted line) for 28 years and green (square and solid line) for 32 years.*

providing eventual tighter constraints. These auxiliary mock data sets are created from the same model independent function of Eq. (6.8).

W-First SNe

The first mock data set we produce is a SNe catalogue based on the *W-First* forecast [214], which includes 2725 SNe randomly picked in redshift bins of $\delta z = 0.1$ spread through a redshift range of $0.1 < z < 1.5$ according to the distribution given by [214].

Given that in the SNe case what one measures is the distance modulus μ, we can make direct use of the fitted function of Eq. (6.8) to generate the mock data points. As in the SL case, we also introduce some Gaussian noise to disperse the data points around the mean value.

To create the error bars for this catalogue and the dispersion for the Gaussian noise, we use the information given in [214]. The statistical errors they account for are the following: the photometric measurement error, $\sigma_{meas} = 0.8$; the intrinsic luminosity dispersion, $\sigma_{int} = 0.08$; and the gravitational lensing magnification, $\sigma_{lens} = 0.07$. Besides, they assume a systematic error $\sigma_{sys} = 0.01(1+z)/1.8$. Thus the total error per SNe is:

$$\sigma_{tot} = \sqrt{\sigma^2_{stat} + N_{\rm SN}\sigma^2_{sys}}\,, \tag{6.15}$$

where $\sigma_{stat} = \sqrt{\sigma^2_{meas} + \sigma^2_{int} + \sigma^2_{lens}}$ and $N_{\rm SN}$ is the number of SNe in the bin. The data set generated for the *W-First* SNe survey is shown on Fig. 6.1.

Euclid BAO

The second data set we consider is BAO. We choose the future *Euclid* survey [142] as the experiment to reproduce. The two quantities we consider are the angular diameter

distance $D_A(z)$ of Eq. (2.15), which can be expressed in the following way for the spatially flat case,

$$D_A(z) = \frac{c}{1+z}\int_0^z \frac{dz'}{H(z')}\,, \tag{6.16}$$

normalized by the sound horizon, $D_A(z)/r_s$; and the Hubble parameter times the sound horizon, $H(z)\,r_s$, where the value of $r_s = 144.71\ Mpc$, consistent with the previous H_0, is used according to [5].

Both the angular diameter distance and the Hubble parameter are reconstructed using again the function of Eq. (6.8). We have already discussed that the Hubble parameter can be inferred as in Eq. (6.11), once a value for H_0 is decided. Instead, in order to derive the angular diameter distance from the same Eq. (6.8), we use its definition and its relation with the luminosity distance $(1+z)^2 D_A = D_L$, thus to obtain

$$D_A(z) = \frac{c}{H_0}\frac{F_{fit}(z;b,c,d,e)}{(1+z)^2}\,. \tag{6.17}$$

The redshift values of the data set are taken from [96], and they specifically are the central redshfits of 15 bins with $\delta z = 0.1$ width, spread from $z = 0.5$ to $z = 2.1$. The error in each redshift value for both D_A and H_0 is build from the percentage error given also in [96]. Finally, we introduce some Gaussian noise using the error from each bin as dispersion when generating the points $D_A(z)/r_s$ and $H(z)\,r_s$. The resulting data sets can be seen at Fig. 6.1 before normalizing the observables by the comoving sound horizon r_s.

6.2 Mock data constrains

Within the Bayesian framework, we wish to find out how SL constrains the probability distribution function of some cosmological parameters. For that purpose, we need the posterior distribution, or equivalently the likelihood, which can be straightforwardly computed with MCMC sampling while minimizing the χ^2 function as shown in Chap. 3. The knowledge of the posterior probability gives a better and more complete information about the parameters, including the full correlation among them.

Thus, once we have the mock data sets, we build the χ^2 function for each observable and, once all contributions are summed up, we minimize the total χ^2 in order to perform our statistical analysis. The χ^2 contribution for the spectroscopic velocity shift is simply

$$\chi^2_{SL} = \sum_i \left(\frac{\Delta v_i^{theo} - \Delta v_i^{mock}}{\sigma_{\Delta v_i}}\right)^2\,, \tag{6.18}$$

where $\Delta v_i^{theo} = \Delta v(z_i)$ follows from Eq. (6.7), while errors $\sigma_{\Delta v_i}$ are given by Eq. (6.13). The errors are arranged into a diagonal covariance matrix. Depending on whether the SL surveys will use overlapping redshift bins or not, the error could be more realistically

given by a non-diagonal covariance matrix. As we lack such information, we adopt the optimistic diagonal covariance matrix assumption, always keeping in mind that it could lead to a general underestimation of the global errors on the cosmological parameters. The period of observation Δt_o, which were specified before, changes depending on the mock SL survey tested.

In the case of the χ^2 contribution of SNe, the χ^2 reads:

$$\chi^2_{\rm SN} = \sum_i \frac{(\mu(z_i) - \mu_i^{mock})^2}{\sigma^2_{\mu_i}} \,, \tag{6.19}$$

where the error is given by Eq. (6.15). We can marginalize χ^2 over the parameter μ_0, similarly as in Sec. 3.1.3, by expanding the χ^2 in Eq. (6.19) with respect to μ_0 as

$$\chi^2_{\rm SN} = A - 2\mu_0 B + \mu_0^2 C \,, \tag{6.20}$$

where

$$\begin{aligned} A &= \sum_i \frac{(\tilde{\mu}(z_i) - \mu_i^{mock})^2}{\sigma^2_{\mu_i}} \,, \\ B &= \sum_i \frac{\tilde{\mu}(z_i) - \mu_i^{mock}}{\sigma^2_{\mu_i}} \,, \\ C &= \sum_i \frac{1}{\sigma^2_{\mu_i}} \,. \end{aligned} \tag{6.21}$$

Then, integrating μ_0 out of the likelihood $\mathcal{L} = e^{-\frac{\chi^2_{\rm SN}}{2}}$ we can retrieve

$$\tilde{\chi}^2_{\rm SN} = A - \frac{B^2}{C} + \ln\frac{C}{2\pi} \,, \tag{6.22}$$

where $\tilde{\chi}^2_{\rm SN}$ has now no dependence on the μ_0 parameter. This marginalization differs from the one shown in Sec. 3.1.3 and previous chapters because in this case we are using a diagonal covariance matrix. It is not possible to forecast out-of-diagonal terms, which can lead to underestimated errors on cosmological parameters.

With BAO we have two correlated measurements to contribute to the total χ^2; these are $H(z)\, r_s$ and $D_A(z)/r_s$. In this case, the comoving sound horizon r_s of Eq. (2.39) has an equivalent expression, which is evaluated at photon-decoupling epoch redshift given by the fitting formula [123] of Eq. (2.35). The BAO contribution is calculated independently for each redshift, $\chi^2_{BAO} = \sum_i \chi^2_{BAO_i}$, but taking into account the correlation of the quantities, each term at each redshift has the same form of Eq. (4.21),

$$\chi^2_{BAO_i} = \frac{1}{1-r^2}\left(\frac{\tilde{H}_i^2}{\sigma^2_{\tilde{H}_i}} + \frac{\tilde{D}_i^2}{\sigma^2_{\tilde{D}_i}} - 2r\frac{\tilde{H}_i}{\sigma_{\tilde{H}_i}}\frac{\tilde{D}_i}{\sigma_{\tilde{D}_i}}\right) \,, \tag{6.23}$$

where $\tilde{H}_i$ and $\tilde{D}_i$ are the differences between the model predicted and the mock generated measurements:

$$\tilde{H}_i = H(z_i)\, r_s(z_*) - (H\, r_s)_i^{mock}, \tag{6.24}$$

$$\tilde{D}_i = \frac{D_A(z_i)}{r_s(z_*)} - \left(\frac{D_A}{r_s}\right)_i^{mock}. \tag{6.25}$$

The correlation between the two magnitudes $H\, r_s$ and D_A/r_s in each redshift is fixed as $r = 0.4$ [209]. Since CMB data are not used, SNe data are marginalized over the parameter H_0, and BAO data do not give information about it (because $D_A/r_s(z_*)$ and $H\, r_s(z_*)$ do not basically depend on it), the parameters H_0 and the combination $\Omega_b h^2$ cannot be well constrained. Thus, we also include a Gaussian prior for H_0 and $\Omega_b h^2$, with $H_0^{Planck} = 67.51 \pm 0.64$ and for $\Omega_b h^2_{Planck} = 0.02226 \pm 0.00016$ both derived from *Planck* [5].

The minimization of the χ^2 function was performed using the MCMC method [61, 148, 226], with a Wolfram Mathematica self-developed code based on the Metropolis-Hastings algorithm shown in Sec. 3.2. In order to see the contribution of each mock data set to the total χ^2, we have also run chains for each data set separately. In this way, we compare the cosmological redshift drift data with those from the other future surveys, and find out whether it will be useful and up to what extent. Moreover, for a round analysis regarding the viability of the Sandage-Loeb test and the performance of the future (mock) surveys, several dark energy scenarios are put to the test.

6.2.1 ΛCDM

The first model we test is the extremely well-known ΛCDM model [57, 199], which has no degree of freedom in the dark energy equation of state and whose dimensionless Hubble parameter is given by

$$E^2_{\Lambda CDM}(a) = \Omega_m a^{-3} + \Omega_r a^{-4} + \Omega_\Lambda\,, \tag{6.26}$$

taking $\Omega_\Lambda = 1 - \Omega_m - \Omega_r$ with [238]

$$\Omega_r = \Omega_m \left[1 + 2.5 \times 10^4 h^2 \Omega_m (T_{CMB}/2.7)^{-4}\right]^{-1} \tag{6.27}$$

and using $T_{CMB} = 2.7255\, K$ [95]. We enforce $0 < \Omega_m < 1$, and $0 < \Omega_b < \Omega_m < 1$ as physical priors, and we do the same for all the rest of models analysed in this chapter. The results of the Bayesian analysis for the ΛCDM model can be seen on Tab. 6.2 and Fig. 6.4.

6.2.2 Quiessence

The second model tested is quiessence [137, 187], with a single degree of freedom in the dark energy equation of state parameter (i.e. no redshift dependence). Its dimensionless Hubble parameter is given by

$$E_Q^2(a) = \Omega_m a^{-3} + \Omega_r a^{-4} + \Omega_\Lambda a^{-3(1+w)}, \tag{6.28}$$

where all the parameters except w are built like in the ΛCDM model and have the same priors. The parameter w has the prior $-5 < w < 0$. This range was chosen after having verified that expanding it further has no influence on results. Tab. 6.3 and Fig. 6.5 show the results for quiessence model.

6.2.3 Slow-Roll Dark Energy

We consider another one-parameter dark energy model, coming from the slow-roll dark energy scenario described in [212]. Its dimensionless Hubble parameter, taking into account a radiation component [4, 20] is given by

$$E_{SR}^2(a) = \Omega_m a^{-3} + \Omega_r a^{-4} + \Omega_\Lambda \left(\frac{a^{-3}}{\Omega_m a^{-3} + \Omega_r a^{-4} + \Omega_\Lambda} \right)^{(\delta w/\Omega_\Lambda)} . \tag{6.29}$$

For δw we impose a prior of the same width as that of the parameter w of quiessence, but as δw is supposed to have its mean value at $\delta w = 0$, we design its prior accordingly. Thus, we take $-2.5 < \delta w < 2.5$. The results for the the slow-roll dark energy model can be found on Tab. 6.4 and Fig. 6.6.

6.2.4 CPL

We are also interested in testing models of dark energy whose equation of state parameter w has more than one degree of freedom. As our first two-parameter dark energy model, we take the CPL model [59, 154], its dimensionless Hubble parameter being

$$E_{CPL}^2(a) = \Omega_m a^{-3} + \Omega_r a^{-4} + \Omega_\Lambda a^{-3(1+w_0+w_a)} e^{-3w_a(1-a)} , \tag{6.30}$$

where all the terms except w_0 and w_a are built like in previous models and with the same priors. The parameter w_0 has the same prior as w does in quiessence; and we take $-5 < w_a < 5$ for the second parameter. We demand in this case $w_a + w_0 < 0$ in order to have an equation of state for the DE component which is negative in the asymptotic past. Tab. 6.5 and Fig. 6.7 give the results of our Bayesian analysis for the CPL model.

6.2.5 Lazkoz-Sendra pivotal Dark Energy

We consider another model with two parameters for the equation of state for DE [208], which can be understood easily as a perturbative departure from ΛCDM up to second order in redshift. Even though it is a different parametrization as compared to CPL, it can be also expressed in terms of the parameters w_0 and w_a with the same interpretation: w_0 is the value of equation of state of the dark energy at present, whereas $w_0 + w_a$ is its value in the asymptotic past. Specifically, the Lazkoz-Sendra pivotal dark energy parametrization has the following dimensionless Hubble parameter:

$$\begin{aligned} E^2_{\rm LS}(a) &= \Omega_m a^{-3} + \Omega_r a^{-4} + \Omega_\Lambda X(a)\ , \\ X(a) &= a^{-3(1+w_0+w_a)} e^{\frac{3}{4}(1-a)[1+w_0-5w_a+a(w_a-w_0-1)]} \end{aligned} \tag{6.31}$$

where all the relative densities Ω_i are built like in the CPL case, having all the parameters also the same priors as in CPL, including w_0 and w_a. In the case of the Lazkoz-Sendra (LS) model, the results of the Bayesian analysis are shown in Tab. 6.6 and Fig. 6.8.

6.3 Take-home lesson about forecast with Sandage-Loeb data

In the summary tables for each model, we present the minimum value of χ^2, the constraints for all the free parameters and the reduced χ^2_{red}. As explained in previous section, the χ^2-minimization is done using different combinations of data sets. In the tables we first show the results from using BAO and SNe separately and those from joining both; then, we move on to present the results from SL only, and then, finally, those for the total SNe+BAO+SL combination. When using SL data, each data set with different observation years is treated separately. In this way, the performance of the cosmological redshift drift data sets can be clearly analysed. For each model we also show the confidence contours for the most interesting cosmological parameters. Each MCMC round is tested for statistical convergence using the method explained in [82] and described in Sec. 3.2.1.

In the ΛCDM scenario we find that the cosmological redshift drift data provide remarkably good constraints on Ω_m: when those data are used alone we get standard deviations on Ω_m which are $2-3$ times smaller that those from the SNe+BAO combination. Considering the broad priors taken for Ω_m in all cases, and the negligible correlation between the Hubble constant h and Ω_m [1], we conclude that the result for the matter density Ω_m is not influenced by any prior and is solely given by the data.

Indeed, the SL data sets always do better in constraining Ω_m than the SNe data, and depending on the model and on the years of observation, even better than the BAO data set. Once we combine the SL data set with the other two, the cosmological redshift

[1] As the major axis of the contours are typically aligned with the axes of each parameters in the parameter space.

drift is still helpful, even though the BAO+SNe data set already improves greatly the constrains in the parameter space. In general, it is clear that the cosmological redshift drift data helps considerably to constrain the parameter Ω_m in all the models.

Regarding the dark energy parameters, we can observe that for most of the cases, the 24 years of observation for SL is not enough to constrain them properly, as it can be clearly seen for example from the contours of the parameters w_0 and w_a in Figs. 6.7 - 6.8. With 28 years SL data, the 1σ regions improve noticeable, and with 32 years of observation both 1σ and 2σ regions are well constrained for all the DE parameters. The best example is in Fig. 6.8, as stated, but similar behaviour can be appreciated in the rest of the models. Besides, it is clear that increasing the observation years improves the overall constraining ability of the cosmological redshift drift data sets. It is worth to note that in all these cases, the contours of the SL data set are almost perpendicular to the contours of the SNe and BAO data sets, thus showing a great complementarity between SL and the rest of the data sets [67], as for example in the $\Omega_m - w$ plane for the quiessence model, Fig. 6.5, or for the dynamical dark energy models, Figs. 6.6 - 6.7 - 6.8. This is very important, because it means that even the cosmological redshift drift data set with the lowest observation period, noticeably contributes to improved dark energy insights when used as cosmological probe together with other kind of observations.

However, if one focuses on the w_0 and w_a parameters, two things can be noted: first, that the best fit for the SNe+BAO case is completely different from the values derived from SNe and BAO only analysis (this is more evident for w_a than w_0); second, the errors on the w_0 and w_a parameters slightly increase when adding cosmological redshift drift data to the SNe+BAO data. Both trends might have an explanation. For what concerns the first one, if we look at the left panel of Fig. 6.3 (this is for the CPL case, but it holds true for the LS model as well), we can see how unsatisfactorily the SNe and BAO contours overlap: the borders of the 1σ confidence levels show a small overlap in a region which is far from the best fit expected for each of them when considered separately. This reduces the constraints on the parameters in a considerable way and shifts the best fit estimations (not only in w_a, but also on Ω_m). But note also that this behavior is somehow expected and might be counter-productive in the future, as explained in [93]. Anyway, we must also remember we are working with mock data, not real ones, and the potential future goodness of the joint use of SNe and BAO at the present, and maybe in the near future, is not put at stake. Moreover, we have to remember that in order to gain more insights into a dynamical dark energy model, we need to improve the number and the quality of data at high redshift; that is the reason behind pushing SNe observations to higher redshifts [201], for example, or employing BAO data at $z \sim 2$. But the strongest hints about the dynamical nature of the dark energy might come from data like SL, which are able to cover a larger and deeper redshift range. And the second issue discussed above should be exactly connected to this: if we check again the right panel of Fig. 6.3, we can see how the SL data set alone, which should be more sensitive to a dynamical dark energy, determines a consistent shift in the parameter w_0 with respect to the SNe+BAO case but with smaller uncertainty with respect to both SNe and BAO data separately, which eventually ends in a slightly large error for this parameter for the total SNe+BAO+SL

sample.

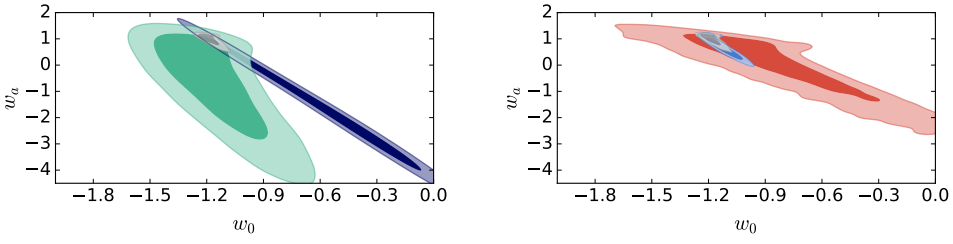

Figure 6.3: *Contours in the $w_0 - w_a$ plane for CPL; solid contours are for 1σ regions and clear contours are for 2σ regions. Left panel: purple is for the BAO data; green for SNe and grey for SNe+BAO. Right panel: red is for 32 years SL data; grey for SNe+BAO; blue for SNe+BAO+SL.*

In the case of models with a single DE parameter, that is, whose equation of state is fixed during time, high redshift SL data are also helpful. In the extreme case when SL data are added to the SNe+BAO data set, even the SL data with lowest observational period help constrain the single parameter of DE. However, it is also remarkable how every data set, separately, constrains the single DE parameter to a different value. Taking into account that the redshift range of each data set is quite different, the fact that separately they measure a different value for the parameter could be an evidence for a time evolution in the equation of state of DE. This is a clear example of another application for the SL observation, where its high redshift data could easily test the time evolution of the equation of state of DE once compared to the results of other data sets coming from different sources.

A lot of what has been stated above can be easily inferred upon closer examination of the various contours plots. However, these plots are more useful for analyzing the correlation between different parameters. As stated previously, in most of the contour plots, a different correlation angle can be seen for the cosmological redshift drift data comparing the other data sets. Thus, it clearly emerges that SL data sets will be of utmost importance in breaking degeneracies among cosmological parameters. Besides, considering the high redshift data that will be available thanks to cosmological redshift drift, we conclude that it can be a cosmic observable much worth to consider.

6.3.1 Detailed Results

Results for the ΛCDM model

Table 6.2: *Parameter results of the ΛCDM model.*

Data Set	h	Ω_m	Ω_b	χ^2_{min}	χ^2_{red}
BAO	$0.689^{+0.002}_{-0.002}$	$0.335^{+0.008}_{-0.008}$	$0.0467^{+0.0004}_{-0.0004}$	9.47	0.861
SNe	$0.675^{+0.006}_{-0.007}$	$0.301^{+0.008}_{-0.008}$		1387.41	0.510
SNe+BAO	$0.689^{+0.002}_{-0.002}$	$0.324^{+0.006}_{-0.006}$	$0.0472^{+0.0004}_{-0.0004}$	1402.07	0.513
SL(24y)	$0.674^{+0.006}_{-0.006}$	$0.328^{+0.003}_{-0.003}$		14.51	0.538
SNe+BAO+SL(24y)	$0.689^{+0.002}_{-0.002}$	$0.324^{+0.003}_{-0.002}$	$0.0467^{+0.0004}_{-0.0004}$	1417.82	0.513
SL(28y)	$0.673^{+0.006}_{-0.006}$	$0.328^{+0.003}_{-0.003}$		19.73	0.731
SNe+BAO+SL(28y)	$0.689^{+0.002}_{-0.002}$	$0.325^{+0.002}_{-0.002}$	$0.0467^{+0.0004}_{-0.0004}$	1423.49	0.515
SL(32y)	$0.673^{+0.006}_{-0.006}$	$0.328^{+0.002}_{-0.002}$		25.75	0.954
SNe+BAO+SL(32y)	$0.689^{+0.002}_{-0.002}$	$0.325^{+0.002}_{-0.002}$	$0.0468^{+0.0004}_{-0.0004}$	1430.03	0.518

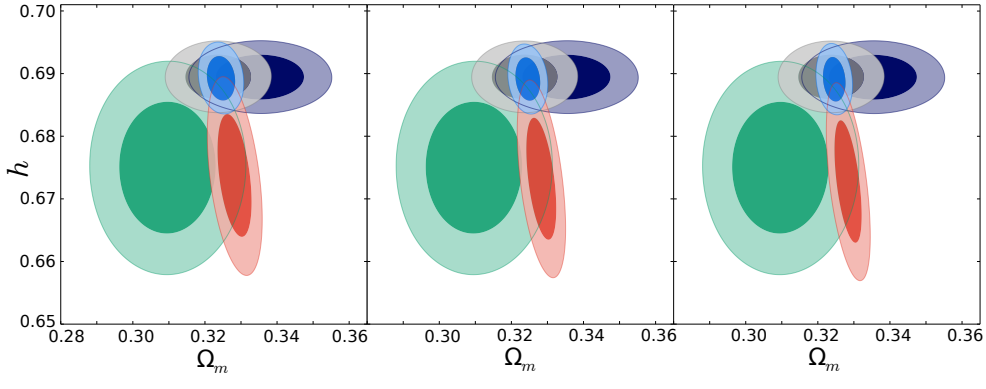

Figure 6.4: *ΛCDM model; solid contours limit 1σ regions and clear contours 2σ regions. Purple for the BAO, green for SNe and red for SL data set, grey for SNe+BAO and blue SL+BAO+SNe. First set (left) for 24 years, second (middle) for 28 and third (right) for 32 years.*

Results for the Quiessence model

Table 6.3: *Parameter results of the Quiessence model.*

Data Set	h	Ω_m	Ω_b	w	χ^2_{min}	χ^2_{red}
BAO	$0.677^{+0.006}_{-0.006}$	$0.336^{+0.008}_{-0.008}$	$0.0485^{+0.0010}_{-0.0009}$	$-0.948^{+0.024}_{-0.025}$	5.10	0.510
SNe	$0.675^{+0.006}_{-0.007}$	$0.341^{+0.013}_{-0.015}$		$-1.244^{+0.123}_{-0.122}$	1383.13	0.509
SNe+BAO	$0.686^{+0.006}_{-0.006}$	$0.323^{+0.006}_{-0.006}$	$0.0472^{+0.0008}_{-0.0008}$	$-0.987^{+0.022}_{-0.023}$	1401.74	0.513
SL(24y)	$0.674^{+0.006}_{-0.007}$	$0.323^{+0.011}_{-0.011}$		$-0.888^{+0.141}_{-0.660}$	12.73	0.490
SNe+BAO+SL(24y)	$0.685^{+0.005}_{-0.005}$	$0.324^{+0.003}_{-0.002}$	$0.0474^{+0.0008}_{-0.0008}$	$-0.982^{+0.020}_{-0.021}$	1417.07	0.513
SL(28y)	$0.674^{+0.006}_{-0.007}$	$0.321^{+0.009}_{-0.009}$		$-0.845^{+0.102}_{-0.176}$	17.32	0.666
SNe+BAO+SL(28y)	$0.684^{+0.005}_{-0.005}$	$0.325^{+0.002}_{-0.002}$	$0.0475^{+0.0008}_{-0.0008}$	$-0.979^{+0.020}_{-0.021}$	1422.49	0.515
SL(32y)	$0.674^{+0.007}_{-0.006}$	$0.320^{+0.007}_{-0.008}$		$-0.830^{+0.084}_{-0.119}$	22.62	0.870
SNe+BAO+SL(32y)	$0.684^{+0.005}_{-0.005}$	$0.325^{+0.002}_{-0.002}$	$0.0476^{+0.0008}_{-0.0008}$	$-0.977^{+0.020}_{-0.020}$	1428.75	0.517

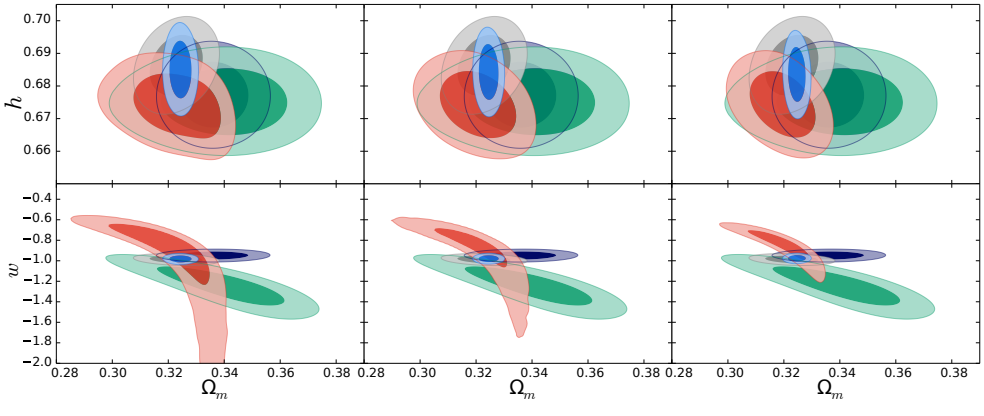

Figure 6.5: *Quiessence model; solid contours limit 1σ regions and clear contours 2σ regions. Purple for the BAO, green for SNe and red for SL data set, grey for SNe+BAO and blue SL+BAO+SNe. First set (left) for 24 years, second (middle) for 28 and third (right) for 32 years.*

Results for the Slow-Roll model

Table 6.4: *Parameter results of the Slow-Roll model.*

Data Set	h	Ω_m	Ω_b	δw	χ^2_{min}	χ^2_{red}
BAO	$0.678^{+0.006}_{-0.006}$	$0.341^{+0.009}_{-0.008}$	$0.0485^{+0.0010}_{-0.0009}$	$0.074^{+0.036}_{-0.035}$	5.20	0.520
SNe	$0.675^{+0.006}_{-0.006}$	$0.330^{+0.010}_{-0.012}$		$-0.260^{+0.128}_{-0.138}$	1383.10	0.509
SNe+BAO	$0.688^{+0.005}_{-0.006}$	$0.324^{+0.006}_{-0.006}$	$0.0468^{+0.0008}_{-0.0008}$	$0.005^{+0.030}_{-0.030}$	1402.05	0.513
SL(24y)	$0.674^{+0.006}_{-0.006}$	$0.324^{+0.007}_{-0.007}$		$0.231^{+0.252}_{-0.539}$	13.12	0.504
SNe+BAO+SL(24y)	$0.687^{+0.005}_{-0.005}$	$0.325^{+0.002}_{-0.002}$	$0.0471^{+0.0008}_{-0.0008}$	$0.014^{+0.028}_{-0.029}$	1417.62	0.513
SL(28y)	$0.674^{+0.006}_{-0.006}$	$0.323^{+0.006}_{-0.006}$		$0.282^{+0.199}_{-0.330}$	17.85	0.686
SNe+BAO+SL(28y)	$0.686^{+0.005}_{-0.005}$	$0.325^{+0.002}_{-0.002}$	$0.0472^{+0.0008}_{-0.0008}$	$0.017^{+0.028}_{-0.027}$	1423.21	0.515
SL(32y)	$0.674^{+0.006}_{-0.006}$	$0.323^{+0.005}_{-0.005}$		$0.306^{+0.171}_{-0.254}$	23.31	0.897
SNe+BAO+SL(32y)	$0.686^{+0.005}_{-0.005}$	$0.325^{+0.002}_{-0.002}$	$0.0473^{+0.0008}_{-0.0007}$	$0.021^{+0.029}_{-0.029}$	1429.59	0.518

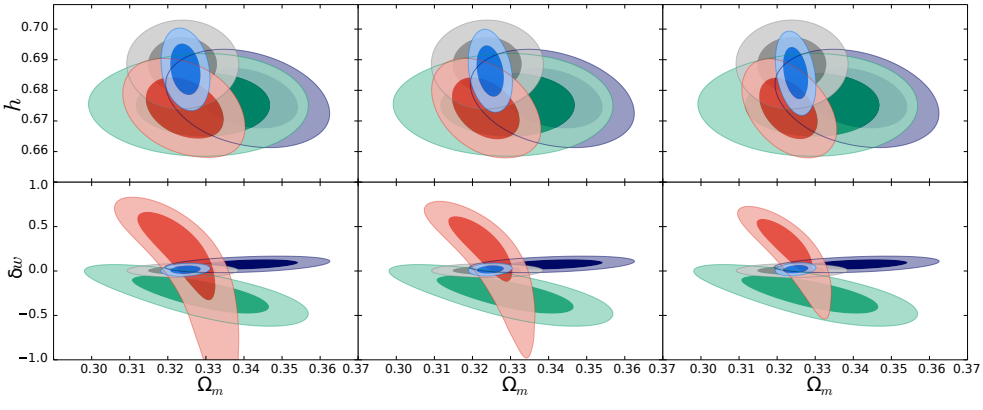

Figure 6.6: *Slow-Roll model; solid contours limit 1σ regions and clear contours 2σ regions. Purple for the BAO, green for SNe and red for SL data set, grey for SNe+BAO and blue SL+BAO+SNe. First set (left) for 24 years, second (middle) for 28 and third (right) for 32 years.*

Results for the CPL model

Table 6.5: *Parameter results of the CPL model.*

Data Set	h	Ω_m	Ω_b	w_0	w_a	χ^2_{min}	χ^2_{red}
BAO	$0.677^{+0.006}_{-0.007}$	$0.395^{+0.035}_{-0.075}$	$0.0486^{+0.0010}_{-0.0010}$	$-0.558^{+0.311}_{-0.467}$	$-1.722^{+2.035}_{-1.457}$	3.37	0.374
SNe	$0.675^{+0.006}_{-0.006}$	$0.356^{+0.030}_{-0.038}$		$-1.165^{+0.203}_{-0.182}$	$-0.555^{+1.232}_{-1.708}$	1383.07	0.509
SNe+BAO	$0.678^{+0.006}_{-0.006}$	$0.281^{+0.011}_{-0.011}$	$0.0484^{+0.0010}_{-0.0009}$	$-1.187^{+0.040}_{-0.032}$	$1.022^{+0.119}_{-0.195}$	1386.45	0.508
SL(24y)	$0.674^{+0.007}_{-0.006}$	$0.328^{+0.008}_{-0.017}$		$-1.026^{+0.498}_{-1.518}$	$-0.001^{+1.044}_{-1.584}$	12.19	0.488
SNe+BAO+SL(24y)	$0.684^{+0.006}_{-0.006}$	$0.314^{+0.006}_{-0.008}$	$0.0476^{+0.0009}_{-0.0008}$	$-1.117^{+0.066}_{-0.066}$	$0.602^{+0.286}_{-0.286}$	1412.27	0.512
SL(28y)	$0.674^{+0.006}_{-0.006}$	$0.324^{+0.010}_{-0.017}$		$-0.937^{+0.423}_{-0.627}$	$-0.021^{+0.869}_{-1.541}$	16.56	0.662
SNe+BAO+SL(28y)	$0.683^{+0.006}_{-0.006}$	$0.315^{+0.006}_{-0.008}$	$0.0476^{+0.0009}_{-0.0008}$	$-1.113^{+0.066}_{-0.068}$	$0.590^{+0.293}_{-0.276}$	1417.52	0.513
SL(32y)	$0.674^{+0.006}_{-0.006}$	$0.319^{+0.010}_{-0.019}$		$-0.895^{+0.372}_{-0.256}$	$0.240^{+0.637}_{-1.147}$	21.65	0.866
SNe+BAO+SL(32y)	$0.683^{+0.006}_{-0.006}$	$0.315^{+0.006}_{-0.008}$	$0.0477^{+0.0009}_{-0.0008}$	$-1.120^{+0.066}_{-0.062}$	$0.628^{+0.297}_{-0.278}$	1423.36	0.516

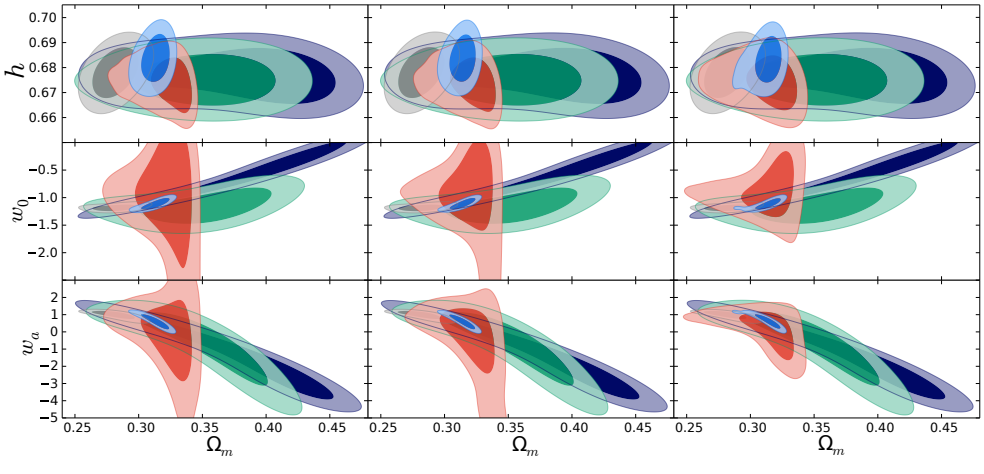

Figure 6.7: *CPL model; solid contours limit 1σ regions and clear contours 2σ regions. Purple for the BAO, green for SNe and red for SL data set, grey for SNe+BAO and blue SL+BAO+SNe. First set (left) for 24 years, second (middle) for 28 and third (right) for 32 years.*

Results for the Lazkoz-Sendra pivotal Dark Energy model

Table 6.6: *Parameter results of the Lazkoz-Sendra pivotal model.*

Data Set	h	Ω_m	Ω_b	w_0	w_a	χ^2_{min}	χ^2_{red}
BAO	$0.677^{+0.006}_{-0.006}$	$0.391^{+0.034}_{-0.065}$	$0.0485^{+0.0009}_{-0.0009}$	$-0.661^{+0.244}_{-0.333}$	$-2.114^{+2.401}_{-1.820}$	3.33	0.370
SNe	$0.675^{+0.006}_{-0.007}$	$0.361^{+0.023}_{-0.031}$		$-1.170^{+0.150}_{-0.143}$	$-1.063^{+1.565}_{-2.004}$	1383.13	0.509
SNe+BAO	$0.680^{+0.006}_{-0.006}$	$0.295^{+0.009}_{-0.008}$	$0.0481^{+0.0009}_{-0.0009}$	$-1.093^{+0.028}_{-0.025}$	$0.934^{+0.112}_{-0.196}$	1388.46	0.508
SL(24y)	$0.673^{+0.007}_{-0.006}$	$0.331^{+0.005}_{-0.014}$		$-1.056^{+0.510}_{-2.390}$	$-0.616^{+1.416}_{-2.186}$	12.53	0.501
SNe+BAO+SL(24y)	$0.683^{+0.006}_{-0.006}$	$0.311^{+0.006}_{-0.006}$	$0.0477^{+0.0008}_{-0.0008}$	$-1.088^{+0.037}_{-0.029}$	$0.826^{+0.185}_{-0.278}$	1408.54	0.510
SL(28y)	$0.674^{+0.007}_{-0.007}$	$0.325^{+0.009}_{-0.015}$		$-0.884^{+0.349}_{-0.449}$	$-0.173^{+0.917}_{-1.775}$	16.77	0.671
SNe+BAO+SL(28y)	$0.682^{+0.005}_{-0.006}$	$0.312^{+0.006}_{-0.006}$	$0.0477^{+0.0009}_{-0.0008}$	$-1.089^{+0.037}_{-0.029}$	$0.839^{+0.177}_{-0.279}$	1413.75	0.512
SL(32y)	$0.674^{+0.006}_{-0.006}$	$0.322^{+0.009}_{-0.015}$		$-0.848^{+0.335}_{-0.227}$	$-0.080^{+0.815}_{-1.498}$	21.93	0.877
SNe+BAO+SL(32y)	$0.682^{+0.005}_{-0.005}$	$0.312^{+0.005}_{-0.006}$	$0.0479^{+0.0008}_{-0.0008}$	$-1.087^{+0.038}_{-0.028}$	$0.835^{+0.177}_{-0.274}$	1419.53	0.514

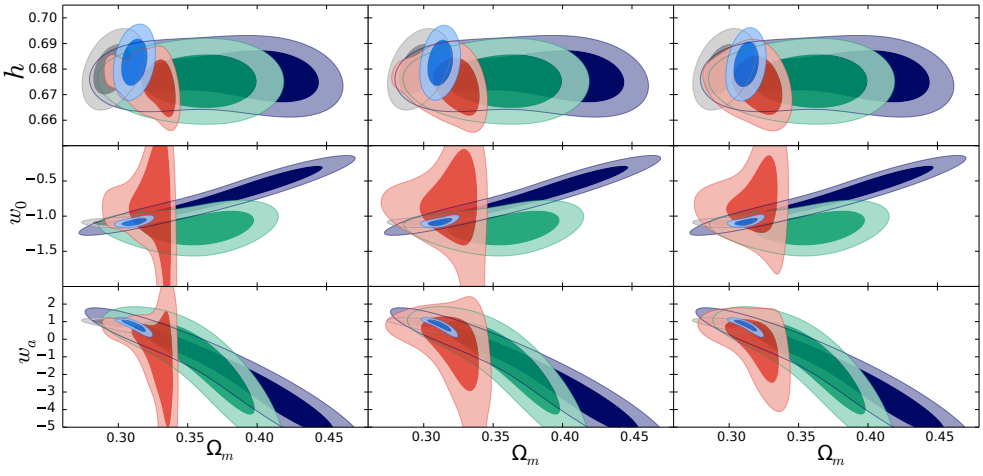

Figure 6.8: *Lazkoz-Sendra pivotal model; solid contours limit 1σ regions and clear contours 2σ regions. Purple for the BAO, green for SNe and red for SL data set, grey for SNe+BAO and blue SL+BAO+SNe. First set (left) for 24 years, second (middle) for 28 and third (right) for 32 years.*

PART IV

Conclusions

7 General Conclusions

Despite the quite reasonable claim and evidence of having entered an era of "precision cosmology", the nature of the dark sector of our Universe is still far from having been clarified. In this thesis we have tried to take some small further steps in clarifying the global picture by testing theoretical proposal with observational data, or by exploring the possibility to use novel observational probes to cast some light on the dark sector.

We have explored the possibility that dark matter and dark energy might be two sides of the same coin: despite the fact they are apparently so different in their nature, we could try to simplify the picture by assuming a single new exotic fluid which, given the right conditions, might behave as both dark matter and as dark energy.

In Chap. 4, we have introduced a phenomenological unified dark matter-energy (UDM) model which exhibits the possibility of a fast transition from a dark matter behavior to a late ΛCDM scenario. In this way, a single fluid could explain both the present dark energy-dominated accelerated expansion of the Universe and the early dark matter-dominated era. We have compared this UDM model with other more standard scenarios (where dark matter and dark energy are two separate fluids) in order to check exactly not only its consistence with data, but also its degree of reliability and its statistical preference (or not) with respect to such standard cases. In a few words, we have tried to answer the following question: even if the unification of dark sector is theoretically possible, is it really achievable and carved in the data?

As standard scenarios, as well as the consensus ΛCDM model, we have also considered the quiessence model. All models have then been fitted to cosmological data coming mainly from geometrical probes, i.e. Type Ia Supernovae, Baryon Acoustic Oscillations and shift parameters from Cosmic Microwave Background. In order to check the statistical reliability of each model against the others, we have relied on a Bayesian Evidence analysis, which has shown that the UDM model might have a slightly better statistical preference than the rest of the models we have addressed. Nevertheless, all models display a very small evidence difference as compared to ΛCDM, and thus none of the models can be discarded.

The transition is parametrized by the value of the scale factor at which it happens, a_t, along with its rapidity, β. The value of those parameters is clearly to be constrained by the cosmological background data. Our estimations indicate it might have happened in the past around the scale factor $a_t \approxeq 0.17 - 0.18$ (redshift $z_t \approxeq 4.55 - 4.88$), and it was fast according to the rapidity parameter, with $\beta \sim 550$ and $\beta \sim 770$ for each UDM model. Therefore, the cosmological background data favors fast transitions over slow ones, a feature which makes the UDM model easily distinguishable from the ΛCDM, even though the late evolution of both models are similar. In this way, the UDM model could be interpreted as an early-time deviation or correction of the ΛCDM model, thus modifying the expansion history of the universe before the transition.

In Chap. 5, we have considered another UDM model which is not phenomenological, but it is supported by a proper scalar field representation. This single scalar field could behave both as dark matter and dark energy, with a transition between both behaviors which can occur rapidly. We have compared this UDM model with similar cosmological background data as in the previous case, and have performed again a Bayesian analysis. The results have shown that the UDM model of this Chap. 5 obtains a milder result that the previous phenomenological UDM model of Chap. 4. However, the difference in Bayesian evidence, compared to the ΛCDM model, has still been inconclusive, so no model should be discarded.

A result which is in common with Chap. 4 is that also for the model in Chap. 5 the cosmological background data have discarded slow transitions and favored fast ones. A 1-σ lower bound for the rapidity of $\beta > 300$ has been found, while slow transitions have strongly been disfavored by the cosmological data; transitions of $\beta \lesssim 40$ have even completely been discarded by CMB shift parameters. A correlation between the transition redshift and rapidity has also been found for intermediate rapidity regimes ($40 \lesssim \beta \lesssim 300$), implying that slower transitions should have occurred earlier. However, the cosmological analysis for this UDM model has not shown any appreciable difference beyond a certain big value of rapidity ($\beta \gtrsim 800$). Therefore, in this case the cosmological data have been unable to distinguish any upper bound for the transition rapidity once the fast-transition regime was reached.

Therefore, we have shown that cosmological background data allow the existence of UDM models as long as their transition between a dark matter and a dark energy behavior is fast. Although these cosmological data seem amenable to the expansion history of these UDM models (which is different from that of ΛCDM, or course), further studies on dynamical probes are required to definitely support or discard them. For instance, an actual computation of the evolution of perturbations would be interesting. Testing UDM perturbations with actual data would help us infer whether dynamical data (matter power spectrum) can be fitted in these scenarios, and we could even check if there are some distinctive signatures which make them easily distinguishable from the ΛCDM model. In any case, the different expansionary features of UDM models would affect significantly the integrated Sachs-Wolfe effect measured in the CMB, and this would also be worth testing.

While in Part II we have mainly focused on using geometric distance measurements to constrain the parameter space of different models and perform model selection according to the Bayesian evidence, in Part III we have focused on an alternative probe which could be employed in the near future and might provide a complementary approach to dark energy studies. We have focused on the cosmic redshift drift originated by the expanding universe, which allows to carry out the so-called Sandage-Loeb (SL) test. Despite the fact these are background data, such observations are not distance measurements per se, but rather dynamical observations, so they constrain the Hubble function directly instead of its integration, thus greatly improving the performance of this type of observations. The fact that these Sandage-Loeb surveys are planned to observe high-redshift quasars in a redshift range with few data collected so far, makes them even more valuable.

In Chap. 6, we have analyzed the constraining power of the future Sandage-Loeb observations based on the cosmic redshift drift of high-redshift quasars. To analyze future observations without biasing towards a particular chosen fiducial cosmological model, we have generated mock data sets by a model-independent procedure, set on the specifications of near-future surveys. We have included in our analysis also future *Euclid* BAO and *W-First* SNe Ia sets as auxiliary mock data sets to compare with SL ones.

Then, we have performed a Bayesian analysis to see how the future surveys constrain several tested models. The results have shown that SL data sets will provide a noticeable improvement to constrains on dynamical dark energy parameters, compared to historical SNe Ia or BAO. In particular, they will help to narrow the uncertainty on the matter density parameter Ω_m.

Moreover, our results have also shown that each data set has different correlation angles regarding dark energy parameters, it being particulary evident in the Sandage-Loeb case compared to BAO and SNe Ia. This means that by combining such data sets, even for the lowest observation period of SL, a tighter constrain on the dark energy parameters could be possible. Besides, cosmological measurements up to such a high redshift range coming from SL could provide important information regarding the possible evolution of the dark energy equation of state, that is, whether it is time dependent or not.

To sum up, in this thesis we have shown that there is still plenty of room to have new cosmological models with different evolutions for the dark sector between the extremely high redshift of the CMB data and low redshift observations as SNe Ia and BAO. Measurements of intermediate redshifts coming from Sandage-Loeb observations of high-redshift quasars could help filling the gap and increasing the knowledge. Overall, we have shown that cosmological background data, both as distance measurements or future dynamic observations, reveal more information than expected once high precision cosmology is attained. One such example is the fact that background data back up the rapidity constraint of the UDM transitions imposed by the perturbation theory. With the next generations of cosmological background observations, some light may be shed to the dark sector of the universe, especially to dark energy, and for all these reasons cosmological background observations are and will be of utmost importance.

Bibliography

[1] *"CODEX Phase A Science Case, document E-TRE-IOA-573-0001 Issue 1 (2010)"*, CODEX Phase A Science Case, document E-TRE-IOA-573-0001 Issue 1 (2010).

[2] *"SKA Level 0 Science Requirements, document SKA-TEL-SKO-0000007 (2015)"*, SKA Level 0 Science Requirements, document SKA-TEL-SKO-0000007 (2015).

[3] P. Ade et al., *"Planck 2013 results. XVI. Cosmological parameters"*, Astron.Astrophys. **571**, A16 (2014).

[4] P. A. R. Ade et al., *"Planck 2015 results. XIV. Dark energy and modified gravity"*, Astron. Astrophys. **594**, A14 (2016).

[5] P. A. R. Ade et al., *"Planck 2015 results. XIII. Cosmological parameters"*, Astron. Astrophys. **594**, A13 (2016).

[6] N. Aghanim et al., *"Planck 2018 results. VI. Cosmological parameters"*.

[7] H. Akaike, *"A New Look at the Statistical Model Identification"*, IEEE Transactions on Automatic Control **19**, 716-723 (1974).

[8] S. Alam et al., *"The Eleventh and Twelfth Data Releases of the Sloan Digital Sky Survey: Final Data from SDSS-III"*, Astrophys. J. Suppl. **219**, 12 (2015).

[9] S. Alam et al., *"The clustering of galaxies in the completed SDSS-III Baryon Oscillation Spectroscopic Survey: cosmological analysis of the DR12 galaxy sample"*, Mon. Not. Roy. Astron. Soc. **470**, 2617-2652 (2017).

[10] C. Alcock and B. Paczynski, *"An evolution free test for non-zero cosmological constant"*, Nature **281**, 358-359 (1979).

[11] S. Allan, *"The Change of Redshift and Apparent Luminosity of Galaxies due to the Deceleration of Selected Expanding Universes"*, Astrophys. J. **136**, 319-333 (1962).

[12] R. A. Alpher and R. Herman, *"Evolution of the Universe"*, Nature **162**, 774-775 (1948).

[13] R. A. Alpher, H. Bethe, and G. Gamow, *"The origin of chemical elements"*, Phys. Rev. **73**, 803-804 (1948).

[14] R. A. Alpher, J. W. Follin, and R. C. Herman, *"Physical Conditions in the Initial Stages of the Expanding Universe"*, Phys. Rev. **92**, 1347-1361 (1953).

[15] R. Amanullah et al., *"Spectra and Light Curves of Six Type Ia Supernovae at 0.511 $< z <$ 1.12 and the Union2 Compilation"*, Astrophys. J. **716**, 712-738 (2010).

[16] L. Amendola, *"Coupled quintessence"*, Phys. Rev. **D62**, 043511 (2000).

[17] L. Amendola et al., *"Cosmology and Fundamental Physics with the Euclid Satellite"*.

[18] M. E. Araujo and W. R. Stoeger, *"Using Time Drift of Cosmological Redshifts to find the Mass-Energy Density of the Universe"*, Phys. Rev. **D82**, 123513 (2010).

[19] C. Armendariz-Picon, V. F. Mukhanov, and P. J. Steinhardt, *"Essentials of k essence"*, Phys. Rev. **D63**, 103510 (2001).

[20] E. Aubourg et al., *"Cosmological implications of baryon acoustic oscillation measurements"*, Phys. Rev. **D92**, 123516 (2015).

[21] H. W. Babcock, *"The rotation of the Andromeda Nebula"*, Lick Observatory Bulletin **19**, 41-51 (1939).

[22] A. Balcerzak and M. P. Dabrowski, *"Redshift drift in a pressure gradient cosmology"*, Phys. Rev. **D87**, 063506 (2013).

[23] A. Balcerzak and M. P. Dabrowski, *"Redshift drift in varying speed of light cosmology"*, Phys. Lett. **B728**, 15-18 (2014).

[24] K. Bamba, S. Capozziello, S. Nojiri, and S. D. Odintsov, *"Dark energy cosmology: the equivalent description via different theoretical models and cosmography tests"*, Astrophys.Space Sci. **342**, 155-228 (2012).

[25] S. Banerjee, N. Jayswal, and T. P. Singh, *"Cosmic Acceleration in a Model of Fourth Order Gravity"*, Phys. Rev. **D92**, 084026 (2015).

[26] M. Bartelmann and P. Schneider, *"Weak gravitational lensing"*, Phys. Rept. **340**, 291-472 (2001).

[27] B. A. Bassett and R. Hlozek, *"Baryon Acoustic Oscillations"*.

[28] D. Baumann. *"Inflation"*. In *Physics of the large and the small, TASI 09, proceedings of the Theoretical Advanced Study Institute in Elementary Particle Physics, Boulder, Colorado, USA, 1-26 June 2009*, pages 523–686, (2011). doi: 10.1142/9789814327183_0010.

[29] M. Beltran, J. Garcia-Bellido, J. Lesgourgues, A. R. Liddle, and A. Slosar, *"Bayesian model selection and isocurvature perturbations"*, Phys. Rev. **D71**, 063532 (2005).

[30] C. Bennett, D. Larson, J. Weiland, and G. Hinshaw, *"The 1% Concordance Hubble Constant"*, Astrophys. J. **794**, 135 (2014).

[31] C. L. Bennett, D. Larson, J. L. Weiland, N. Jarosik, G. Hinshaw, N. Odegard, K. M. Smith, R. S. Hill, B. Gold, M. Halpern, E. Komatsu, M. R. Nolta, L. Page, D. N. Spergel, E. Wollack, J. Dunkley, A. Kogut, M. Limon, S. S. Meyer, G. S. Tucker, and E. L. Wright, *"Nine-year Wilkinson Microwave Anisotropy Probe (WMAP) Observations: Final Maps and Results"*, Astrophys. J. Suppl. **208**, 20 (2013).

[32] M. C. Bento, O. Bertolami, and A. A. Sen, *"Generalized Chaplygin gas, accelerated expansion and dark energy matter unification"*, Phys. Rev. **D66**, 043507 (2002).

[33] L. Berezhiani and J. Khoury, *"Theory of dark matter superfluidity"*, Phys. Rev. **D92**, 103510 (2015).

[34] D. Bertacca and N. Bartolo, *"ISW effect in Unified Dark Matter Scalar Field Cosmologies: An analytical approach"*, JCAP **0711**, 026 (2007).

[35] D. Bertacca, N. Bartolo, A. Diaferio, and S. Matarrese, *"How the Scalar Field of Unified Dark Matter Models Can Cluster"*, JCAP **0810**, 023 (2008).

[36] D. Bertacca, N. Bartolo, and S. Matarrese, *"Unified Dark Matter Scalar Field Models"*, Adv. Astron. **2010**, 904379 (2010).

[37] D. Bertacca, M. Bruni, O. F. Piattella, and D. Pietrobon, *"Unified Dark Matter scalar field models with fast transition"*, JCAP **1102**, 018 (2011).

[38] E. Berti et al., *"Testing General Relativity with Present and Future Astrophysical Observations"*, Class. Quant. Grav. **32**, 243001 (2015).

[39] G. Bertone, D. Hooper, and J. Silk, *"Particle dark matter: Evidence, candidates and constraints"*, Phys. Rept. **405**, 279-390 (2005).

[40] F. Beutler, C. Blake, M. Colless, D. H. Jones, L. Staveley-Smith, L. Campbell, Q. Parker, W. Saunders, and F. Watson, *"The 6dF Galaxy Survey: Baryon Acoustic Oscillations and the Local Hubble Constant"*, Mon. Not. Roy. Astron. Soc. **416**, 3017-3032 (2011).

[41] N. Bilic, *"Thermodynamics of k-essence"*, Phys. Rev. **D78**, 105012 (2008).

[42] N. Bilic, G. B. Tupper, and R. D. Viollier, *"Unification of dark matter and dark energy: The Inhomogeneous Chaplygin gas"*, Phys.Lett. **B535**, 17-21 (2002).

[43] N. Bilic, R. J. Lindebaum, G. B. Tupper, and R. D. Viollier, *"Nonlinear evolution of dark matter and dark energy in the Chaplygin-gas cosmology"*, JCAP **0411**, 008 (2004).

[44] C. Blake et al., *"The WiggleZ Dark Energy Survey: Joint measurements of the expansion and growth history at $z < 1$"*, Mon. Not. Roy. Astron. Soc. **425**, 405-414 (2012).

[45] H. Bondi and T. Gold, *"The Steady-State Theory of the Expanding Universe"*, Mon. Not. Roy. Astron. Soc. **108**, 252 (1948).

[46] G. E. P. Box and G. C. Tiao. *Bayesian Inference in Statistical Analysis*. Addison-Wesley Publishing Company, (1973).

[47] D. Branch and G. A. Tammann, *"Type ia supernovae as standard candles"*, Ann. Rev. Astron. Astrophys. **30**, 359-389 (1992).

[48] M. Bruni, R. Lazkoz, and A. Rozas-Fernandez, *"Phenomenological models for Unified Dark Matter with fast transition"*, Mon. Not. Roy. Astron. Soc. **431**, 2907-2916 (2013).

[49] M. Bucher, *"Physics of the cosmic microwave background anisotropy"*, Int. J. Mod. Phys. **D24**, 1530004 (2015).

[50] P. Bull et al., *"Beyond ΛCDM: Problems, solutions, and the road ahead"*, Phys. Dark Univ. **12**, 56-99 (2016).

[51] M. E. Burbidge, G. R. Burbidge, W. A. Fowler, and F. Hoyle, *"Synthesis of the elements in stars"*, Rev. Mod. Phys. **29**, 547-650 (1957).

[52] R. R. Caldwell and A. Stebbins, *"A Test of the Copernican Principle"*, Phys. Rev. Lett. **100**, 191302 (2008).

[53] S. Camera, D. Bertacca, A. Diaferio, N. Bartolo, and S. Matarrese, *"Weak lensing signal in Unified Dark Matter models"*, Mon. Not. Roy. Astron. Soc. **399**, 1995-2003 (2009).

[54] S. Camera, T. D. Kitching, A. F. Heavens, D. Bertacca, and A. Diaferio, *"Measuring Unified Dark Matter with 3D cosmic shear"*, Mon. Not. Roy. Astron. Soc. **415**, 399-409 (2011).

[55] S. Capozziello, L. Consiglio, M. De Laurentis, G. De Rosa, and C. Di Donato, *"The missing matter problem: from the dark matter search to alternative hypotheses"*.

[56] S. M. Carroll, *"The Cosmological constant"*, Living Rev. Rel. **4**, 1 (2001).

[57] S. M. Carroll, W. H. Press, and E. L. Turner, *"The Cosmological constant"*, Ann. Rev. Astron. Astrophys. **30**, 499-542 (1992).

[58] D. Carturan and F. Finelli, *"Cosmological effects of a class of fluid dark energy models"*, Phys. Rev. **D68**, 103501 (2003).

[59] M. Chevallier and D. Polarski, *"Accelerating universes with scaling dark matter"*, Int. J. Mod. Phys. **D10**, 213-224 (2001).

[60] T. Chiba, T. Okabe, and M. Yamaguchi, *"Kinetically driven quintessence"*, Phys. Rev. **D62**, 023511 (2000).

[61] N. Christensen, R. Meyer, L. Knox, and B. Luey, *"II. Bayesian methods for cosmological parameter estimation from cosmic microwave background measurements"*, Class. Quant. Grav. **18**, 2677 (2001).

[62] C.-H. Chuang and Y. Wang, *"Measurements of $H(z)$ and $D_A(z)$ from the Two-Dimensional Two-Point Correlation Function of Sloan Digital Sky Survey Luminous Red Galaxies"*, Mon. Not. Roy. Astron. Soc. **426**, 226 (2012).

[63] C.-H. Chuang and Y. Wang, *"Measurements of $H(z)$ and $D_A(z)$ from the Two-Dimensional Two-Point Correlation Function of Sloan Digital Sky Survey Luminous Red Galaxies"*, Mon.Not.Roy.Astron.Soc. **426**, 226 (2012).

[64] C.-H. Chuang et al., *"The clustering of galaxies in the SDSS-III Baryon Oscillation Spectroscopic Survey: single-probe measurements and the strong power of normalized growth rate on constraining dark energy"*, Mon. Not. Roy. Astron. Soc. **433**, 3559 (2013).

[65] C. Clarkson, B. Bassett, and T. H.-C. Lu, *"A general test of the Copernican Principle"*, Phys. Rev. Lett. **101**, 011301 (2008).

[66] T. Clifton, P. G. Ferreira, A. Padilla, and C. Skordis, *"Modified Gravity and Cosmology"*, Phys. Rept. **513**, 1-189 (2012).

[67] D. Coe, *"Fisher Matrices and Confidence Ellipses: A Quick-Start Guide and Software"*.

[68] A. Conley et al., *"Supernova Constraints and Systematic Uncertainties from the First 3 Years of the Supernova Legacy Survey"*, Astrophys. J. Suppl. **192**, 1 (2011).

[69] E. J. Copeland, M. Sami, and S. Tsujikawa, *"Dynamics of dark energy"*, Int. J. Mod. Phys. **D15**, 1753-1936 (2006).

[70] P.-S. Corasaniti, D. Huterer, and A. Melchiorri, *"Exploring the Dark Energy Redshift Desert with the Sandage-Loeb Test"*, Phys. Rev. **D75**, 062001 (2007).

[71] R. D. Cousins, *"Why isn't every physicist a Bayesian?"*, Am. J. Phys. **63**, 398 (1995).

[72] J. P. Cox. *Theory of stellar pulsation*. (1980).

[73] M. Crocce and R. Scoccimarro, *"Nonlinear Evolution of Baryon Acoustic Oscillations"*, Phys. Rev. **D77**, 023533 (2008).

[74] N. Cruz, P. F. González-Díaz, A. Rozas-Fernández, and G. Sanchez, *"Holographic kinetic k-essence model"*, Phys. Lett. **B679**, 293-297 (2009).

[75] R. de Grijs. *An Introduction to Distance Measurement in Astronomy*. Wiley & Sons, (2011).

[76] J. De-Santiago, D. Wands, and Y. Wang. *"Inhomogeneous and interacting vacuum energy"*. In *6th International Meeting on Gravitation and Cosmology Guadalajara, Jalisco, Mexico, May 21-25, 2012*, (2012). URL https://inspirehep.net/record/1184300/files/arXiv:1209.0563.pdf.

[77] W. de Sitter, *"Einstein's theory of gravitation and its astronomical consequences, Third Paper"*, Mon. Not. Roy. Astron. Soc. **78**, 3-28 (1917).

[78] T. Denkiewicz, M. P. Dąbrowski, C. J. A. P. Martins, and P. E. Vielzeuf, *"Redshift drift test of exotic singularity universes"*, Phys. Rev. **D89**, 083514 (2014).

[79] R. H. Dicke, P. J. E. Peebles, P. G. Roll, and D. T. Wilkinson, *"Cosmic Black-Body Radiation"*, Astrophys. J. **142**, 414-419 (1965).

[80] A. Diez-Tejedor and A. Feinstein, *"Relativistic hydrodynamics with sources for cosmological K-fluids"*, Int. J. Mod. Phys. **D14**, 1561-1576 (2005).

[81] S. Dodelson. *Modern Cosmology*. Academic Press, Amsterdam, (2003). ISBN 9780122191411. URL http://www.slac.stanford.edu/spires/find/books/www?cl=QB981:D62:2003.

[82] J. Dunkley, M. Bucher, P. G. Ferreira, K. Moodley, and C. Skordis, *"Fast and reliable mcmc for cosmological parameter estimation"*, Mon. Not. Roy. Astron. Soc. **356**, 925-936 (2005).

[83] A. S. Eddington. *Internal Constitution of the Stars*. Cambridge University Press, (1926).

[84] G. Efstathiou, S. L. Bridle, A. N. Lasenby, M. P. Hobson, and R. S. Ellis, *"Constraints on omega(lambda) and omega(m) from distant type 1a supernovae and cosmic microwave background anisotropies"*, Mon. Not. Roy. Astron. Soc. **303**, 47 (1999).

[85] J. Einasto. *"Dark Matter"*. In *Astronomy and Astrophysics 2010, [Eds. Oddbjorn Engvold, Rolf Stabell, Bozena Czerny, John Lattanzio], in Encyclopedia of Life Support Systems (EOLSS), Developed under the Auspices of the UNESCO, Eolss Publishers, Oxford ,UK*, (2009). URL http://inspirehep.net/record/810367/files/arXiv:0901.0632.pdf.

[86] A. Einstein, *"The Field Equations of Gravitation"*, Sitzungsber. Preuss. Akad. Wiss. Berlin (Math. Phys.) **1915**, 844-847 (1915).

[87] A. Einstein, *"Cosmological Considerations in the General Theory of Relativity"*, Sitzungsber. Preuss. Akad. Wiss. Berlin (Math. Phys.) **1917**, 142-152 (1917).

[88] D. J. Eisenstein and W. Hu, *"Baryonic features in the matter transfer function"*, Astrophys. J. **496**, 605 (1998).

[89] D. J. Eisenstein, H.-j. Seo, E. Sirko, and D. Spergel, *"Improving Cosmological Distance Measurements by Reconstruction of the Baryon Acoustic Peak"*, Astrophys. J. **664**, 675-679 (2007).

[90] D. J. Eisenstein, H.-j. Seo, and M. J. White, *"On the Robustness of the Acoustic Scale in the Low-Redshift Clustering of Matter"*, Astrophys. J. **664**, 660-674 (2007).

[91] D. J. Eisenstein et al., *"Detection of the Baryon Acoustic Peak in the Large-Scale Correlation Function of SDSS Luminous Red Galaxies"*, Astrophys. J. **633**, 560-574 (2005).

[92] D. J. Eisenstein et al., *"SDSS-III: Massive Spectroscopic Surveys of the Distant Universe, the Milky Way Galaxy, and Extra-Solar Planetary Systems"*, Astron. J. **142**, 72 (2011).

[93] C. Escamilla-Rivera, R. Lazkoz, V. Salzano, and I. Sendra, *"Tension between SN and BAO: current status and future forecasts"*, JCAP **1109**, 003 (2011).

[94] M. W. Feast and R. M. Catchpole, *"The Cepheid period-luminosity zero-point from HIPPARCOS trigonometrical parallaxes"*, Mon. Not. Roy. Astron. Soc. **286**, L1-L5 (1997).

[95] D. Fixsen, *"The Temperature of the Cosmic Microwave Background"*, Astrophys. J. **707**, 916-920 (2009).

[96] A. Font-Ribera, P. McDonald, N. Mostek, B. A. Reid, H.-J. Seo, and A. Slosar, *"DESI and other dark energy experiments in the era of neutrino mass measurements"*, JCAP **1405**, 023 (2014).

[97] A. Font-Ribera et al., *"Quasar-Lyman α Forest Cross-Correlation from BOSS DR11 : Baryon Acoustic Oscillations"*, JCAP **1405**, 027 (2014).

[98] W. L. Freedman, *"New Cepheid distances to nearby galaxies based on BVRI CCD photometry. I - IC 1613"*, Astrophys. J. **326**, 691-709 (1988).

[99] W. L. Freedman, B. F. Madore, S. L. Hawley, I. K. Horowitz, J. Mould, M. Navarrete, and S. Sallmen, *"New Cepheid distances to nearby galaxies based on BVRI CCD photometry. III - NGC 300"*, Astrophys. J. **396**, 80-96 (1992).

[100] A. Friedmann, *"On the Possibility of a world with constant negative curvature of space"*, Z. Phys. **21**, 326-332 (1924). [Gen. Rel. Grav.31,2001(1999)].

[101] J. Garriga and V. F. Mukhanov, *"Perturbations in k-inflation"*, Phys. Lett. **B458**, 219-225 (1999).

[102] A. Gelman and D. B. Rubin, *"Inference from Iterative Simulation Using Multiple Sequences"*, Statist. Sci. **7**, 457-472 (1992).

[103] J.-J. Geng, J.-F. Zhang, and X. Zhang, *"Quantifying the impact of future Sandage-Loeb test data on dark energy constraints"*, JCAP **1407**, 006 (2014).

[104] J.-J. Geng, J.-F. Zhang, and X. Zhang, *"Parameter estimation with Sandage-Loeb test"*, JCAP **1412**, 018 (2014).

[105] J.-J. Geng, R.-Y. Guo, D.-Z. He, J.-F. Zhang, and X. Zhang, *"Redshift drift constraints on $f(T)$ gravity"*, Front. Phys.(Beijing) **10**, 109501 (2015).

[106] J.-J. Geng, Y.-H. Li, J.-F. Zhang, and X. Zhang, *"Redshift drift exploration for interacting dark energy"*, Eur. Phys. J. **C75**, 356 (2015).

[107] D. Giannakis and W. Hu, *"Kinetic unified dark matter"*, Phys. Rev. **D72**, 063502 (2005).

[108] M. Goliath, R. Amanullah, P. Astier, A. Goobar, and R. Pain, *"Supernovae and the nature of the dark energy"*, Astron. Astrophys. **380**, 6-18 (2001).

[109] J. Goodman, *"Geocentrism reexamined"*, Phys. Rev. **D52**, 1821-1827 (1995).

[110] C. Gordon and R. Trotta, *"Bayesian Calibrated Significance Levels Applied to the Spectral Tilt and Hemispherical Asymmetry"*, Mon.Not.Roy.Astron.Soc. **382**, 1859-1863 (2007).

[111] R.-Y. Guo and X. Zhang, *"Constraining dark energy with Hubble parameter measurements: an analysis including future redshift-drift observations"*, Eur. Phys. J. **C76**, 163 (2016).

[112] J. Guy et al., *"SALT2: Using distant supernovae to improve the use of Type Ia supernovae as distance indicators"*, Astron. Astrophys. **466**, 11-21 (2007).

[113] A. J. S. Hamilton, *"Measuring Omega and the real correlation function from the redshift correlation function"*, Astrophys. J. **385**, L5-L8 (1992).

[114] W. K. Hastings, *"Monte Carlo Sampling Methods Using Markov Chains and Their Applications"*, Biometrika **57**, 97-109 (1970).

[115] D. W. Hogg, *"Distance measures in cosmology"*.

[116] D. A. Howell, *"Type Ia Supernovae as Stellar Endpoints and Cosmological Tools"*, Nature Commun. **2**, 350 (2011).

[117] F. Hoyle, *"A New Model for the Expanding Universe"*, Mon. Not. Roy. Astron. Soc. **108**, 372 (1948).

[118] F. Hoyle, *"On Nuclear Reactions Occuring in Very Hot Stars. 1. The Synthesis of Elements from Carbon to Nickel"*, Astrophys. J. Suppl. **1**, 121-146 (1954).

[119] F. Hoyle and R. J. Tayler, *"The Mystery of the Cosmic Helium Abundance"*, Nature **203**, 1108 (1964).

[120] E. Y. Hsiao, A. J. Conley, D. A. Howell, M. Sullivan, C. J. Pritchet, R. G. Carlberg, P. E. Nugent, and M. M. Phillips, *"K-corrections and spectral templates of Type Ia supernovae"*, Astrophys. J. **663**, 1187-1200 (2007).

[121] W. Hu, *"Structure formation with generalized dark matter"*, Astrophys. J. **506**, 485-494 (1998).

[122] W. Hu and S. Dodelson, *"Cosmic microwave background anisotropies"*, Ann. Rev. Astron. Astrophys. **40**, 171-216 (2002).

[123] W. Hu and N. Sugiyama, *"Small scale cosmological perturbations: An Analytic approach"*, Astrophys. J. **471**, 542-570 (1996).

[124] W. Hu and M. J. White, *"Acoustic signatures in the cosmic microwave background"*, Astrophys. J. **471**, 30-51 (1996).

[125] E. Hubble, *"A relation between distance and radial velocity among extra-galactic nebulae"*, Proc. Nat. Acad. Sci. **15**, 168-173 (1929).

[126] E. Hubble, *"The Distribution of Extra-Galactic Nebulae"*, Astrophys. J. **79**, 8 (1934).

[127] E. P. Hubble, *"Extragalactic nebulae"*, Astrophys. J. **64**, 321-369 (1926).

[128] S. Jha, A. G. Riess, and R. P. Kirshner, *"Improved Distances to Type Ia Supernovae with Multicolor Light Curve Shapes: MLCS2k2"*, Astrophys. J. **659**, 122-148 (2007).

[129] N. Kaiser, *"Clustering in real space and in redshift space"*, Mon. Not. Roy. Astron. Soc. **227**, 1-27 (1987).

[130] A. Y. Kamenshchik, U. Moschella, and V. Pasquier, *"An Alternative to quintessence"*, Phys.Lett. **B511**, 265-268 (2001).

[131] J. U. Kang, V. Vanchurin, and S. Winitzki, *"Attractor scenarios and superluminal signals in k-essence cosmology"*, Phys. Rev. **D76**, 083511 (2007).

[132] E. A. Kazin et al., *"The Baryonic Acoustic Feature and Large-Scale Clustering in the SDSS LRG Sample"*, Astrophys. J. **710**, 1444-1461 (2010).

[133] M. Kendall and A. Stuart. *The advanced theory of statistics. Vol.2: Inference and relationship*. (1979).

[134] M. Killedar and G. F. Lewis, *"Lyman alpha absorbers in motion: consequences of gravitational lensing for the cosmological redshift drift experiment"*, Mon. Not. Roy. Astron. Soc. **402**, 650 (2010).

[135] A. G. Kim, E. V. Linder, J. Edelstein, and D. Erskine, *"Giving Cosmic Redshift Drift a Whirl"*, Astropart. Phys. **62**, 195-205 (2015).

[136] H.-R. Klöckner, D. Obreschkow, C. Martins, A. Raccanelli, D. Champion, A. L. Roy, A. Lobanov, J. Wagner, and R. Keller, *"Real time cosmology - A direct measure of the expansion rate of the Universe with the SKA"*, PoS **AASKA14**, 027 (2015).

[137] R. A. Knop et al., *"New constraints on Omega(M), Omega(lambda), and w from an independent set of eleven high-redshift supernovae observed with HST"*, Astrophys. J. **598**, 102 (2003).

[138] S. M. Koksbang and S. Hannestad, *"Redshift drift in an inhomogeneous universe: averaging and the backreaction conjecture"*, JCAP **1601**, 009 (2016).

[139] E. Komatsu, K. M. Smith, J. Dunkley, C. L. Bennett, B. Gold, G. Hinshaw, N. Jarosik, D. Larson, M. R. Nolta, L. Page, D. N. Spergel, M. Halpern, R. S. Hill, A. Kogut, M. Limon, S. S. Meyer, N. Odegard, G. S. Tucker, J. L. Weiland, E. Wollack, and E. L. Wright, *"Seven-year Wilkinson Microwave Anisotropy Probe (WMAP) Observations: Cosmological Interpretation"*, Astrophys. J. Suppl. **192**, 18 (2011).

[140] M. Kunz, *"The phenomenological approach to modeling the dark energy"*, Comptes Rendus Physique **13**, 539-565 (2012).

[141] S. D. Landy and A. S. Szalay, *"Bias and variance of angular correlation functions"*, Astrophys. J. **412**, 64 (1993).

[142] R. Laureijs et al., *"Euclid Definition Study Report"*.

[143] R. Lazkoz, I. Leanizbarrutia, and V. Salzano, *"Cosmological constraints on fast transition unified dark energy and dark matter models"*, Phys. Rev. **D93**, 043537 (2016).

[144] H. S. Leavitt and E. C. Pickering, *"Periods of 25 Variable Stars in the Small Magellanic Cloud"*, Harvard Obs. Circ. **173**, 1-3 (1912).

[145] B. Leibundgut, *"Supernovae and Cosmology"*, Gen. Rel. Grav. **40**, 221 (2008).

[146] G. Lemaitre, *"A Homogeneous Universe of Constant Mass and Growing Radius Accounting for the Radial Velocity of Extragalactic Nebulae"*, Annales Soc. Sci. Bruxelles A **47**, 49-59 (1927). [Gen. Rel. Grav.45,no.8,1635(2013)].

[147] G. Lemaitre, *"Republication of: The beginning of the world from the point of view of quantum theory"*, Nature **127**, 706 (1931). [Gen. Rel. Grav.43,2929(2011)].

[148] A. Lewis and S. Bridle, *"Cosmological parameters from CMB and other data: A Monte Carlo approach"*, Phys. Rev. **D66**, 103511 (2002).

[149] A. Lewis and A. Challinor, *"Weak gravitational lensing of the CMB"*, Phys. Rept. **429**, 1-65 (2006).

[150] M. Li, X.-D. Li, S. Wang, and Y. Wang, *"Dark Energy: A Brief Review"*, Front. Phys.(Beijing) **8**, 828-846 (2013).

[151] Z. Li, K. Liao, P. Wu, H. Yu, and Z.-H. Zhu, *"Probing modified gravity theories with the Sandage-Loeb test"*, Phys. Rev. **D88**, 023003 (2013).

[152] A. R. Liddle and L. A. Urena-Lopez, *"Inflation, dark matter and dark energy in the string landscape"*, Phys. Rev. Lett. **97**, 161301 (2006).

[153] A. R. Liddle, P. Mukherjee, and D. Parkinson, *"Cosmological model selection"*.

[154] E. V. Linder, *"Exploring the expansion history of the universe"*, Phys. Rev. Lett. **90**, 091301 (2003).

[155] J. Liske et al., *"Cosmic dynamics in the era of Extremely Large Telescopes"*, Mon. Not. Roy. Astron. Soc. **386**, 1192-1218 (2008).

[156] J. Liu and H. Wei, *"Cosmological models and gamma-ray bursts calibrated by using Padé method"*, Gen. Rel. Grav. **47**, 141 (2015).

[157] A. Loeb, *"Direct Measurement of Cosmological Parameters from the Cosmic Deceleration of Extragalactic Objects"*, Astrophys. J. **499**, L111-L114 (1998).

[158] V. Lukovic, P. Cabella, and N. Vittorio, *"Dark matter in cosmology"*, Int.J.Mod.Phys. **A29**, 1443001 (2014).

[159] D. J. C. MacKay. *Information Theory, Inference and Learning Algorithms*. Cambridge University Press, (2005).

[160] L. M. Macri, C.-C. Ngeow, S. M. Kanbur, S. Mahzooni, and M. T. Smitka, *"Large Magellanic Cloud Near-Infrared Synoptic Survey. I. Cepheid variables and the calibration of the Leavitt Law"*, Astron. J. **149**, 117 (2015).

[161] B. F. Madore and W. L. Freedman, *"The Cepheid distance scale"*, Publ. Astron. Soc. Pac. **103**, 933-957 (1991).

[162] K. Maeda and Y. Terada, *"Progenitors of type Ia supernovae"*, Int. J. Mod. Phys. **D25**, 1630024 (2016).

[163] M. Makler, S. Quinet de Oliveira, and I. Waga, *"Constraints on the generalized Chaplygin gas from supernovae observations"*, Phys. Lett. **B555**, 1 (2003).

[164] J. Martin, *"Everything You Always Wanted To Know About The Cosmological Constant Problem (But Were Afraid To Ask)"*, Comptes Rendus Physique **13**, 566-665 (2012).

[165] M. Martinelli, S. Pandolfi, C. J. A. P. Martins, and P. E. Vielzeuf, *"Probing dark energy with the Sandage-Loeb test"*, Phys. Rev. **D86**, 123001 (2012).

[166] C. J. A. P. Martins, M. Martinelli, E. Calabrese, and M. P. L. P. Ramos, *"Real-time cosmography with redshift derivatives"*, Phys. Rev. **D94**, 043001 (2016).

[167] F. Melia, *"Definitive test of the $Rh = ct$ universe using redshift drift"*, Mon. Not. Roy. Astron. Soc. **463**, L61-L63 (2016).

[168] N. Metropolis, A. W. Rosenbluth, M. N. Rosenbluth, A. H. Teller, and E. Teller, *"Equation of state calculations by fast computing machines"*, J. Chem. Phys. **21**, 1087-1092 (1953).

[169] P. Mishra, M.-N. Celerier, and T. P. Singh, *"Redshift drift as a test for discriminating between different cosmological models"*, Phys. Rev. **D86**, 083520 (2012).

[170] B. Moraes and D. Polarski, *"The complementarity of the redshift drift"*, Phys. Rev. **D84**, 104003 (2011).

[171] M. Moresco, L. Pozzetti, A. Cimatti, R. Jimenez, C. Maraston, L. Verde, D. Thomas, A. Citro, R. Tojeiro, and D. Wilkinson, *"A 6% measurement of the Hubble parameter at $z \sim 0.45$: direct evidence of the epoch of cosmic re-acceleration"*, JCAP **1605**, 014 (2016).

[172] P. Mukherjee, D. Parkinson, and A. R. Liddle, *"A nested sampling algorithm for cosmological model selection"*, Astrophys. J. **638**, L51-L54 (2006).

[173] R. M. Neal. *"Bayesian Learning via Stochastic Dynamics"*. In S. J. Hanson, J. D. Cowan, and C. L. Giles, editors, *Advances in Neural Information Processing Systems 5*, pages 475–482. Morgan-Kaufmann, (1993). URL `http://papers.nips.cc/paper/613-bayesian-learning-via-stochastic-dynamics.pdf`.

[174] R. M. Neal. *"Probabilistic Inference Using Markov Chain Monte Carlo Methods (CRG-TR-93-1)"*. Technical report, Dept. of Computer Science, University of Toronto, (1993).

[175] T. Padmanabhan and T. R. Choudhury, *"A theoretician's analysis of the supernova data and the limitations in determining the nature of dark energy"*, Mon. Not. Roy. Astron. Soc. **344**, 823-834 (2003).

[176] P. Peebles and B. Ratra, *"The Cosmological constant and dark energy"*, Rev.Mod.Phys. **75**, 559-606 (2003).

[177] A. A. Penzias and R. W. Wilson, *"A Measurement of excess antenna temperature at 4080-Mc/s"*, Astrophys. J. **142**, 419-421 (1965).

[178] S. Perlmutter et al., *"Measurements of Omega and Lambda from 42 high redshift supernovae"*, Astrophys. J. **517**, 565-586 (1999).

[179] A. H. Peter, *"Dark Matter: A Brief Review"*, Proceedings of Science (Bash11) **014**, (2011).

[180] M. M. Phillips, *"The absolute magnitudes of Type IA supernovae"*, Astrophys. J. **413**, L105-L108 (1993).

[181] O. F. Piattella, *"The extreme limit of the generalized Chaplygin gas"*, JCAP **1003**, 012 (2010).

[182] O. F. Piattella, D. Bertacca, M. Bruni, and D. Pietrobon, *"Unified Dark Matter models with fast transition"*, JCAP **1001**, 014 (2010).

[183] D. Pietrobon, A. Balbi, M. Bruni, and C. Quercellini, *"Affine parameterization of the dark sector: costraints from WMAP5 and SDSS"*, Phys. Rev. **D78**, 083510 (2008).

[184] C. Quercellini, L. Amendola, A. Balbi, P. Cabella, and M. Quartin, *"Real-time Cosmology"*, Phys. Rept. **521**, 95-134 (2012).

[185] A. G. Riess, W. H. Press, and R. P. Kirshner, *"A Precise distance indicator: Type Ia supernova multicolor light curve shapes"*, Astrophys. J. **473**, 88 (1996).

[186] A. G. Riess et al., *"Observational evidence from supernovae for an accelerating universe and a cosmological constant"*, Astron.J. **116**, 1009-1038 (1998).

[187] A. G. Riess et al., *"Type Ia supernova discoveries at $z > 1$ from the Hubble Space Telescope: Evidence for past deceleration and constraints on dark energy evolution"*, Astrophys. J. **607**, 665-687 (2004).

[188] A. G. Riess et al., *"Cepheid Calibrations of Modern Type Ia Supernovae:Implications for the Hubble Constant"*, Astrophys. J. Suppl. **183**, 109-141 (2009).

[189] G. Risaliti and E. Lusso, *"A Hubble Diagram for Quasars"*, Astrophys. J. **815**, 33 (2015).

[190] H. P. Robertson, *"Relativistic Cosmology"*, Rev. Mod. Phys. **5**, 62-90 (1933).

[191] H. P. Robertson, *"Kinematics and World-Structure"*, Astrophys. J. **82**, 284-301 (1935).

[192] P. G. Roll and D. T. Wilkinson, *"Cosmic Background Radiation at 3.2 cm-Support for Cosmic Black-Body Radiation"*, Phys. Rev. Lett. **16**, 405-407 (1966).

[193] A. Rozas-Fernández, *"Kinetic k-essence ghost dark energy model"*, Phys. Lett. **B709**, 313-321 (2012).

[194] A. Rozas-Fernández, *"K-essential covariant holography"*, Gen. Rel. Grav. **46**, 1825 (2014).

[195] V. Rubin, N. Thonnard, and J. Ford, W.K., *"Rotational properties of 21 SC galaxies with a large range of luminosities and radii, from NGC 4605 /R = 4kpc/ to UGC 2885 /R = 122 kpc/"*, Astrophys. J. **238**, 471 (1980).

[196] V. C. Rubin and W. K. Ford, Jr., *"Rotation of the Andromeda Nebula from a Spectroscopic Survey of Emission Regions"*, Astrophys. J. **159**, 379-403 (1970).

[197] R. K. Sachs and A. M. Wolfe, *"Perturbations of a cosmological model and angular variations of the microwave background"*, Astrophys. J. **147**, 73-90 (1967). [Gen. Rel. Grav.39,1929(2007)].

[198] A. Saha, F. Thim, G. A. Tammann, B. Reindl, and A. Sandage, *"Cepheid distances to sne ia host galaxies based on a revised photometric zero-point of the hst-wfpc2 and new p-l relations and metallicity corrections"*, Astrophys. J. Suppl. **165**, 108-137 (2006).

[199] V. Sahni and A. A. Starobinsky, *"The Case for a positive cosmological Lambda term"*, Int. J. Mod. Phys. **D9**, 373-444 (2000).

[200] V. Salvatelli, N. Said, M. Bruni, A. Melchiorri, and D. Wands, *"Indications of a late-time interaction in the dark sector"*, Phys. Rev. Lett. **113**, 181301 (2014).

[201] V. Salzano, S. A. Rodney, I. Sendra, R. Lazkoz, A. G. Riess, M. Postman, T. Broadhurst, and D. Coe, *"Improving Dark Energy Constraints with High Redshift Type Ia Supernovae from CANDELS and CLASH"*, Astron. Astrophys. **557**, A64 (2013).

[202] A. Sandage, *"Current Problems in the Extragalactic Distance Scale"*, Astrophys. J. **127**, 513-526 (1958).

[203] A. Sandage and G. A. Tammann, *"Absolute Magnitude Calibrations of Population I and II Cepheids and Other Pulsating Variables in the Instability Strip of the Hertzsprung-Russell Diagram"*, Ann. Rev. Astron. Astrophys. **44**, 93-140 (2006).

[204] H. Sandvik, M. Tegmark, M. Zaldarriaga, and I. Waga, *"The end of unified dark matter?"*, Phys. Rev. **D69**, 123524 (2004).

[205] R. J. Scherrer, *"Purely kinetic k-essence as unified dark matter"*, Phys. Rev. Lett. **93**, 011301 (2004).

[206] G. Schwarz, *"Estimating the Dimension of a Model"*, Annals Statist. **6**, 461-464 (1978).

[207] I. Sendra. *Cosmology in an accelerated universe: observations and phenomenology*. PhD thesis, University of the Basque Country (UPV/EHU), (2012).

[208] I. Sendra and R. Lazkoz, *"SN and BAO constraints on (new) polynomial dark energy parametrizations: current results and forecasts"*, Mon. Not. Roy. Astron. Soc. **422**, 776-793 (2012).

[209] H.-J. Seo and D. J. Eisenstein, *"Improved forecasts for the baryon acoustic oscillations and cosmological distance scale"*, Astrophys. J. **665**, 14-24 (2007).

[210] J. Silk, *"Cosmic black body radiation and galaxy formation"*, Astrophys. J. **151**, 459-471 (1968).

[211] J. Skilling, *"Nested sampling for general Bayesian computation"*, Bayesian Analysis **1**, 833-859 (2006).

[212] Z. Slepian, J. R. Gott, III, and J. Zinn, *"A one-parameter formula for testing slow-roll dark energy: observational prospects"*, Mon. Not. Roy. Astron. Soc. **438**, 1948-1970 (2014).

[213] V. M. Slipher, *"Nebulae"*, Proc. Am. Phil. Soc. **56**, 403-409 (1917).

[214] D. Spergel et al., *"Wide-Field InfraRed Survey Telescope-Astrophysics Focused Telescope Assets WFIRST-AFTA Final Report"*.

[215] D. J. Spiegelhalter, N. G. Best, B. P. Carlin, and A. van der Linde, *"Bayesian measures of model complexity and fit"*, J. Roy. Statist. Soc. **B64**, 583-639 (2002).

[216] P. Steinhardt. *Critical Problems in Physics*. Princeton University Press, Princeton., (1997).

[217] R. A. Sunyaev and Ya. B. Zeldovich, *"Small scale fluctuations of relic radiation"*, Astrophys. Space Sci. **7**, 3-19 (1970).

[218] R. A. Sunyaev and Ya. B. Zeldovich, *"The Observations of relic radiation as a test of the nature of X-Ray radiation from the clusters of galaxies"*, Comments Astrophys. Space Phys. **4**, 173 (1972).

[219] R. A. Sunyaev and Ya. B. Zeldovich, *"The Velocity of clusters of galaxies relative to the microwave background. The Possibility of its measurement"*, Mon. Not. Roy. Astron. Soc. **190**, 413-420 (1980).

[220] N. Suzuki et al., *"The Hubble Space Telescope Cluster Supernova Survey: V. Improving the Dark Energy Constraints Above z>1 and Building an Early-Type-Hosted Supernova Sample"*, Astrophys. J. **746**, 85 (2012).

[221] L. Szabados, *"Pulsating stars - plethora of variables and observational tasks"*, Contributions of the Astronomical Observatory Skalnate Pleso **43**, 338-350 (2014).

[222] N. R. Tanvir, *"Cepheid standard candles"*, ASP Conf. Ser. **167**, 84 (1999).

[223] M. Tegmark et al., *"The 3-D power spectrum of galaxies from the SDSS"*, Astrophys. J. **606**, 702-740 (2004).

[224] M. Tegmark et al., *"Cosmological Constraints from the SDSS Luminous Red Galaxies"*, Phys. Rev. **D74**, 123507 (2006).

[225] I. A. B. Tereno. *Cosmological Parameters Estimation with Cosmic Shear*. PhD thesis, Universidade de Lisboa, (2006).

[226] R. Trotta. *Cosmic microwave background anisotropies*. PhD thesis, Geneva U., (2004). URL `http://doc.rero.ch/record/3646?ln=en`.

[227] R. Trotta, *"Applications of Bayesian model selection to cosmological parameters"*, Mon.Not.Roy.Astron.Soc. **378**, 72-82 (2007).

[228] D. G. Turner, *"The Progenitors of Classical Cepheid Variables"*, J. Roy. Astron. Soc. Canada **90**, 82 (1996).

[229] J.-P. Uzan, C. Clarkson, and G. F. R. Ellis, *"Time drift of cosmological redshifts as a test of the Copernican principle"*, Phys. Rev. Lett. **100**, 191303 (2008).

[230] J. Valiviita and E. Palmgren, *"Distinguishing interacting dark energy from wCDM with CMB, lensing, and baryon acoustic oscillation data"*, JCAP **1507**, 015 (2015).

[231] F. van Leeuwen, M. W. Feast, P. A. Whitelock, and C. D. Laney, *"Cepheid Parallaxes and the Hubble Constant"*, Mon. Not. Roy. Astron. Soc. **379**, 723-737 (2007).

[232] L. Verde, *"A practical guide to Basic Statistical Techniques for Data Analysis in Cosmology"*.

[233] L. Verde, *"Statistical methods in cosmology"*, Lect. Notes Phys. **800**, 147-177 (2010).

[234] P. E. Vielzeuf and C. J. A. P. Martins, *"Probing dark energy beyond $z = 2$ with CODEX"*, Phys. Rev. **D85**, 087301 (2012).

[235] A. G. Walker, *"On Milne's Theory of World-Structure*"*, Proceedings of the London Mathematical Society **s2-42**, 90-127 (1937).

[236] Y. Wang and M. Dai, *"Exploring uncertainties in dark energy constraints using current observational data with Planck 2015 distance priors"*, Phys. Rev. **D94**, 083521 (2016).

[237] Y. Wang and P. Mukherjee, *"Observational Constraints on Dark Energy and Cosmic Curvature"*, Phys. Rev. **D76**, 103533 (2007).

[238] Y. Wang and S. Wang, *"Distance Priors from Planck and Dark Energy Constraints from Current Data"*, Phys. Rev. **D88**, 043522 (2013). [Erratum: Phys. Rev.D88,no.6,069903(2013)].

[239] Y. Wang, D. Wands, L. Xu, J. De-Santiago, and A. Hojjati, *"Cosmological constraints on a decomposed Chaplygin gas"*, Phys. Rev. **D87**, 083503 (2013).

[240] Y. Wang, G.-B. Zhao, D. Wands, L. Pogosian, and R. G. Crittenden, *"Reconstruction of the dark matter–vacuum energy interaction"*, Phys. Rev. **D92**, 103005 (2015).

[241] D. H. Weinberg, M. J. Mortonson, D. J. Eisenstein, C. Hirata, A. G. Riess, et al., *"Observational Probes of Cosmic Acceleration"*, Phys.Rept. **530**, 87-255 (2013).

[242] S. Weinberg. *Gravitation and Cosmology*. John Wiley and Sons, New York, (1972). ISBN 0471925675, 9780471925675. URL `http://www-spires.fnal.gov/spires/find/books/www?cl=QC6.W431`.

[243] H. Weyl, *"LXXXVI. Redshift and relativistic cosmology"*, The London, Edinburgh, and Dublin Philosophical Magazine and Journal of Science **9**, 936-943 (1930).

[244] J. A. Wheeler and K. Ford. *Geons, black holes, and quantum foam: A life in physics*. (1998).

[245] C. M. Will, *"The Confrontation between General Relativity and Experiment"*, Living Rev. Rel. **17**, 4 (2014).

[246] E. Wit, E. v. d. Heuvel, and J.-W. Romeijn, *"'All models are wrong...': an introduction to model uncertainty"*, Statistica Neerlandica **66**, 217-236 (2012).

[247] C.-M. Yoo, T. Kai, and K.-i. Nakao, *"Redshift Drift in LTB Void Universes"*, Phys. Rev. **D83**, 043527 (2011).

[248] H.-b. Zhang, W. Zhong, Z. H. Zhu, and S. He, *"Exploring holographic dark energy model with Sandage-Leob test"*, Phys. Rev. **D76**, 123508 (2007).

[249] J. Zhang, L. Zhang, and X. Zhang, *"Sandage-Loeb test for the new agegraphic and Ricci dark energy models"*, Phys. Lett. **B691**, 11-17 (2010).

[250] M.-J. Zhang and W.-B. Liu, *"Redshift drift reconstruction for some cosmological models from observations"*, Res. Astron. Astrophys. **13**, 1397-1408 (2013).

[251] M.-J. Zhang and W.-B. Liu, *"Observational constraint on the interacting dark energy models including the Sandage-Loeb test"*, Eur. Phys. J. **C74**, 2863 (2014).

[252] M.-J. Zhang, J.-Z. Qi, and W.-B. Liu, *"Cosmic Expansion History from the Distance Indicator and Redshift Drift"*, Int. J. Theor. Phys. **54**, 2456-2466 (2015).

[253] P. Zhang and A. Stebbins, *"Confirmation of the Copernican principle at Gpc radial scale and above from the kinetic Sunyaev Zel'dovich effect power spectrum"*, Phys. Rev. Lett. **107**, 041301 (2011).

[254] W.-T. Zhu, P.-X. Wu, and H.-W. Yu, *"Constraining the Generalized and Superfluid Chaplygin Gas Models with the Sandage-Loeb Test"*, Chin. Phys. Lett. **32**, 059501 (2015).

[255] F. Zwicky, *"Die Rotverschiebung von extragalaktischen Nebeln"*, Helv. Phys. Acta **6**, 110-127 (1933). [Gen. Rel. Grav.41,207(2009)].

[256] F. Zwicky, *"On the Masses of Nebulae and of Clusters of Nebulae"*, Astrophys. J. **86**, 217-246 (1937).